ISSN 3042-0466

Conference Proceedings META 2025

meta

ISSN 3042-0466 (Online)

META 2025

The 10th Conference on Mathematics in Engineering: Theory and Applications

Conference Proceedings

December 12-14, 2025
Novi Sad, Serbia

The 10th Conference on Mathematics in Engineering: Theory and Applications was organized by the Faculty of Technical Sciences, University of Novi Sad

Scientific Committee:

Biljana Carić, *president*, *University of Novi Sad*,
Ksenija Doroslovački, *University of Novi Sad*,
Tibor Lukić, *University of Novi Sad*,
Jelena Ivetić, *University of Novi Sad*.
Filip Tomić, *University of Novi Sad*,
Buda Bajić Papuga, *University of Novi Sad*,

Organizing Committee:

Vladimir Ilić, *president*, *University of Novi Sad*,
Zoran Ovcin, *University of Novi Sad*,
Ivan Prokić, *University of Novi Sad*,
Nataša Duraković, *University of Novi Sad*,
Jovana Dedeić, *University of Novi Sad*,
Srđan Milićević, *University of Novi Sad*,
Jelena Čolić Oravec, *University of Novi Sad*,
Marija Delić, *University of Novi Sad*,
Gabrijela Grujić, *University of Novi Sad*,
Tijana Ostojić, *University of Novi Sad*,
Jelena Stratijev, *University of Novi Sad*,
Dunja Arsić, *University of Novi Sad*,

The conference is supported by:

Ministry of Science, Technological Development and Innovation, Republic of Serbia

Faculty of Technical Sciences, University of Novi Sad

Contents

Predgovor

Pred vama je zbornik radova desetog izdanja konferencije Mathematics in Engineering: Theory and Applications - META 2025, koja je održana na Fakultetu tehničkih nauka Univerziteta u Novom Sadu od 12. do 14. decembra 2025. godine. Konferencija META od 2015. godine okuplja matematičare i inženjere koji izlažu naučne ili stručne radove iz svih teorijskih i primenjenih oblasti matematike, kao i iz metodike nastave matematike.

Ove godine, stiglo je dvadeset radova i svi pristigli radovi su prihvaćeni za izlaganje na konferenciji. Organizovane su tri sekcije usmenih izlaganja i jedna poster sekcija. Plenarno predavanje je održao dr Filip Tomić, vanredni profesor na Fakultetu tehničkih nauka u Novom Sadu.

Programski odbor su činili: dr Biljana Carić (predsednik), dr Tibor Lukić, dr Ksenija Doroslovački, dr Jelena Ivetić, dr Filip Tomić, dr Buda Bajić Papuga. Organizacioni odbor su činili: dr Vladimir Ilić (predsednik), dr Zoran Ovcin, dr Ivan Prokić, dr Nataša Duraković, dr Jovana Dedeić, dr Srđan Milićević, dr Jelena Čolić Oravec, dr Marija Delić, mr Gabrijela Grujić, dr Tijana Ostojić, dr Jelena Stratijev i dr Dunja Arsić.

Zahvaljujemo se plenarnom predavaču i svim autorima koji svojim interesovanjem i učešćem omogućavaju održavanje konferencije. Zahvaljujemo se recenzentima, kao i članovima programskog i organizacionog odbora na stručnom i odgovornom radu. Zahvalni smo šefu Katedre za matematiku dr Kseniji Doroslovački i direktoru Departmana za opšte discipline u tehnici dr Nebojši Raleviću na podršci, uloženom radu i trudu. Iskazujemo zahvalnost za pruženu finansijsku podršku Ministarstvu za nauku, tehnološki razvoj i inovacije Republike Srbije i Fakultetu tehničkih nauka u Novom Sadu.

The 10th Conference on Mathematics in Engineering: Theory and Applications
Novi Sad, December 12-14th 2025

EXTENDED GEVREY REGULARITY WITH APPLICATION TO WAVELETS[1]

Filip Tomić [2]

plenary talk

https://doi.org/10.24867/META.2025.00 Review Article

Abstract. In this paper, we investigate several fundamental properties of the extended Gevrey classes. Furthermore, as an application, we construct wavelets whose regularity is characterized by these classes.

AMS Mathematics Subject Classification (2020): 46E10; 46F05

Key words and phrases: Gevery classes, wavelet, Lambert W function

1. Introduction

We will give a short review on some of the properties of the extended Gevrey classes. Moreover, we will use the following function

$$f_{\rho,\sigma}(t) = e^{-\rho g_\sigma\left(\frac{1}{t}\right)}, \quad \rho > 0,\ \sigma > 1, \tag{1.1}$$

where

$$g_\sigma(t) = \frac{\ln^{\frac{\sigma}{\sigma-1}}(1+|t|)}{W^{\frac{1}{\sigma-1}}(\ln(1+|t|))}, \quad t \in \mathbb{R},$$

and W denotes the principal branch of *Lambert W function*, to construct a wavelet which is extended Gevrey regular in both time and frequency domains.

Extended Gevrey classes were introduced in [10] to describe regularity between the Gevrey classes and C^∞. The derivatives of their elements are controlled by sequences of *rapid growth*

$$\{M_p^{\tau,\sigma} = p^{\tau p^\sigma}\}_{p\in\mathbb{N}_0}, \quad \tau > 0,\ \sigma > 1. \tag{1.2}$$

These classes provide an important example of *weight matrix classes* of ultradifferentiable functions (see [5, 13]). Moreover, the function in (1.1) can be estimated in terms of the associated function corresponding to the sequences

[1]This research was partially supported by the Science Fund of the Republic of Serbia, #GRANT No. 2727, *Global and local analysis of operators and distributions* - GOALS, and by the project "Socio-technological aspects of improving the teaching process in the English language in fundamental disciplines", Department of Fundamental Sciences, Faculty of Technical Sciences, University of Novi Sad.

[2]Department of Fundamental Sciences, Faculty of Technical Sciences, University of Novi Sad, e-mail: filip.tomic@uns.ac.rs

in (1.2). For some applications of the theory of extended Gevrey classes, we refer to [1, 2, 6, 7].

Lambert W function (see [9]) is defined as the multivalued inverse of the function $z \mapsto ze^z$ for $z \in \mathbb{C}$. It splits the complex plane into infinitely many regions. Throughout the paper we will use the notation $W(z)$, $z \in \mathbb{C} \setminus (-\infty, -e^{-1}]$, for its principal branch (instead of common $W_0(z)$). The boundary curve of its principal branch is given by:

$$\{(-t\,\mathrm{ctg}t, t) \in \mathbb{R}^2 \mid -\pi < t < \pi\}.$$

2. Extended Gevrey classes

We start with the following Lemma that contains the properties of sequences given in (1.2).

Lemma 2.1. *Let $\tau > 0$, $\sigma > 1$, $M_0^{\tau,\sigma} = 1$, and $M_p^{\tau,\sigma} = p^{\tau p^\sigma}$, $p \in \mathbb{N}$. Then there exists constant $C > 1$ such that:*

$(M.1)$ $(M_p^{\tau,\sigma})^2 \leq M_{p-1}^{\tau,\sigma} M_{p+1}^{\tau,\sigma}$, $p \in \mathbb{N}$,

$\widetilde{(M.2)}$ $\quad M_{p+q}^{\tau,\sigma} \leq C^{p^\sigma + q^\sigma} M_p^{\tau 2^{\sigma-1},\sigma} M_q^{\tau 2^{\sigma-1},\sigma}$, $p, q \in \mathbb{N}_0$,

$\widetilde{(M.2)}'$ $M_{p+1}^{\tau,\sigma} \leq C^{p^\sigma} M_p^{\tau,\sigma}$, $p \in \mathbb{N}_0$,

$(M.3)'$ $\displaystyle\sum_{p=1}^{\infty} \frac{M_{p-1}^{\tau,\sigma}}{M_p^{\tau,\sigma}} < \infty.$

In addition, if $\sigma_2 > \sigma_1 > 1$ and $\tau_0 > 0$ then for every $h, \tau > 0$ there exists $C > 0$ such that

$$h^{p^{\sigma_1}} M_p^{\tau_0,\sigma_1} \leq C M_p^{\tau,\sigma_2}$$

Let us briefly discuss the borderline case $\sigma = 1$. Note that $M_p := M_p^{\tau,1} = p^{\tau p}$, $\tau > 0$, is the Gevrey sequence, and the conditions $(M.1)$, $\widetilde{(M.2)}'$, and $\widetilde{(M.2)}$ are classical Komatsu conditions $(M.1)$, $(M.2)'$, and $(M.2)$, respectively. Moreover, M_p satisfies condition $(M.3)'$ if and only if $\tau > 1$, which ensures that the corresponding ultradifferentiable classes contain functions with compact support (see [8]). The proof of Lemma 2.1 is given in [10].

Next we define extended Gevrey classes $\mathcal{E}_{\tau,\sigma}(\mathbb{R})$.

Definition 2.1. *Let $\tau > 0$ and $\sigma > 1$ and $M_p^{\tau,\sigma} = p^{\tau p^\sigma}$ for $p \in \mathbb{N}$, $M_0^{\tau,\sigma} = 1$. A smooth function ϕ belongs to $\mathcal{E}_{\tau,\sigma}(\mathbb{R})$ if*

$$(\forall \mathbb{K} \subset\subset \mathbb{R})(\exists C > 0) \quad \sup_{x \in \mathbb{K}} |\phi^{(p)}(x)| \leq C^{p^\sigma + 1} M_p^{\tau,\sigma},\ p \in \mathbb{N}_0.$$

We denote

$$\mathcal{E}_\sigma(\mathbb{R}) = \bigcup_{\tau > 0} \mathcal{E}_{\tau,\sigma}(\mathbb{R}).$$

Again for $\sigma = 1$ we obtain some of the well-known classes. For instance that $\mathcal{A}(\mathbb{R}) := \mathcal{E}_{1,1}(\mathbb{R})$, and $\mathcal{G}_t(\mathbb{R}) := \mathcal{E}_{1,t}(\mathbb{R})$ for $t > 1$; these are the spaces of locally analytic functions and Gevrey functions of order t, respectively.

In the following Proposition we collect some of the basic properties of the extended Gevrey classes. The proof relies on the properties of $M_p^{\tau,\sigma}$ given in Lemma 2.1 (see [10, 11, 12, 13]).

Proposition 2.1. *Let $\tau > 0$ and $\sigma > 1$. Then*

i) For $\sigma_2 > \sigma_1 > 1$ we have

$$\mathcal{A}(\mathbb{R}) \subset \bigcup_{t>1} \mathcal{G}_t(\mathbb{R}) \subset \bigcap_{\tau>0} \mathcal{E}_{\tau,\sigma_1}(\mathbb{R}) \subset \mathcal{E}_{\tau,\sigma_1}(\mathbb{R}) \subset \mathcal{E}_{\sigma_1} \subset \mathcal{E}_{\sigma_2} \subset C^\infty(\mathbb{R}).$$

ii) $\mathcal{E}_{\tau,\sigma}(\mathbb{R})$ is closed under the pointwise multiplication.

iii) $\mathcal{E}_{\tau,\sigma}(\mathbb{R})$ is closed under finite order derivation.

iv) $\mathcal{E}_{\tau,\sigma}(\mathbb{R})$ is closed under superposition. In particular, if $F(x) \in \mathcal{A}(\mathbb{R})$ and $f(x) \in \mathcal{E}_{\tau,\sigma}(\mathbb{R})$ then $F(f(x)) \in \mathcal{E}_{\tau,\sigma}(\mathbb{R})$.

v) $\mathcal{E}_{\tau,\sigma}(\mathbb{R})$ is invariant under translations and dilatations.

Let us define a function associated to $M_p^{\tau,\sigma}$, $p \in \mathbb{N}_0$.

Definition 2.2. *Let $\tau > 0$ and $\sigma > 1$. Then the associated function to the sequence $M_p^{\tau,\sigma}$ is given by*

$$T_{\tau,\sigma}(k) = \sup_{p\in\mathbb{N}_0} \ln \frac{k^p}{M_p^{\tau,\sigma}}, \qquad k > 0. \tag{2.1}$$

In the following Theorem we estimate $T_{\tau,\sigma}(k)$ in terms of the Lambert W function. The proof can be found in [13], and for a more general version we refer to [12].

Theorem 2.1. *For $\tau > 0$ and $\sigma > 1$ we have*

$$T_{\tau,\sigma}(k) \asymp \tau^{-\frac{1}{\sigma-1}} \frac{\ln^{\frac{\sigma}{\sigma-1}}(1+k)}{W^{\frac{1}{\sigma-1}}(\ln(1+k))}, \quad k \geq 0.$$

In particular, $T_{\tau,\sigma}(|k|) \asymp \rho\, g_\sigma(k)$, $k \in \mathbb{R}$, for $\rho = \tau^{-\frac{1}{\sigma-1}}$ where g_σ is given in (1.1).

Next we discuss the connection between functions given in (1.1), sequences in (1.2) and associated function (2.1).

Let us define

$$h_{\tau,\sigma}(t) := e^{-T_{\tau,\sigma}(1/t)} = \inf_{p\in\mathbb{N}_0} M_p^{\tau,\sigma} t^p, \quad t \geq 0.$$

Then Theorem 2.1 implies that for any $\rho > 0$ and $\sigma > 1$ there exist constants $A, B, \tau_1, \tau_2 > 0$ such that

$$Ah_{\tau_1,\sigma}(|t|) \leq f_{\rho,\sigma}(t) \leq Bh_{\tau_2,\sigma}(|t|), \quad t \in \mathbb{R}, \tag{2.2}$$

where $f_{\rho,\sigma}$ is given in (1.1). Note that the right-hand side of (2.2) implies that for any given $\rho > 0$ there exists $B_1, \tau > 0$ such that

$$\sup_{t>0} \frac{f_{\rho,\sigma}(t)}{t^p} \leq B_1 M_p^{\tau,\sigma}, \quad p \in \mathbb{N}_0. \tag{2.3}$$

Estimate (2.3) (together with Caushy's integral formula) can be used to prove that

$$f_{\rho_\sigma,\sigma}(t) = \exp\left\{-e^{-\frac{1}{\sigma}} W^{-\frac{1}{\sigma-1}}\left(\ln\left(1+\frac{1}{|t|}\right)\right) \ln^{\frac{\sigma}{\sigma-1}}\left(1+\frac{1}{|t|}\right)\right\}, \, t \in \mathbb{R}, \tag{2.4}$$

is an example of the extended Gevrey function. In particular, following Proposition holds.

Proposition 2.2. *If $\sigma > 1$ and the function $f_{\rho_\sigma,\sigma}$ is given in* (2.4) *then:*

a) $\lim_{t\to 0} f^{(j)}_{\rho_\sigma,\sigma}(t) = 0$, $j \in \mathbb{N}$,

b) $f_{\rho_\sigma,\sigma}(t) \in \mathcal{E}_\sigma(\mathbb{R})$.

We conclude this section with the Paley–Wiener theorem, which connects the time-domain regularity of a function with its decay rate in the Fourier domain. The decay rate we use is given in the following definition.

Definition 2.3. *Let $\sigma > 1$ and $g_\sigma(\xi) = \dfrac{\ln^{\frac{\sigma}{\sigma-1}}(1+|\xi|)}{W^{\frac{1}{\sigma-1}}(\ln(1+|\xi|))}$ be as in* (1.1)*. A continuous function $f(\xi)$ belongs to $\mathbf{\Gamma}_\sigma(\mathbb{R})$, if there exist $\rho > 0$ and $C > 0$ such that*

$$|f(\xi)| \leq C\, e^{-\rho g_\sigma(\xi)}, \quad \xi \in \mathbb{R}.$$

We now state the Paley–Wiener theorem. For the proof we refer to [12].

Theorem 2.2. *Let $\sigma > 1$.*

a) Let φ be a C^∞ function with compact support. If $\varphi(x) \in \mathcal{E}_\sigma(\mathbb{R})$ then $\widehat{\varphi}(\xi) \in \mathbf{\Gamma}_\sigma(\mathbb{R})$.

b) If the function φ is such that $\widehat{\varphi}(\xi) \in \mathbf{\Gamma}_\sigma(\mathbb{R})$ then $\varphi(x) \in \mathcal{E}_\sigma(\mathbb{R})$.

3. Wavelet construction

In this section, we use the functions given in (1.1) to construct an orthonormal wavelet ψ such that both ψ and its Fourier transform $\hat{\psi}$ belong to $\mathcal{E}_\sigma(\mathbb{R})$. Our construction follows the ideas of multiresolution analysis (MRA for short, see [3, 4]). We refer to [14] for the construction of band-limited wavelets, that is, wavelets whose Fourier transform has compact support.

Let $m_0(\xi)$ be a *low-pass filter* of the orthonormal wavelet that satisfies following minimal requirements:

i) m_0 is a continuous, even, $2\pi-$ periodic function on $\mathbb{R}, m_0(0) = 1$,

ii) $\inf_{\xi \in [-\pi/3, \pi/3]} |m_0(\xi)| \neq 0$,

iii) $|m_0(\xi)|^2 + |m_0(\xi + \pi)|^2 = 1$.

Then the Fourier transform of the *scaling function* φ is continuous and

$$\hat{\varphi}(\xi) = \prod_{j=1}^{\infty} m_0(2^{-j}\xi), \quad \xi \in \mathbb{R}.$$

Moreover, if m_0 is smooth then $\hat{\varphi}$ is smooth.

Fourier transform of the orthonormal wavelet is then given by

$$\hat{\psi}(\xi) = e^{i\frac{\xi}{2}} \overline{m_0\Big(\frac{\xi}{2} + \pi\Big)} \hat{\varphi}\Big(\frac{\xi}{2}\Big), \quad \xi \in \mathbb{R}. \tag{3.1}$$

In particular, it is sufficient to construct a low-pass filter that belongs to $\mathcal{E}_\sigma$. The properties of extended Gevrey classes given in Proposition 2.1, together with the Paley–Wiener theorem (2.2), imply that the orthonormal wavelet defined in (3.1) satisfies $\psi, \hat{\psi} \in \mathcal{E}_\sigma(\mathbb{R})$.

We construct the desired low-pass filter as follows. Let

$$\gamma_\sigma(\eta) := \begin{cases} f_\sigma(\eta) & , \eta > 0 \\ 0 & , \eta \leq 0, \end{cases}$$

where $f_\sigma = f_{1,\sigma}$ is given in (1.1).

For

$$\delta_\sigma(\xi) := \begin{cases} \left(\int_0^1 \gamma_\sigma(\eta)\gamma_\sigma(1-\eta)\, d\eta\right)^{-1} \int_0^\xi \gamma_\sigma(\eta)\gamma_\sigma(1-\eta)\, d\eta & , \xi > 0 \\ 0 & , \xi \leq 0, \end{cases}$$

Let us define

$$\theta_\sigma(\xi) := \left(1 - \delta_\sigma\left(\frac{5\xi - \pi}{3\pi}\right)\right) \delta_\sigma\left(\frac{|\xi - \frac{2\pi}{3}|}{d}\right), \quad \xi \in \left[\frac{\pi}{2}, \pi\right), d \in \left(0, \frac{\pi}{6}\right].$$

Note that θ_σ can be extended to $[0, 2\pi]$ by $\theta_\sigma(\xi) + \theta_\sigma(\xi + \pi) = 1$, and then further extended on $\mathbb{R}$ so that it is 2π periodic.

Finally, low-pass filter $m_0 \in \mathcal{E}_\sigma$ is given by

$$m_0(\xi) = \sin\left(\frac{\pi}{2}\theta_\sigma(\xi)\right), \xi \in \mathbb{R}.$$

The further details concerning wavelet construction can be found in [15].

References

[1] A. Cáceres, A. Lastra, *On the domain and growth rate of the solutions to linear systems of moment differential equations,* Journal of Mathematical Analysis and Applications, 556, 1, (2026)

[2] M. Cicognani, D. Lorentz, *Strictly hyperbolic equations with coefficients low-regular in time and smooth in space*, J. Pseudo-Differ. Oper. Appl., 9, no. 3 (2018)

[3] N. Fukuda, T. Kinoshita, and I. Uehara, *On the wavelets having Gevrey regularities and subexponential decays.* Math. Nachr., 287 (2014)

[4] E. Hernández, G. Weiss, *A first course of wavelets.* CRC Press, 1996.

[5] J. Jiménez-Garrido, D.N. Nenning, G. Schindl, *On generalized definitions of ultradifferentiable classes*, J. Math. Anal. Appl. 526, Paper No. 127260 (2023)

[6] J. Jiménez-Garrido, A. Lastra, J. Sanz, *Extension Operators for Some Ultraholomorphic Classes Defined by Sequences of Rapid Growth.* Constr Approx 60, 285–307 (2024).

[7] Jiménez-Garrido, J., Miguel-Cantero, I., Sanz, J. et al. *Optimal Flat Functions in Carleman–Roumieu Ultraholomorphic Classes in Sectors.* Results Math 78, 98 (2023).

[8] H. Komatsu, *Ultradistributions, I: Structure theorems and a characterization.* J. Fac. Sci. Univ. Tokyo, Sect. IA Math., 20 (1) (1973)

[9] I. Mező, *The Lambert W Function Its Generalizations and Applications*, CRC Press, Boca Raton, 2022.

[10] S. Pilipović, N. Teofanov, F. Tomić, *On a class of ultradifferentiable functions*, Novi Sad Journal of Mathematics, 45 (1), (2015)

[11] S. Pilipović, N. Teofanov, F. Tomić, *Superposition and propagation of singularities for extended Gevrey regularity*, FILOMAT 32 (2018)

[12] S. Pilipović, N. Teofanov, F. Tomić, *A Paley–Wiener theorem in extended Gevrey regularity*, J. Pseudo-Differ. Oper. Appl., 11 (2020)

[13] N. Teofanov, F. Tomić, *Extended Gevrey regularity via weight matrices*, Axioms 2022, 11, 576 (2022),

[14] N. Teofanov, F. Tomić, S. Tutić, *Band-limited wavelets beyond Gevrey regularity*, International Journal of Wavelets, Multiresolution and Information Processing, Vol. 22, No. 5 (2024)

[15] F. Tomić, S. Tutić, M.Žigić *Extending wavelet regularity beyond Gevrey classes*, http://arxiv.org/abs/2512.05655, preprint (2025)

The 10th Conference on Mathematics in Engineering: Theory and Applications
Novi Sad, December 12-14th 2025

MAGIČNE KONFIGURACIJE NA C_{24} FULERENU[1]

Đorđe Baralić [2] i **Adam Farhat** [3]

https://doi.org/10.24867/META.2025.01 Originalni naučni članak

Sažetak. Fulereni su alotropi ugljenika koji imaju šuplju, kaveznu strukturu. Atomi u molekulu raspoređeni su u petougaone i šestougaone prstenove tako da je svaki atom povezan sa još tri atoma. Jednostavni poliedri koji imaju samo petougaone i šestougaone strane predstavljaju matematički model za fulerene. Kažemo da fulleren sa n temena ima magično svojstvo ako se brojevi $1, 2, \dots, n$ mogu dodeliti njegovim temenima tako da su zbirovi brojeva u svakom petouglu jednaki i zbirovi brojeva na svakom šestouglu jednaki. Pokazujemo da C_{8n+4} ne dozvoljava takvo uređenje za sva n, dok fuleren C_{24} ima mnogo neizomorfnih takvih uređenja.

AMS Mathematics Subject Classification (2020): 00A08

Ključne reči i izrazi: magično svojstvo, fulerenu, C_{24}

1. Uvod

Pre četrdeset godina, ser Harald V. Kroto, Robert F. Karl, mlađi i Ričard Smoli otkrili su prvi fuleren C_{60}, takođe poznat kao bakminsterfuleren ili ,,bakibol", vidi [4]. Za ovo otkriće dobili su Nobelovu nagradu za hemiju 1996. godine. Identifikacija fulerena značajno je proširila spektar priznatih alotropa ugljenika, koji je ranije bio ograničen na grafit, dijamant i amorfne forme ugljenika kao što su čađ i ugalj. Nakon otkrića bakminsterfulerena, potvrđeno je postojanje sličnih struktura sa 70, 76, 78, 82, 84, 90, 94 ili 96 atoma ugljenika. Oni su bili u fokusu opsežnih istraživanja, kako u vezi sa njihovim hemijskim svojstvima, tako i sa tehnološkim primenama, naročito u nauci o materijalima, elektronici i nanotehnologiji.

Eksperimentalno proučavanje fulerena bilo je praćeno teorijskim istraživanjima zasnovanim na matematičkim modelima molekula fulerena koji se nazivaju fulerenski grafovi. Temena grafova predstavljaju atome, a grane veze između atoma u molekulu. Matematički, fuleren je 3-povezan 3-regularan ravanski graf koji ima samo petougaone i šestougaone strane. Ekvivalentno, matematički fuleren može se posmatrati kao jednostavan 3-poliedar čije su strane petougaonici ili šestougaonici. Ojlerova formula implicira da broj

[1] Prvi autor je podržan od Ministarstva nauke, tehnološkog razvoja i inovacija Republike Srbije kroz institucionalno finansiranje Matematičkog instituta SANU.

[2] Matematički institut SANU, Beograd, Srbija e-mail: djbaralic@mi.sanu.ac.rs

[3] Amerikanska akademija Dubai, Ujedinjeni Arapski Emirati e-mail: adamfermata@gmail.com

petougaonih strana u fulerenu iznosi 12, dok je broj temena paran. Grinbaum i Motzkin u [3] pokazali su da postoji fuleren sa svakim parnim $n \geq 24$ i sa $n = 20$ temena, kao i da ne postoji fuleren sa $n = 22$ temena.

Baralić i Milenković u [?] predložili su proučavanje jednog zanimljivog svojstva motivisanog konfiguracijama magičnih kvadrata. Oni su pronašli primer rasporeda prvih dvadeset četiri pozitivna broja po dvadeset četiri temena trodimenzionalnog permutoedra tako da su zbirovi brojeva u temenima svakog kvadrata i svakog šestougla konstantni. Ovo svojstvo nazvali su *magičnim*. Pojam magičnog svojstva može se slično uvesti i za fulerene. Fuleren sa n temena ima magično svojstvo ako se prvih n pozitivnih brojeva može pridružiti tako da po jedno teme nosi jedan broj i tako da je zbir brojeva na svakom petougaonom licu konstantan, kao i odgovarajuci zbir za svako šestougaono lice. Cilj ovog rada je da predstavi i razmotri neke rezultate o magičnom svojstvu fulerena.

2. Fulereni i magično svojstvo

Označimo sa $V = \{v_1, v_2, \ldots, v_n\}$ skup temena fulerena C_n.

Definicija 2.1. Neka su $\mathcal{H}$ i $\mathcal{P}$ skupovi šestougaonih i petougaonih strana na fulerenu C_n. Kažemo da fuleren C_n ima magično svojstvo ako postoji bijekcija $f\colon V \to \{1, 2, \ldots, n\}$, nazvana magična konfiguracija, takva da

$$\sum_{v \in H_i} f(v) = S_h, \quad \forall H_i \in \mathcal{H}$$

$$\sum_{v \in P_j} f(v) = S_p, \quad \forall P_j \in \mathcal{P}$$

gde se zbir po petouglu S_p i zbir po šestouglu S_h smatraju magičnim konstantama fulerena.

Fuleren može imati mnogo različitih magičnih konfiguracija, uključujući i one sa različitim magičnim konstantama, što ćemo videti u narednom odeljku. Međutim, magične konstante S_p i S_h za dati fuleren C_n zadovoljavaju narednu relaciju.

Tvrđenje 2.2. *Ako fuleren C_n ima magično svojstvo, tada*

$$24S_p + (n - 20)S_h = 3n(n + 1). \tag{2.1}$$

Dokaz. Relacija se dobija sabiranjem brojeva preko svih strana C_n, čime se dobija tri puta zbir prvih n pozitivnih brojeva, jer svako teme pripada tačno trima stranama. □

Baralić i Milenković koristili su (2.1) i argument deljivosti u [?] da pokažu da ne postoji magična konfiguracija na dodekaedru C_{20}. Isti rezon može se primeniti na bakminsterfuleren C_{60}. Kada bi postojala magična konfiguracija na C_{60}, tada bi po (2.1) magične konstante zadovoljavale

$$24S_p + 40S_h = 3 \cdot 60 \cdot 61,$$

što je nemoguće zbog toga što je leva strana deljiva sa 8. Zaista, argument se neposredno generalizuje na sledeći rezultat.

Teorema 2.3. *Ako je $n \equiv 4 \pmod 8$, tada fuleren C_n ne dozvoljava magičnu konfiguraciju.*

Dokaz. Pretpostavimo suprotno. Tada je $24S_p + (n-20)S_h \equiv 0 \pmod 8$. S druge strane, $3n(n+1) \equiv 4 \pmod 8$. Kontradikcija! □

Na osnovu kongruencija modulo 8 ne možemo zaključiti mnogo o ostalim slučajevima.

Tvrđenje 2.4.

$$S_h \equiv \begin{cases} 0 \pmod 2, & \textit{ako je } n \equiv 0 \pmod 8, \\ 3 \pmod 4, & \textit{ako je } n \equiv \pm 2 \pmod 8. \end{cases}$$

Na žalost, korišćenjem ovakvih elementarnih brojevnoteorijskih argumenata ne može se dobiti mnogo. Radom modulo 3, najviše što se može reći je sledeće.

Tvrđenje 2.5. *Ako $n \not\equiv 2 \pmod 3$ i fuleren C_n dozvoljava magičnu konfiguraciju, tada $S_h \equiv 0 \pmod 3$.*

3. Magične konfiguracije na C_{24}

U prethodnom odeljku ustanovili smo nekoliko rezultata o nepostojanju magičnih konfiguracija na fulerenima. Najjednostavniji slučaj fulerena je C_{24}: njegov Šlegelov dijagram dat je na slici 1. C_{24} ima 24 temena, dvanaest petougaonih i dve šestougaone strane.

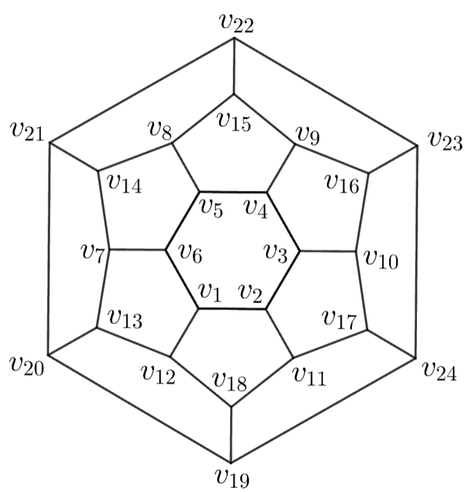

Slika 1: Schlegel dijagram za C_{24}

Proučavanje magičnih konfiguracija na C_{24} počinjemo ispitivanjem njegovih magičnih konstanti S_p i S_h. Korišćenjem (2.1) dobijamo

$$6S_p + S_h = 450. \tag{3.1}$$

Gornja linearna Diofantska jednačina ima rešenja u pozitivnim celim brojevima, npr. $S_p = 50$ i $S_h = 150$, tako da se ne može isključiti mogućnost postojanja magičnog svojstva kod C_{24}.

Iz (3.1) je jasno da $S_h \equiv 0 \pmod 6$. Dva šestougla u C_{24} ne dele nijedno teme. Najmanja moguća vrednost za S_h nije manja od zbira brojeva iz skupa $\{1, 2, \ldots, 12\}$ raspoređenih na temena šestougla, što iznosi 39. S druge strane, najveća moguća vrednost nije veća od zbira brojeva $\{13, 14, \ldots, 24\}$, što iznosi 111.

Međutim, uslov $S_h \equiv 0 \pmod 6$ implicira

$$S_h \in \{42, 48, 54, 60, 66, 72, 78, 84, 90, 96, 102, 108\},$$

a odgovarajuće vrednosti za S_p su

$$S_p \in \{68, 67, 66, 65, 64, 63, 62, 61, 60, 59, 58, 57\}.$$

Ispitali smo sve očigledne brojevnoteorijske argumente i ne mogu se dobiti nova ograničenja za magične konstante. Ručno traženje magične konfiguracije za te konstante deluje besmisleno, pa smo stoga napisali program [2] da proveri koje permutacije prvih 24 pozitivnih brojeva zadovoljavaju sistem (3.2) Diofantskih jednačina za svaki od dvanaest parova konstanti (S_p, S_h). Promenljive su povezane sa temenima označenim na slici 1. Više o programu dato je u [**?**].

(3.2)
$$\begin{aligned}
v_1 + v_2 + v_3 + v_4 + v_5 + v_6 &= S_h & v_{19} + v_{20} + v_{21} + v_{22} + v_{23} + v_{24} &= S_h \\
v_5 + v_8 + v_{15} + v_9 + v_4 &= S_p & v_4 + v_9 + v_{16} + v_{10} + v_3 &= S_p \\
v_3 + v_{10} + v_{17} + v_{11} + v_2 &= S_p & v_2 + v_{11} + v_{18} + v_{12} + v_1 &= S_p \\
v_1 + v_{12} + v_{13} + v_7 + v_6 &= S_p & v_6 + v_7 + v_{14} + v_8 + v_5 &= S_p \\
v_{14} + v_8 + v_{15} + v_{22} + v_{21} &= S_p & v_{15} + v_9 + v_{16} + v_{23} + v_{22} &= S_p \\
v_{16} + v_{10} + v_{17} + v_{24} + v_{23} &= S_p & v_{17} + v_{11} + v_{18} + v_{19} + v_{24} &= S_p \\
v_{18} + v_{12} + v_{13} + v_{20} + v_{19} &= S_p & v_{13} + v_7 + v_{14} + v_{21} + v_{20} &= S_p
\end{aligned}$$

Iznenađujuće, program je pronašao mnogo rešenja u svakom od dvanaest slučajeva.

Za zaključak analize C_{24}, dajemo primere magičnih konfiguracija. Na slici 2 predstavljena je po jedna magična konfiguracija za svaki od dvanaest parova magičnih konstanti S_p i S_h.

Literatura

[1] Đ. Baralic and L. Milenković, *The Magic Permutohedron*, *Math. Intelligencer* 46 , pp. 260-263, 2024.

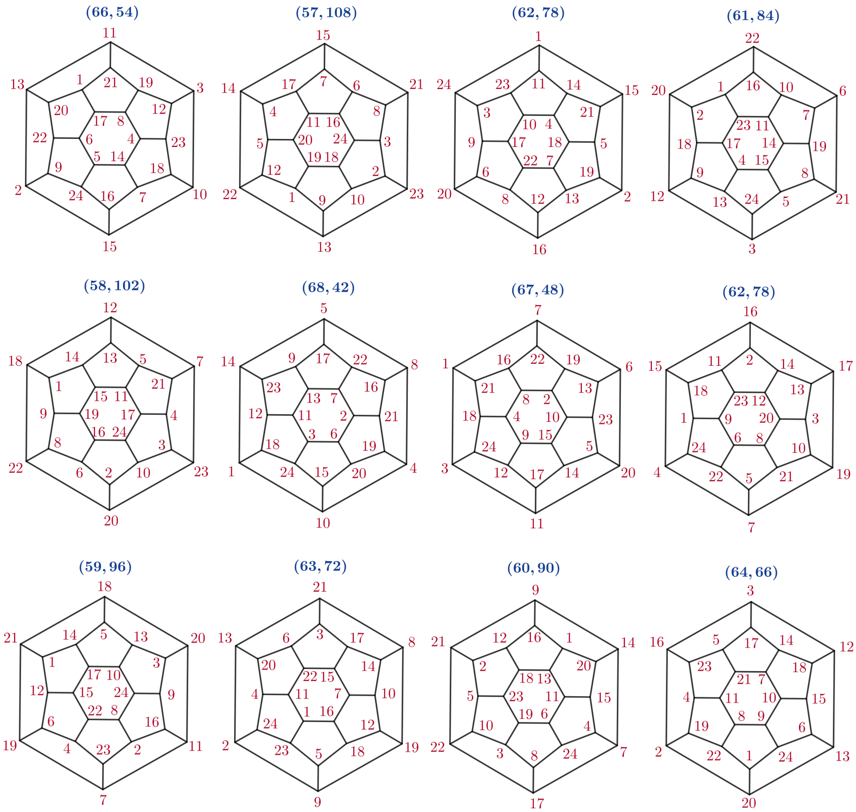

Slika 2: Primeri magičnih konfiguracija na C_{24}

S_p	S_h	# of solutions	S_p	S_h
57	108	576	68	42
58	102	936	67	48
59	96	2832	66	54
60	90	8832	65	60
61	84	11208	64	66
62	78	14592	63	72

Tabela 1: Broj magičnih konfiguracija na C_{24} za date magične konstante

[2] A. Farhat, *Magic Property of Fullerenes*, GitHub repository (2025), https://github.com/jazzbits/magic_property_of_fullerenes

[3] B. Grünbaum and T. S. Motzkin,"The number of hexagons and the simplicity of geodesics on certain polyhedra", *Canadian J. Math.*, vol. 15, pp. 744-751, 1963.

[4] H. W. Kroto, J. R. Heath, S. C. O'Brien, R. F. Curl, R. E. Smalley, "C60: Buckminsterfullerene", *Nature*, vol. 318, pp. 162-163, 1985.

The 10th Conference on Mathematics in Engineering: Theory and Applications
Novi Sad, December 12-14th 2025

A NEW FUZZY CONTRACTIVE CONDITION IN FUZZY METRIC SPACES WITH APPLICA-TIONS TO IMAGE PROCESSING

Biljana Carić [1] and **Tatjana Došenović** [2]

https://doi.org/10.24867/META.2025.02 Scientific Article

Abstract. We introduce a new fuzzy contractive condition in fuzzy metric spaces equipped with continuous t-norms of H-type and establish a fixed point theorem under this assumption. A concrete example is provided, together with an application to iterative image filtering.

AMS Mathematics Subject Classification (2020): 54H25, 47H10, 68U10

Key words and phrases: fuzzy metric space, fixed point theorem, fuzzy contractive mapping, image denoising.

1. Introduction

Fixed point theory has been a cornerstone of modern mathematical analysis since Banach introduced his contraction principle in 1922, guaranteeing the existence and uniqueness of fixed points for self-mappings in complete metric spaces. Over time, numerous generalizations were developed to extend these results to more abstract settings, including fuzzy metric spaces, which allow for modeling uncertainty and imprecision encountered in real-world problems. Fixed point theory in fuzzy metric spaces has been extensively studied, providing the foundation for our work [1, 2, 4, 5].

Fuzzy sets, introduced by Zadeh in 1965 [13], provide a mathematical framework for dealing with uncertainty. Fuzzy metric spaces, formalized by Kramosil and Michalek (1975) and further developed by George and Veeramani (1994), incorporate a continuous t-norm to define a generalized notion of distance. These spaces have found applications in image processing, decision making, control theory, and other fields where uncertainty plays a crucial role.

2. Preliminaries

Definition 2.1. [8] A binary operation $* : [0,1]^2 \to [0,1]$ is a t-norm if it is commutative, associative, nondecreasing in each argument, and has 1 as the neutral element ($a * 1 = a$).

Example 2.2. Basic examples of t-norms: Minimum t-norm: $*_M(a,b) = \min(a,b)$, $*_P(a,b) = a \cdot b$, $*_L(a,b) = \max\{0, a+b-1\}$.

[1]Faculty of Technical Sciences, University of Novi Sad, e-mail: biljana@uns.ac.rs
[2]Faculty of Technology Novi Sad, University of Novi Sad, e-mail: tatjanad@uns.ac.rs

Definition 2.3. [7] Let $*$ be a t-norm and let the sequence of functions $*_n : [0,1] \to [0,1]$ $(n \in \mathbb{N})$ be defined as follows:

$$*_1(x) = *(x,x), \qquad *_{n+1}(x) = *(*_n(x), x), \quad (n \in \mathbb{N},\, x \in [0,1]).$$

A t-norm $*$ is said to be of *Hadžić type* (or H-*type*) if the family $\{*_n(x)\}_{n\in\mathbb{N}}$ is equicontinuous at the point $x = 1$; that is, for every $\lambda \in (0,1)$ there exists $\delta(\lambda) \in (0,1)$ such that the implication

$$x > 1 - \delta(\lambda) \;\Rightarrow\; *_n(x) > 1 - \lambda, \qquad \text{for all } n \in \mathbb{N},$$

holds true.

Definition 2.4. [5] Let X be a nonempty set and $*$ a continuous t-norm. A function

$$M : X \times X \times (0,\infty) \to [0,1]$$

is called a fuzzy metric if for all $x, y, z \in X$ and $s, t > 0$, the following hold:

1. $M(x,y,t) = 1$ if and only if $x = y$,
2. $M(x,y,t) = M(y,x,t)$,
3. $M(x,y,t) * M(y,z,s) \le M(x,z,t+s)$,
4. $M(x,y,\cdot) : (0,\infty) \to [0,1]$ is continuous,

The triple $(X, M, *)$ is called a fuzzy metric space

Definition 2.5. [6] $M(x,\, y,\, \cdot)$ is nondecreasing for all $x,\, y \in X$.

Definition 2.6. [5] Let $(X, M, *)$ be a fuzzy metric space. A sequence $\{x_n\} \subset X$ is said to converge to $x \in X$ if for every $\varepsilon \in (0,1)$ and $t > 0$, there exists $N \in \mathbb{N}$ such that for all $n \ge N$, $M(x_n, x, t) > 1 - \varepsilon$.

Definition 2.7. [5] A sequence $\{x_n\} \subset X$ is called Cauchy sequence if for every $\varepsilon \in (0,1)$ and $t > 0$, there exists $N \in \mathbb{N}$ such that for all $m, n \ge N$, $M(x_n, x_m, t) > 1 - \varepsilon$.

Definition 2.8. [1] A mapping $T : X \to X$ is a Banach contraction if there exists $k \in (0,1)$ such that

$$M(Tx, Ty, t) \ge M(x, y, t/k), \quad \forall x, y \in X, t > 0. \tag{2.1}$$

3. A New Fuzzy Contractive Condition

Definition 3.1. Let $(X, M, *)$ be a fuzzy metric space and $T : X \to X$ a mapping. We say that T satisfies the new fuzzy contractive condition with respect to a strictly decreasing continuous function $\phi : [0,1] \to [0,1]$, with $\phi(1) = 0$ and $\phi(r) < r$ for $r \in [0,1)$, if for all $x, y \in X$ and $t > 0$:

$$\phi(M(Tx,Ty,t)) \le \max\Big\{\phi(M(x,y,t)),\; \phi(M(x,Tx,t)) * \phi(M(y,Ty,t))\Big\}. \tag{3.1}$$

Remark 3.2. Clearly, if condition (2.1) holds, then condition (3.1) is also satisfied.

Theorem 3.3. *Let $(X, M, *)$ be a complete fuzzy metric space and $T : X \to X$ satisfy the new fuzzy contractive condition with function ϕ as above. Then T has a unique fixed point $x^* \in X$, and for any $x_0 \in X$, the sequence $x_{n+1} = Tx_n$ converges to x^*.*

Proof. Let $x_0 \in X$ and define $x_{n+1} = Tx_n$ for $n \geq 0$. Define

$$a_n(t) = \phi(M(x_n, x_{n-1}, t)), \quad b_n(t) = \phi(M(x_n, x_{n+1}, t)).$$

From the contractive condition, we have

$$b_n(t) = \phi(M(Tx_n, Tx_{n-1}, t)) \leq \max\{a_n(t), a_n(t) * b_n(t)\} = a_n(t),$$

since $a_n(t) * b_n(t) \leq a_n(t)$ for $a_n(t), b_n(t) \in [0, 1]$. Since ϕ is strictly decreasing, the inequality

$\phi(M(x_{n+1}, x_n, t)) \leq \phi(M(x_n, x_{n-1}, t))$ implies $M(x_{n+1}, x_n, t) \geq M(x_n, x_{n-1}, t)$,

so the sequence $\{M(x_{n+1}, x_n, t)\}$ is monotone increasing bounded from above with 1 so its convergent to some $a(t)$. Suppose that $a(t) < 1$. Suppose

$$a(t) = \lim_{n\to\infty} M(x_{n+1}, x_n, t) < 1 \implies \phi(a(t)) < a(t) < 1,$$

which leads to a contradiction. Therefore, it is necessary that

$$\lim_{n\to\infty} M(x_{n+1}, x_n, t) = 1.$$

Let $\varepsilon > 0$ be given. Because the sequence $\{M(x_n, x_{n+1}, t)\}$ converges to 1, there exists $N \in \mathbb{N}$ such that for all $n \geq N$,

$$M(x_n, x_{n+1}, t) > 1 - \varepsilon, \quad t > 0.$$

Now, using the recursive property of the fuzzy metric and the t-norm of H-type, for any $m > n \geq N$, we have

$$M(x_n, x_m, t) \geq M\Big(x_n, x_{n+1}, \frac{t}{m-n}\Big) * \cdots * M\Big(x_{m-1}, x_m, \frac{t}{m-n}\Big),$$

and by the choice of N and the equicontinuity of $*$ at 1, this $*$-combination remains arbitrarily close to 1, which implies

$$M(x_n, x_m, t) \geq 1 - \varepsilon$$

for all $m, n \geq N$. Hence, $\{x_n\}$ is a Cauchy sequence in the fuzzy metric space $(X, M, *)$.

To show x^* is a fixed point, note

$$\begin{aligned} & \phi(M(Tx^*, x^*, t)) = \phi(M(Tx^*, Tx_n, t)) \\ \leq \quad & \max\{\phi(M(x^*, x_n, t)), \phi(M(x^*, Tx^*, t)) * \phi(M(x_n, Tx_n, t))\}. \end{aligned}$$

Letting $n \to \infty$ yields $\phi(M(Tx^*, x^*, t)) \leq \phi(1)$, and by the strict monotonicity of ϕ, we obtain $Tx^* = x^*$. Uniqueness follows similarly from the contractive condition. $\square$

Example 3.4. Let $X = [\frac{1}{2}, 1] \subset \mathbb{R}$ with the fuzzy metric

$$M(x, y, t) = \frac{t}{t + |x - y|}, \quad t > 0,$$

and the minimum t-norm $a * b = \min\{a, b\}$. Define

$$\phi(r) = r - r^2, \quad r \in [0, 1].$$

Then ϕ is continuous on $[0, 1]$, $\phi(1) = 0$, $\phi(r) < r$ for all $r \in [0, 1)$, and ϕ is strictly decreasing on $[1/2, 1]$, since $\phi'(r) = 1 - 2r < 0$ for $r > 1/2$.

Define the operator $T : X \to X$ by

$$T(x) = \frac{x}{2} + \frac{1}{4}.$$

Clearly, T maps X into itself, since for $x \in [\frac{1}{2}, 1]$, we have $T(x) \in [\frac{1}{2}, 1]$.

Verification of the new fuzzy contractive condition.

For any $x, y \in X$ and $t > 0$, we have

$$|Tx - Ty| = \frac{|x - y|}{2},$$

and therefore

$$M(Tx, Ty, t) = \frac{t}{t + |x - y|/2}.$$

Since $M(Tx, Ty, t) \geq M(x, y, t)$ and ϕ is strictly decreasing on $[1/2, 1]$, it follows that

$$\phi(M(Tx, Ty, t)) \leq \phi(M(x, y, t)).$$

Consequently,

$$\phi(M(Tx, Ty, t)) \leq \max\Big\{\phi(M(x, y, t)),\, \phi(M(x, Tx, t)) * \phi(M(y, Ty, t))\Big\}.$$

Thus, the new fuzzy contractive condition (3.1) is satisfied and $x = \frac{1}{2}$ is a fixed point.

4. Application: Iterative Filtering in Image Processing

Iterative filtering consists of repeatedly applying an image operator T to an initial image I_0, generating the sequence $I_{n+1} = T(I_n)$ until it stabilizes at a limit image I^*. Applications of fuzzy metrics and iterative filtering in image processing have been extensively studied in the literature, demonstrating both theoretical importance and practical efficiency [3, 4, 9, 10, 11, 12].

Consider a small grayscale image patch I_0 corrupted by impulse noise:

$$I_0 = \begin{bmatrix} 120 & 125 & 130 \\ 122 & 255 & 128 \\ 121 & 123 & 127 \end{bmatrix}.$$

Define T as a continuous approximation of a median filter:

$$T(I)(p) = \frac{1}{|N(p)|} \sum_{q \in N(p)} I(q).$$

The fuzzy metric and the contractive function are:

$$M(I(p), J(p), t) = \frac{t}{t + |I(p) - J(p)|}, \quad \phi(r) = r - r^2, \quad * = \min .$$

Starting with I_0, define the sequence $I_{n+1} = T(I_n)$. The iterations produce:

$$I_1 \approx \begin{bmatrix} 123 & 136 & 133 \\ 142 & 136 & 136 \\ 129 & 133 & 127 \end{bmatrix} \qquad I_2 \approx \begin{bmatrix} 134 & 135 & 134 \\ 135 & 134 & 134 \\ 133 & 134 & 133 \end{bmatrix} \qquad I_3 \approx \begin{bmatrix} 134 & 134 & 134 \\ 134 & 134 & 134 \\ 134 & 134 & 134 \end{bmatrix}.$$

The sequence converges to the unique fixed point I^*.

To verify that the operator T is fuzzy contractive, we compare pixel values in two consecutive iterations. For any pixel p and $t > 0$,

$$M(I_{n+1}(p), I_n(p), t) = \frac{t}{t + |\, I_{n+1}(p) - I_n(p)\,|}.$$

Applying $\phi(r) = r - r^2$, we obtain

$$\phi(M(I_{n+1}(p), I_n(p), t)) = M(I_{n+1}(p), I_n(p), t) - M(I_{n+1}(p), I_n(p), t)^2.$$

The contractive condition requires

$$\phi(M(I_{n+1}(p), I_n(p), t)) \le \max \Big\{ \phi(M(I_n(p), I_n(q), t)), \\ \phi(M(I_n(p), I_{n+1}(p), t)) * \phi(M(I_n(q), I_{n+1}(q), t)) \Big\},$$

with $q \in N(p)$. Since T is an averaging operator and the t-norm is of H-type, the product term remains small, so the inequality holds at each pixel. Consequently, each iteration decreases the fuzzy distance between successive images, and the sequence $\{I_n\}$ converges to a unique stable image I^*.

Acknowledgement

This research was supported by the Science Fund of the Republic of Serbia, Grant no 7632, Project Mathematical Methods in Image Processing under Uncertainty-MaMIPU and by Department of Fundamental Sciences, Faculty of Technical Sciences, University of Novi Sad, in the frame of Project "Socio-technological aspects of improving the teaching process in the English language in fundamental disciplines".

References

[1] S. Banach, "Sur les opérations dans les ensembles abstraits et leur application aux équations intégrales", *Fundamenta Mathematicae*, vol. 3, pp. 133–181, 1932.

[2] B. Carić, T. Došenović, and D. Rakić, "Fixed point of multivalued integral type of contraction mappings", *Filomat*, vol. 29, pp. 1517–1524, 2015.

[3] S. Chen and Y. Qian, "Impulse noise removal using fuzzy logic filters", *IEEE Transactions on Image Processing*, vol. 18, no. 3, pp. 678–687, 2009.

[4] T. Došenović, D. Rakić, N. Ralević, and B. Carić, "Note on Intuitionistic Fuzzy Metric-like Spaces with Application in Image Processing", *Mathematics*, vol. 12, Article 2333, 2024.

[5] A. George and P. Veeramani, "On some results in fuzzy metric spaces", *Fuzzy Sets and Systems*, vol. 64, pp. 395–399, 1994.

[6] M. Grabiec, "Fixed points in fuzzy metric spaces", *Fuzzy Sets and Systems*, vol. 27, pp. 385–389, 1988.

[7] O. Hažić and E. Pap, "Fixed Point Theory in Probabilistic Metric Spaces", *Kluwer Academic Publishers*, Dordrecht, 2001.

[8] E. P. Klement, R. Mesiar, and E. Pap, "Triangular Norms", *Kluwer Academic Publishers*, 2000.

[9] N. R. Pal and S. K. Pal, "A review on image segmentation techniques", *Pattern Recognition*, vol. 26, no. 9, pp. 1277–1294, 1993.

[10] N. M. Ralević, M. V. Paunović, and B. Iričanin, "Fuzzy metric spaces and applications in image processing", *Mathematical Montisnigri*, vol. 48, pp. 103–117, 2020.

[11] N. Ralević and M. Paunović, "Applications of fuzzy metrics in image denoising and segmentation", *Tehnički vjesnik*, vol. 28, no. 3, pp. 819–826, 2021.

[12] X. Wang and L. Zhang, "Edge-preserving image denoising based on fuzzy metrics", *Journal of Visual Communication and Image Representation*, vol. 44, pp. 1–12, 2017.

[13] L. A. Zadeh, "Fuzzy sets", *Information and Control*, vol. 8, pp. 338–353, 1965.

The 10th Conference on Mathematics in Engineering: Theory and Applications
Novi Sad, December 12-14th 2025

O PROBLEMU PAKOVANJA KVADRATA: NEIZBEŽNE TAČKE[1]

Radojka Ciganović [2]

https://doi.org/10.24867/META.2025.03 Stručni rad – prikaz

Sažetak. Neka $s(n)$ predstavlja stranicu najmanjeg kvadrata u koji se može spakovati n jediničnih kvadrata, koji se ne preklapaju. Jasno je da važi $s(n^2) = n$ i da je $s(n)$ neopadajuća funkcija. U ovom radu je dat pregled poznatih dokaza nekih jednostavnijih donjih ograničenja za $s(n)$, dobijenih uz pomoć skupova neizbežnih tačaka.

AMS klasifikacija (2020): 05B40, 52C15

Ključne reči: problem pakovanja kvadrata, metod neizbežnih tačaka, geometrijska optimizacija

1. Uvod

Definicija 1.1. Za prirodan broj n, neka je $s(n)$ stranica najmanjeg kvadrata u koji se može spakovati n jediničnih kvadrata. (Pogledati [1], problem D4)

Rezultat je očigledan kada je n potpuni kvadrat. Kako je $s(n)$ neopadajuća funkcija, zaključujemo da važi $\sqrt{n} \leq s(n) \leq \lceil \sqrt{n} \rceil$. Problem određivanja $s(n)$ kada n nije potpun kvadrat se pokazao kao nimalo lak zadatak. Nije previše teško videti da je $s(2) = 2$, dok je dokaz da je $s(5) = 2 + \frac{\sqrt{2}}{2}$ nešto komplikovaniji. Oba dokaza će biti prezentovana u nastavku rada. Iako su mnogi tvrdili da znaju kako da dokažu da je $s(6) = 3$ (videti sliku 1c), prvi publikovani dokaz datira iz 2002. godine.

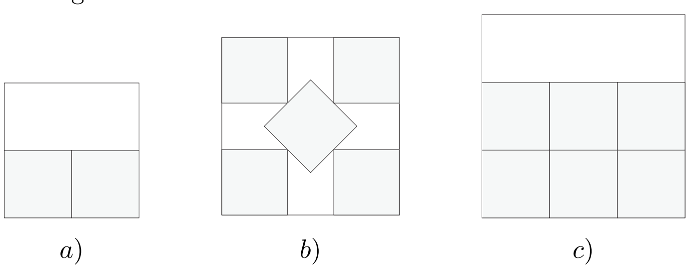

Slika 1: Optimalna pakovanja za dva, pet i šest jediničnih kvadrata

[1] Rad je podržan od strane projekta "Socio-tehnološki aspekti unapređenja nastavnog procesa na engleskom jeziku u opštim disciplinama", Departman za opšte discipline u tehnici, Fakultet tehničkih nauka, Univerzitet u Novom Sadu

[2] Departman za opšte discipline u tehnici, Fakultet tehničkih nauka, Univerzitet u Novom Sadu, e-mail: ciganovic.radojka@uns.ac.rs

Dok se gornja ograničenja za $s(n)$ dobijaju konkretnim konstrukcijama, mi ćemo za neke vrednosti funkcije $s(n)$ pronaći donja ograničenja. Pri tom ćemo koristiti metod koji predstavlja Fridmanovu modifikaciju (videti [2]) metoda koji je Stromkvist prvi upotrebio u svojim neobjavljenim beleškama (pogledati [4], beleška 1). Pre nego što to uradimo dokazaćemo nekoliko tehničkih lema[3], koje će imati ključnu ulogu u nastavku. Ove leme kažu da ako se centar jediničnog kvadrata nalazi u nekoj oblasti, tada kvadrat ima određene zajedničke tačke sa rubom posmatrane oblasti.

2. Pomoćna tvrđenja

Lema 2.1 ([2]). *Jedinični kvadrat koji je smešten u prvom kvadrantu i čiji se centar nalazi u* $[0,1]^2$ *sadrži tačku* $(1,1)$.

Dokaz. Dovoljno je pokazati da jedinični kvadrat u prvom kvadrantu koji dodiruje koordinatne ose Ox i Oy sadrži tačku $(1,1)$. Ako pretpostavimo da je kvadrat nagnut pod uglom $\theta \in (0, \frac{\pi}{2})$, onda su temena koja se nalaze na koordinatnim osama $A(0, \cos\theta)$ i $B(\sin\theta, 0)$ (videti sliku 2). Rotacijom ova dva temena jedno oko drugog za uglove $-\frac{\pi}{2}$ i $\frac{\pi}{2}$ dobijamo koordinate preostala dva temena, $C(\sin\theta + \cos\theta, \sin\theta)$ i $D(\cos\theta, \sin\theta + \cos\theta)$. Sada je prava kroz tačke C i D data jednačinom $y = \sin\theta - \operatorname{ctg}\theta(x - \sin\theta - \cos\theta)$. Uvrštavanjem $x = 1$ u dobijenu jednačinu prave dobijamo da je

$$\begin{aligned} y &= \frac{\sin^2\theta - \cos\theta(1 - \sin\theta - \cos\theta)}{\sin\theta} = \frac{1 - \cos\theta + \sin\theta\cos\theta - \sin\theta + \sin\theta}{\sin\theta} \\ &= \frac{(1-\sin\theta)(1-\cos\theta) + \sin\theta}{\sin\theta} = \frac{(1-\sin\theta)(1-\cos\theta)}{\sin\theta} + 1 \geq 1, \end{aligned}$$

pa se tačka $(1,1)$ nalazi u posmatranom kvadratu. □

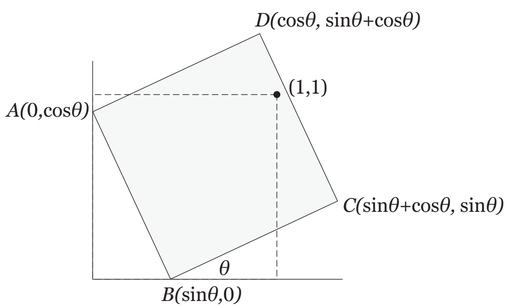

Slika 2: Jedinični kvadrat sa centrom u $[0,1]^2$

Primetimo da se prethodno tvrđenje može uopštiti. Neka je jedinični kvadrat smešten u prvom kvadrantu. Ako se centar kvadrata nalazi u pravougaoniku $[0,a] \times [0,b]$, gde je $0 < a, b \leq 1$, tada jedinični kvadrat sadrži tačku (a,b). (Pogledati [3].)

[3] U literaturi se ova tvrđenja mogu naći pod nazivom *non-avoidance lemmas*. Ovaj termin je prvi put upotrebljen u [4].

Lema 2.2 ([2]). *Neka za a i b važi $a + 2b < 2\sqrt{2}$, pri čemu je $0 < a, b \leq 1$. Tada svaki jedinični kvadrat u prvom kvadrantu sa centrom u pravougaoniku $[1, 1 + a] \times [0, b]$ sadrži bar jednu od tačaka $(1, b)$ i $(1 + a, b)$.*

Dokaz. Pokazaćemo da svaki jedinični kvadrat čiji se centar nalazi u pravougaoniku $[1, 1+a] \times [0, b]$ i koji na svojim stranicama ima tačke $(1, b)$ i $(1+a, b)$ sadrži u svojoj unutrašnjosti tačku na x-osi. Ako tačke $X(1, b)$ i $Y(1+a, b)$ leže na istoj stranici kvadrata, tvrđenje trivijalno važi.

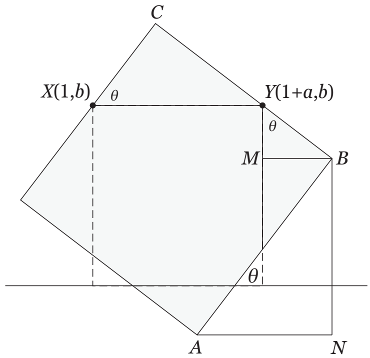

Slika 3: Jedinični kvadrat sa centrom u $[1, 1 + a] \times [0, b]$

Neka je ugao koji kvadrat zaklapa sa x-osom $\theta \in (0, \frac{\pi}{2})$ (slika 3). Pronaći ćemo koordinate "najnižeg"temena A posmatranog jediničnog kvadrata. U pravouglom $\triangle XYC$ važi $|XY| = a$, odakle dobijamo da je $|CY| = a \sin\theta$, pa je $|BY| = 1 - a\sin\theta$. Sledeći trougao koji gledamo je $\triangle YBM$, i pošto je $|MB| = (1-a\sin\theta)\sin\theta$ i $|MY| = (1-a\sin\theta)\cos\theta$, dobijamo da su koordinate temena $B(1 + a + (1 - a\sin\theta)\sin\theta,\ b - (1 - a\sin\theta)\cos\theta)$. Kako je $|AB| = 1$, u $\triangle ABN$ važi $|AN| = \cos\theta$ i $|BN| = \sin\theta$, odakle je

$$A(1 + a + (1 - a\sin\theta)\sin\theta - \cos\theta,\ b - (1 - a\sin\theta)\cos\theta - \sin\theta).$$

Posmatrajmo u nastavku funkciju $f(\theta) = \sin\theta + \cos\theta - a\sin\theta\cos\theta$. Tačka A se neće nalaziti u prvom kvadrantu ako je $f(\theta) > b$. Kako je ispunjeno

$$\begin{aligned} f'(\theta) &= \cos\theta - \sin\theta - a\cos^2\theta + x\sin^2\theta = \cos\theta - \sin\theta - a(\cos^2\theta - \sin^2\theta) \\ &= (\cos\theta - \sin\theta)(1 - a(\cos\theta + \sin\theta)), \end{aligned}$$

jednostavnim trigonometrijskim računom dobijamo da su stacionarne tačke $(\cos\theta, \sin\theta) = \left(\frac{\sqrt{2}}{2}, \frac{\sqrt{2}}{2}\right)$ i $(\cos\theta, \sin\theta) = \left(\frac{1\pm\sqrt{2a^2-1}}{2a}, \frac{1\mp\sqrt{2a^2-1}}{2a}\right)$. Direktnom proverom zaključujemo da funkcija $f(\theta)$ dostiže lokalni minimum za $\theta = \frac{\pi}{4}$. Prema tome, kada je $b < f(\frac{\pi}{4}) = \sqrt{2} - \frac{a}{2}$, teme A jediničnog kvadrata se neće nalaziti u prvom kvadrantu i postojaće tačka u unutrašnjosti kvadrata koja će biti na x-osi. □

Ova lema se najčešće primenjuje u slučaju kada je $a < 2\sqrt{2} - 2 \approx 0.828$ i $b = 1$, ili kada je $a = 1$ i $b < \sqrt{2} - \frac{1}{2} \approx 0.914$.

Lema 2.3 ([2],[4]). *Ako je centar jediničnog kvadrata smešten u $\triangle ABC$, pri čemu dužine stranica nisu veće od 1, tada kvadrat sadrži bar jedno od temena trougla.*

Dokaz. Neka su sa R_1, R_2, R_3 i R_4 označene 4 zatvorene oblasti na koje dijagonale kvadrata dele ravan (slika 4). Ukoliko bi se sva tri temena $\triangle ABC$ nalazila u jednoj, ili u dve susedne oblasti, tada se centar kvadrata ne bi nalazio u trouglu. Uzmimo zato, bez umanjenja opštosti, da se jedno teme $\triangle ABC$ nalazi u oblasti R_1, a da je drugo teme u oblasti R_3. Kako su stranice trougla dužine ≤ 1, nije moguće da se oba uočena temena trougla nalaze izvan kvadrata. $\square$

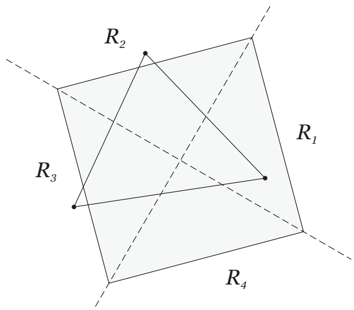

Slika 4: Jedinični kvadrat sa centrom u $\triangle ABC$

Lema 2.4 ([2])**.** *Ako se centar jediničnog kvadrata nalazi u pravougaoniku* $[0, 1] \times [0, 0.4]$, *tada kvadrat sadrži bar jedno teme pravougaonika.*

Dokaz. Uvedimo sledeće oznake za temena pravougaonika: $A(0, 0), B(0, 0.4)$, $C(1, 0.4)$ i $D(1, 0)$. Pokazaćemo da svaki jedinični kvadrat koji sadrži tačke A i B na rubu i čiji se centar nalazi unutar pravougaonika, mora da sadrži i bar jednu od tačaka C i D. Uočimo da okoliko su temena A i B na istoj stranici kvadrata, onda se i temena C i D nalaze na naspramnoj stranici kvadrata. U nastavku razlikujemo tri slučaja u zavisnosti od ugla $\theta \in (0, \frac{\pi}{2})$ pod kojim je jedinični kvadrat nagnut (slika 5).

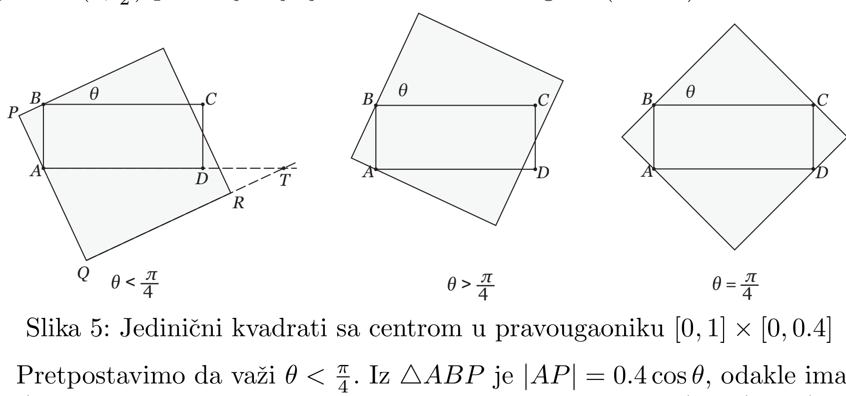

Slika 5: Jedinični kvadrati sa centrom u pravougaoniku $[0, 1] \times [0, 0.4]$

Pretpostavimo da važi $\theta < \frac{\pi}{4}$. Iz $\triangle ABP$ je $|AP| = 0.4 \cos\theta$, odakle imamo $|AQ| = 1 - 0.4\cos\theta$. Neka se tačka T nalazi u preseku $p(A, D)$ i $p(Q, R)$. Sada je u $\triangle ATQ$ ispunjeno $|AT| = \dfrac{|AQ|}{\sin\theta} = \dfrac{1 - 0.4\cos\theta}{\sin\theta} = \dfrac{1}{\sin\theta} - 0.4 \operatorname{ctg}\theta$. Dobijamo $|AT| > \sqrt{2} - 0.4 \cdot 1 > 1 = |AD|$, odakle zaključujemo da se teme D pravougaonika nalazi u jediničnom kvadratu.

Analognim razmatranjem dobijamo da je teme C u kvadratu za $\theta > \frac{\pi}{4}$, dok se u slučaju kada je $\theta = \frac{\pi}{4}$ oba temena i C i D nalaze u unutrašnjosti kvadrata (videti sliku 5). $\square$

Uočimo da pokazane leme možemo primeniti i kada se centar jediničnog kvadrata nalazi u oblasti koja se može dobiti transliranjem i rotacijom osnovnih konfiguracija.

3. Skupovi neizbežnih tačaka

Definicija 3.1 ([2])**.** Skup tačaka P u kvadratu se naziva *neizbežan skup* ako svaki jedinični kvadrat koji je smešten u kvadrat mora sadržati barem jednu tačku iz skupa P, moguće i na stranicama.

Da bismo pokazali da je $s(n) \geq k$, dovoljno je pronaći neizbežan skup P koji sadrži $n-1$ tačku u kvadratu stranice dužine k.

Teorema 3.2 ([2], [4])**.** $s(2) = s(3) = 2$.

Dokaz. Posmatrajmo jedinični kvadrat u $[0,2]^2$. Centar uočenog kvadrata se može nalaziti u nekom od sledeća četiri kvadrata: $[0,1]^2$, $[0,1]\times[1,2]$, $[1,2]\times[0,1]$ ili $[1,2]^2$. Kako na osnovu leme 2.1 znamo da se tačka $(1,1)$ mora nalaziti u posmatranom jediničnom kvadratu, zaključujemo da je skup $P = \{(1,1)\}$ neizbežan u kvadratu $[0,2]^2$ (slika 6). Na ovaj način smo pokazali $s(2) \geq 2$. Kako već znamo da važi $s(2) \leq 2$ (pogledati sliku 1a), dobijamo $s(2) = 2$. Pošto je $s(4) = 2$ i $s(3) \leq s(4)$, zaključujemo da je i $s(3) = 2$. □

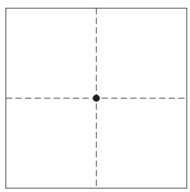

Slika 6: Kvadrat stranice 2 sadrži jednu neizbežnu tačku

Teorema 3.3 ([2], [4])**.** $s(5) = 2 + \frac{\sqrt{2}}{2}$.

Dokaz. Neka je $P = \{(1,1), (1, 1+\frac{\sqrt{2}}{2}), (1+\frac{\sqrt{2}}{2}, 1), (1+\frac{\sqrt{2}}{2}, 1+\frac{\sqrt{2}}{2})\}$. Pomoću ove četiri tačke kvadrat sa stranicom $2+\frac{\sqrt{2}}{2}$ možemo podelili na 10 oblasti: 4 kvadrata, 4 pravougaonika i 2 trougla (slika 7).

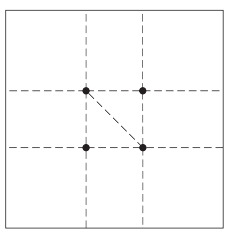

Slika 7: Četiri neizbežne tačke u $[0, 2+\frac{\sqrt{2}}{2}]^2$

Ukoliko se centar nekog jediničnog kvadrata nalazi u jednom od uočenih kvadrata, tada na osnovu leme 2.1 znamo da je i odgovarajuća tačka skupa P takođe u posmatranom jediničnom kvadratu. Ako je centar jediničnog kvadrata u nekom od pravougaonika, primenjujemo lemu 2.2, dok se u slučaju da je centar u nekom od trouglova, pošto su stranice oba trougla manje od ili jednake jedan, koristi lema 2.3. Ranije smo videli da je moguće spakovati 5 jediničnih kvadrata u kvadrat stranice $2 + \frac{\sqrt{2}}{2}$ (videti sliku 1*b*), odakle sledi tvrđenje. $\square$

Teorema 3.4 ([2]). $s(8) = 3$.

Dokaz. Tačke skupa $P = \{(0.9, 1), (1.5, 1), (2.1, 1), (1.5, 1.5), (0.9, 2), (1.5, 2), (2.1, 2)\}$ dele kvadrat sa stranicom 3 na 16 oblasti (pogledati sliku 8*a*). Ako se centar jediničnog kvadrata nalazi u nekom od četiri pravougaonika u uglovima velikog kvadrata, koristimo uopštenje leme 2.1. Za preostale pravougaonike i trouglove, isto kao u dokazu prethodnog tvrđenja, primenjujemo redom leme 2.2 i 2.3. Dobili smo da je posmatrani skup neizbežan, a kako je trivijalno $s(9) = 3$, zaključujemo $s(8) = 3$. $\square$

Teorema 3.5 ([2]). $s(15) = 4$.

Dokaz. Posmatrajmo sledeći skup

$$\begin{aligned} P = &\{(1, 1), (1.6, 1), (2.4, 1), (3, 1), (1, 1.8), (2, 1.8), (3, 1.8), \\ &(1, 2.2), (2, 2.2), (3, 2.2), (1, 3), (1.6, 3), (2.4, 3), (3, 3)\}. \end{aligned}$$

Na dva pravougaonika u centru kvadrata primenjujemo lemu 2.4 (videti sliku 8*b*), dok se za ostale oblasti koriste prve tri leme na isti način kao u prethodnim dokazima. Pronašli smo neizbežan skup sa 14 tačaka u kvadratu stranice 4, pa važi $s(15) = 4$. $\square$

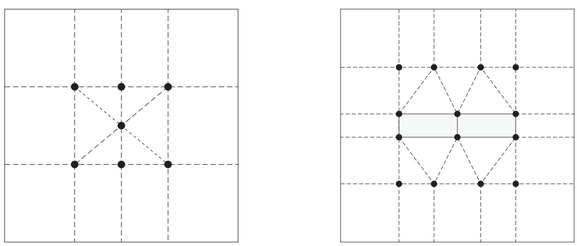

a) $s(8) \geq 3$ *b*) $s(15) \geq 4$

Slika 8: Skupovi neizbežnih tačaka

Literatura

[1] H. T. Croft, K. J. Falconer, R. K. Guy, *Unsolved Problems in Geometry*, Springer Science+Business Media, New York, 1991

[2] E. Friedman, "Packing Unit Squares in Squares: A Survey and New Results", *Electron. J. Comb.*, Dynamic Survey #DS7, (1998, last version 2009), edited by D. Ellsworth `kingbird.myphotos.cc/packing/squares.html`)

[3] W. Stromquist, "Packing 10 or 11 Unit Squares in a Square", *Electron. J. Comb.*, **10** (2003), #R8

[4] W. Stromquist, "Packing Unit Squares Inside Squares, I, II, III", (1984), unpublished memoranda (`walterstromquist.com/publications.html`)

The 10th Conference on Mathematics in Engineering: Theory and Applications
Novi Sad, December 12-14th 2025

SOME VERTEX-DEGREE-BASED TOPOLOGICAL INDICES OF CATACONDENSED CORONOIDS

Lidija Čomić[1] and Nebojša Ralević[2]

https://doi.org/10.24867/META.2025.04 Short communication

Abstract. We compute several vertex-degree-based topological indices of graphs defined by catacondensed coronoid systems. We do this by using our recently proposed formulae for graphs defined by finite sets of hexagons of arbitrary topology in the hexagonal grid, and the associated M-polynomial.

AMS Mathematics Subject Classification (2020): 05C09, 05C92

Key words and phrases: topological graph indexes, vertex-degree-based indexes, M-polynomial, catacondensed coronoids

1. Introduction

Let S be a set of h hexagons in the hexagonal grid, which may or may not be (simply) connected, with β_0 connected components, β_1 holes and the Euler characteristic $\chi = \beta_0 - \beta_1$. Let $G = (V, E)$ be the simple plane graph with n vertices and m edges, induced by S: the vertices and edges of G correspond to the vertices and edges of the hexagons in S, respectively, in the obvious manner. In chemical graph theory, such sets are used to model molecules. Simply connected sets S are called benzenoid systems [6], and connected sets with one hole are coronoid systems [4].

The degree d_v of a vertex v is equal to the number of the edges incident to v. The number of the vertices in V of degree i is denoted by n_i, $i \in \{2,3\}$. The number of the edges connecting a vertex of degree i to a vertex of degree j (type i,j edges) is denoted by $m_{i,j}$, $i,j \in \{2,3\}$, $i \leq j$. Boundary edges are incident to exactly one hexagon in S. Boundary vertices are incident to boundary edges. The number of boundary edges of type 3,3 is denoted by $m^*_{3,3}$. Non-boundary vertices are called interior. Their number is denoted by n_i.

A topological index of a graph G is a real number associated with G. The general form of a vertex-degree-based topological index $I(G)$ of a graph G is given by

$$I(G) = \sum_{uv \in E(G)} f(d_u, d_v),$$

[1]Department of Fundamental Sciences, Faculty of Technical Sciences, University of Novi Sad, e-mail: comic@uns.ac.rs

[2]Department of Fundamental Sciences, Faculty of Technical Sciences, University of Novi Sad, e-mail: nralevic@uns.ac.rs

where f is a real function such that $f(x,y) = f(y,x)$. Several dozens of well-known indices have been defined, varying over the choices of f. In chemical graph theory, graph indices have been repeatedly shown to be apt for describing and predicting chemical, physical and biological properties of associated chemical compounds.

We will consider five such indices, obtained by choosing f as follows:

1. $f(x,y) = x + y$ for the first Zagreb index M_1 [8],
2. $f(x,y) = xy$ for the second Zagreb index M_2 [7],
3. $f(x,y) = (xy)^\alpha$, $\alpha \in \mathbb{N}$, for the general Randić index R_α (variable second Zagreb index ${}^vM_2$ [9]),
4. $f(x,y) = 1/(xy)$ for the second modified Zagreb index ${}^mM_2$ (first order overall index [1]),
5. $f(x,y) = \frac{x^2+y^2}{xy} = \frac{x}{y} + \frac{y}{x}$ for the symmetric division deg index SDD [10].

It is well known [5] that these indices can alternatively be obtained from the M-polynomial

$$M(x,y) = m_{2,2}x^2y^2 + m_{2,3}x^2y^3 + m_{3,3}x^3y^3$$

of G through differentiation or integration as follows

1. $M_1 = (D_x + D_y)(M(x,y))|_{x=y=1}$,
2. $M_2 = (D_xD_y)(M(x,y))|_{x=y=1}$,
3. $R_\alpha =^v M_2 = (D_x^\alpha D_y^\alpha)(M(x,y))|_{x=y=1}$,
4. ${}^mM_2 = (S_xS_y)(M(x,y))|_{x=y=1}$
5. $SDD = (D_xS_y + D_yS_x)(M(x,y))|_{x=y=1}$,

where

$$D_x(M(x,y)) = x\frac{\partial M(x,y)}{\partial x},\ D_y(M(x,y)) = y\frac{\partial M(x,y)}{\partial y},$$

and

$$S_x(M(x,y)) = \int_0^x \frac{M(t,y)}{t}dt,\ S_y(M(x,y)) = \int_0^y \frac{M(x,t)}{t}dt.$$

For simply connected sets S, there are different formulas for $m_{2,2}$, $m_{2,3}$ and $m_{3,3}$ in terms of other, easier to determine and chemically significant, graph invariants [6]. Interestingly, despite the long history and large body of research on vertex-degree-based topological indices for simply connected sets S, these formulae have only recently been extended to sets S of arbitrary topology by the present authors [2] as follows:

$$
\begin{array}{lrcl}
(1.1) \quad & m_{2,2} & = & m^*_{3,3} + 6\chi \\
& m_{2,3} & = & 4h - 2n_i - 4\chi - 2m^*_{3,3} \\
& m_{3,3} & = & h + n_i - \chi + m^*_{3,3}
\end{array}
$$

Here, we further demonstrate the versatility of our formulae by determining the numbers $m_{2,2}$, $m_{2,3}$, $m_{3,3}$, the M-polynomial and the associated indices for catacondensed coronoid systems.

2. Vertex-degree-based topological indices of catacondensed coronoid systems

Catacondensed coronoid system S has exactly one hole and no inner vertices (thus, $\chi = 1 - 1 = 0$ and $n_i = 0$). The hexagons in S are in one of the two configurations, called L_2 (linear) and A_2 (angle or corner), as illustrated in Figure 1 (a). They can be cyclically ordered so that each hexagon shares an edge with the previous and the next one, and there are no more adjacencies among the hexagons in S (see Figure 1 (b)).

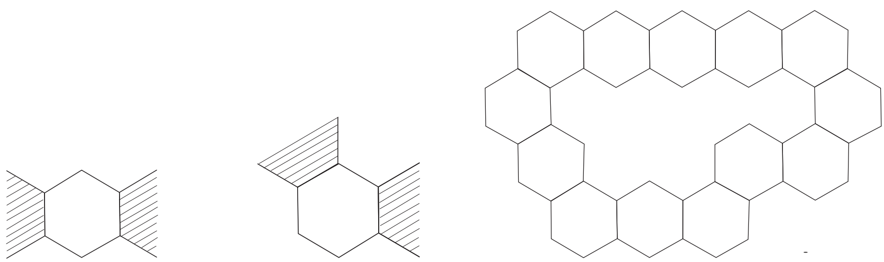

(a) (b)

Figure 1: (a) A linear (left) and corner (right) hexagon. (b) A coronoid system with $a = 8$ and $l = 5$.

We will obtain the M-polynomial and the associated indices of a catacondensed coronoid system with h hexagons, among which there are a corners and $l = h - a$ linear hexagons.

Theorem 2.1. *For the graph G of a catacondensed coronoid system with a corners and l linear hexagons, it holds*

$$M(G) \quad = \quad ax^2y^2 + (2a + 4l)x^2y^3 + (2a + l)x^3y^3.$$

Proof. We have that

$$
\begin{array}{rcl}
m_{2,2} & = & m^*_{3,3} = a \\
m_{2,3} & = & 4h - 2m_{2,2} = 4h - 2a = 2a + 4l \\
m_{3,3} & = & h + m_{2,2} = h + a = 2a + l
\end{array}
$$

The first equality follows from (1.1), and the fact that type 2,2 and type 3,3 edges come in pairs which belong to corner hexagons (see Figure 1 (a)). The second and third equalities follow from the first one and from (1.1).

□

Corollary 2.2. *For the graph of a catacondensed coronoid system, it holds*

$$\begin{aligned} M_1 &= (D_x + D_y)(M(x,y))|_{x=y=1} \\ &= 4a + 5(2a+4l) + 6(2a+l) \\ &= 26a + 26l, \end{aligned}$$

$$\begin{aligned} M_2 &= (D_x D_y)(M(x,y))|_{x=y=1} \\ &= D_x(2ax^2y^2 + 3(2a+4l)x^2y^3 + 3(2a+l)x^3y^3)|_{x=y=1} \\ &= (4ax^2y^2 + 6(2a+4l)x^2y^3 + 9(2a+l)x^3y^3)|_{x=y=1} \\ &= 34a + 33l, \end{aligned}$$

$$\begin{aligned} R_\alpha &= (D_x^\alpha D_y^\alpha)(M(x,y))|_{x=y=1} \\ &= D_x(2^\alpha ax^2y^2 + 3^\alpha(2a+4l) + 3^\alpha(2a+l)x^3y^3)|_{x=y=1} \\ &= (4^\alpha ax^2y^2 + 6^\alpha(2a+4l)x^2y^3 + 9^\alpha(2a+l)x^3y^3)|_{x=y=1} \\ &= (4^\alpha + 2\cdot 6^\alpha + 2\cdot 9^\alpha)a + (4\cdot 6^\alpha + 9^\alpha)l, \end{aligned}$$

$$\begin{aligned} {}^mM_2 &= (S_x S_y)(M(x,y))|_{x=y=1} \\ &= S_x(\int_0^y (ax^2t + (2a+4l)x^2t^2 + (2a+l)x^3t^2)dt)|_{x=y=1} \\ &= S_x((\tfrac{1}{2}ax^2y^2 + \tfrac{1}{3}(2a+4l)x^2y^3 + \tfrac{1}{3}(2a+l)x^3y^3))|_{x=y=1} \\ &= (\int_0^x (\tfrac{1}{2}aty^2 + \tfrac{1}{3}(2a+4l)ty^3 + \tfrac{1}{3}(2a+l)t^2y^3)dt)|_{x=y=1} \\ &= (\tfrac{1}{4}ax^2y^2 + \tfrac{1}{6}(2a+4l)x^2y^3 + \tfrac{1}{9}(2a+l)x^3y^3))|_{x=y=1} \\ &= \tfrac{29}{36}a + \tfrac{7}{9}l, \end{aligned}$$

$$\begin{aligned} SDD &= (D_x S_y + D_y S_x)(M(x,y))|_{x=y=1} \\ &= (D_x(\tfrac{1}{2}ax^2y^2 + \tfrac{1}{3}(2a+4l)x^2y^3 + \tfrac{1}{3}(2a+l)x^3y^3) + \\ &\quad D_y(\tfrac{1}{2}ax^2y^2 + \tfrac{1}{2}(2a+4l)x^2y^3 + \tfrac{1}{3}(2a+l)x^3y^3))|_{x=y=1} \\ &= (ax^2y^2 + \tfrac{2}{3}(2a+4l)x^2y^3 + (2a+l)x^3y^3 + \\ &\quad ax^2y^2 + \tfrac{3}{2}(2a+4l)x^2y^3 + (2a+l)x^3y^3))|_{x=y=1} \\ &= (a + \tfrac{2}{3}(2a+4l) + (2a+l) + a + \tfrac{3}{2}(2a+4l) + (2a+l) \\ &= \tfrac{31}{3}a + \tfrac{32}{3}l. \end{aligned}$$

3. Discussion

We have determined several vertex-degree-based indices of catacondensed coronoid systems using our recently proposed formulae [2] and the associated M-polynomial. In that way, we extended our previous work on a special class of such systems, called fenestrenes [3]. We are currently working on developing analogous formulae for other chemically significant grids, which have been completely neglected in this regard despite considerable amount of attention given to the hexagonal grid.

Acknowledgement

This work has been partially supported by the Science Fund of the Republic of Serbia, #GRANT no. 7632, the project "Mathematical Methods in Image Processing under Uncertainty" MaMIPU and by the project "Socio-technological aspects of improving the teaching process in the English language in fundamental disciplines".

References

[1] D. Bonchev, "Overall connectivity - a next generation molecular connectivity", *Journal of Molecular Graphics and Modelling*, 20, pp. 65-75, 2001.

[2] L. Čomić and N. Ralević, "Vertex-Degree-Based Topological Indices of Arbitrary Sets of Hexagons in the Regular Hexagonal Grid", *Applicable Analysis and Discrete Mathematics*, 2024.

[3] L. Čomić, N. Ralević, and S. Tošić, "Vertex-degree-based topological indices of fenestrene", In *The 6th Conference on Mathematics in Engineering: Theory and Applications, Novi Sad*, pp. 75-79, 2021.

[4] S. J. Cyvin, J. Brunvoll, and B. N. Cyvin, , *Theory of Coronoid Hydrocarbons*, volume 54 of *Lecture Notes in Chemistry*, Springer-Verlag, Berlin Heidelberg, 1991.

[5] E. Deutsch and S. Klavžar, "M-Polynomial and Degree-Based Topological Indices", *Iranian Journal of Mathematical Chemistry*, 6(2), pp. 93-102, 2015.

[6] I. Gutman and S. J. Cyvin, *Introduction to the Theory of Benzenoid Hydrocarbons*, Springer-Verlag, 1989.

[7] I. Gutman, B. Ruščić, N. Trinajstić, and C. F. Wilcox, "Graph theory and molecular orbitals. XII. Acyclic polyenes", *Journal of Chemical Physics*, 62, pp. 3399-3405, 1975.

[8] I. Gutman and N. Trinajstić, "Graph theory and molecular orbitals. Total π-electron energy of alternant hydrocarbons", *Chemical Physics Letters*, 17, pp. 535-538, 1972.

[9] A. Miličević and S. Nikolić, "On Variable Zagreb Indices", *Croatica Chemica Acta*, 77(1-2), pp. 97-101, 2004.

[10] D. Vukičević and M. Gašperov, "Bond Additive Modeling 1. Adriatic Indices", *Croatica Chemica Acta*, 83(3), pp. 243-260, 2010.

The 10th Conference on Mathematics in Engineering: Theory and Applications
Novi Sad, December 12-14th 2025

GENERAL ALGEBRAIC SOLUTION OF A FUZZY SYLVESTER MATRIX EQUATION [1]

Đorđe Dragić [2]

https://doi.org/10.24867/META.2025.05 Original scientific article

Abstract. In this paper, we propose a new algorithm based on {1}-inverses for finding all algebraic (strong) solutions of a fuzzy Sylvester matrix equation (FSME), $A\tilde{X} + \tilde{X}B = \tilde{C}$, where the coefficient matrices A and B are real matrices of orders $n \times n$ and $m \times m$, respectively, while $\tilde{C}$ is a given matrix of fuzzy numbers. The proposed method is illustrated through a numerical example.

AMS Mathematics Subject Classification (2020): 03E72, 15A09, 93C05

Key words and phrases: fuzzy Sylvester matrix equation, generalized inverses, general solution

1. Introduction

In numerous practical applications involving systems of linear equations, the available data are often imprecise or uncertain. Consequently, there is a need to develop methods for solving systems of equations where certain parameters are represented as fuzzy numbers. A method for solving square fuzzy linear systems (FLS), $A\tilde{X} = \tilde{B}$, whose coefficient matrix A is real and $\tilde{B}$ is an arbitrary fuzzy number vector, was first introduced by Friedman et al. in [2]. In [5], Mihailović et al. presented the first algorithm for obtaining all solutions of rectangle FLS using the Moore-Penrose inverse of the coefficient matrix. In [1], Dragić et al. proposed the straightforward method for obtaining all algebraic (strong) solutions of an arbitrary dual fuzzy linear system (DFLS), $A\tilde{X} + \tilde{C} = B\tilde{X} + \tilde{D}$, where the coefficient matrices A and B are arbitrary real $m \times n$ matrices and $\tilde{C}$ and $\tilde{D}$ are given fuzzy number vectors.

In 2011, Salkuyeh [6] investigated the existence and uniqueness of a fuzzy solution to the fuzzy Sylvester matrix equation (FSME) of the form $A\tilde{X}+\tilde{X}B = \tilde{C}$, when matrices A and B are M-matrices. Salkuyeh transformed FSME into DFLS by using Kronecker products. Very recently, in [3], He et al. established an algorithm to obtain general strong fuzzy solutions to the FSME by using

[1]The author acknowledge the financial support of Department of Fundamental Sciences, Faculty of Technical Sciences, University of Novi Sad, in the frame of Project "Socio-technological aspects of improving the teaching process in the English language in fundamental disciplines".

[2]Department of Fundamental Sciences, Faculty of Technical Sciences, University of Novi Sad, e-mail: djordje.dragic@uns.ac.rs

the BT inverse of the coefficient matrix, under certain additional conditions on the involved matrices, including their nonnegativity (or nonpositivity).

The main goal of this paper is to characterize the general algebraic (strong) solution of the FSME. Using the Kronecker product, we transform the given FSME into a dual fuzzy linear system, which is then extended to a classical system of linear equations, for which a necessary and sufficient condition for the existence of representative solutions (see page 4) is established. Furthermore, an algorithm based on the $\{1\}$-inverses is proposed to obtain the general algebraic solution, and its effectiveness is demonstrated through an example.

2. Preliminaries and previous research

Let us denote with $\mathcal{M}^{m\times n}$ the class of all $m \times n$ real matrices, $m, n \in \mathbb{N}$. For any $F \in \mathcal{M}^{m\times n}$, let a matrix $G \in \mathcal{M}^{n\times m}$ be such that it fulfills equation $FGF = F$. A such matrix G is called an $\{1\}$-inverse of F, and it will be denoted by $F^{(1)}$, and $F\{1\}$ denotes sets of all $\{1\}$-inverses of F.

Recall that a general solution of a classical linear system $AX = B$ is given in the next form:

$$X = A^{(1)}B + (I_n - A^{(1)}A)V, \quad A \in \mathcal{M}^{m\times n},\ B \in \mathcal{M}^{m\times 1}, \tag{2.1}$$

where $A^{(1)} \in A\{1\}$, $V \in \mathcal{M}^{n\times 1}$ is arbitrary, and I_n is identity matrix of size n.

A fuzzy number is a mapping $\tilde{u} : \mathbb{R} \to [0, 1]$ so that for each $\alpha \in (0, 1]$ the α-level set, $[\tilde{u}]^\alpha = \{x \in \mathbb{R} : \tilde{u}(x) \geq 0\}$, $\forall\alpha \in (0, 1]$, is a nonempty, closed and bounded interval, and support of $\tilde{u}$ defined as $supp(\tilde{u}) = \overline{\{x \in \mathbb{R} : \tilde{u}(x) > 0\}}$ is a nonempty, closed and bounded interval. The set of all fuzzy numbers is denoted by $\tilde{\mathcal{J}}$.

A fuzzy number $\tilde{u} \in \tilde{\mathcal{J}}$ is given in the parametric form $(\underline{u}, \overline{u})$, where the upper branch $\overline{u} : [0, 1] \to \mathbb{R}$ is non-increasing and left continuous, $\overline{u}(\alpha) = \sup[\tilde{u}]^\alpha$, whereas the lower branch $\underline{u} : [0, 1] \to \mathbb{R}$ is non-decreasing and left continuous, $\underline{u}(\alpha) = \inf[\tilde{u}]^\alpha$, such that $\underline{u}(\alpha) \leq \overline{u}(\alpha)$, for each $\alpha \in [0, 1]$. The addition, scalar multiplication and equality of fuzzy numbers are based on the interval arithmetic and the fact that α-cuts of a fuzzy number $\tilde{u}$, given by $[\tilde{u}]^\alpha = [\underline{u}(\alpha), \overline{u}(\alpha)]$, $\alpha \in [0, 1]$, are closed intervals (for more details, we refer the reader to [1, 2]).

Definition 2.1 ([4]). Let $P = [p_{ij}] \in \mathcal{M}^{m\times n}$, $p_i = (p_{1i}, p_{2i}, \dots, p_{mi})^T$ be the i-th column of P, $i = 1, \dots, n$, then the mn-dimensional vector $\mathrm{vec}(P) = V_P = \begin{bmatrix} p_1 & p_2 & \dots & p_n \end{bmatrix}^T$ is called the extension on column of the matrix P.

Definition 2.2 ([4]). Let $P \in \mathcal{M}^{m\times n}$, $Q \in \mathcal{M}^{p\times q}$. Then the Kronecker product is defined by $P \otimes Q = \begin{bmatrix} p_{11}Q & \cdots & p_{1n}Q \\ \vdots & & \vdots \\ p_{m1}Q & \cdots & p_{mn}Q \end{bmatrix}$, where $P \otimes Q \in \mathcal{M}^{mp\times nq}$. It holds $\mathrm{vec}(AXB) = (B^T \otimes A)\mathrm{vec}(X)$.

Let $\tilde{X} = (\tilde{x}_1, \dots, \tilde{x}_n)^T$ denotes a fuzzy number vector, where $\tilde{x}_i \in \tilde{\mathcal{J}}$, $i = 1, \dots, n$. Let $\mathcal{V}_n$ denotes the class of all n-dimensional fuzzy number vectors.

Let $X = (\underline{x}_1, \ldots, \underline{x}_n, -\overline{x}_1, \ldots, -\overline{x}_n)^T$ denotes the associated $2n \times 1$ classical functional vector and let $\mathcal{F}$ denotes a class of all classical functional vectors. The vector $X \in \mathcal{F}$ is called the representative vector if all its components are adequate functions on the unit interval that represent the upper and lower branches of some fuzzy number vector $\tilde{X} \in \mathcal{V}_n$. A class of all representative classical functional vectors is denoted by $\mathcal{F}^{\mathcal{R}}$. For each $\tilde{X} \in \mathcal{V}_n$, the associated $n \times 1$ classical functional vectors are $\underline{X} = (\underline{x}_1, \ldots, \underline{x}_n)^T$ and $\overline{X} = (\overline{x}_1, \ldots, \overline{x}_n)^T$. The zero vector is denoted by O.

For each matrix $M \in \mathcal{M}^{m \times n}$, let $S_M \in \mathcal{M}^{2m \times 2n}$ be given by

$$S_M = \begin{bmatrix} M^+ & M^- \\ M^- & M^+ \end{bmatrix}, \tag{2.2}$$

where for each matrix $M \in \mathcal{M}^{m \times n}$ we denote $M^+ = \frac{1}{2}(M + |M|)$ and $M^- = \frac{1}{2}(|M| - M)$, $|M| = [|m_{ij}|]$.

Definition 2.3 ([3])**.** The fuzzy matrix equation

$$A\tilde{X} + \tilde{X}B = \tilde{C}, \tag{2.3}$$

where $A = [a_{ij}] \in \mathcal{M}^{n \times n}$, $B = [b_{ij}] \in \mathcal{M}^{m \times m}$, $\tilde{C} = [\tilde{c}_{ij}]$ is a $n \times m$ matrix of fuzzy numbers, and $\tilde{X}$ is a $n \times m$ unknown matrix of fuzzy numbers, is called a fuzzy Sylvester matrix equation (FSME).

A matrix of fuzzy numbers $\tilde{U}$, $\mathrm{vec}(\tilde{U}) = \tilde{V}_{\tilde{U}} \in \mathcal{V}_{2mn}$, $V_{\tilde{U}} \in \mathcal{F}^{\mathcal{R}}$, is a (strong) solution of (2.3) iff it holds:

$$A\tilde{U} + \tilde{U}B = \tilde{C}.$$

Theorem 2.4 ([3])**.** *Let $A \in \mathcal{M}^{n \times n}$, $B \in \mathcal{M}^{m \times m}$, $\tilde{X}$, and $\tilde{C}$ be $n \times m$ matrices of fuzzy numbers. Then, $A\tilde{X} + \tilde{X}B = \tilde{C}$ is equivalent to*

$$(I_m \otimes A)\tilde{V}_{\tilde{X}} + (B^T \otimes I_n)\tilde{V}_{\tilde{X}} = \tilde{V}_{\tilde{C}}, \tag{2.4}$$

where I_n and I_m denote the identity matrices of order n and m, respectively.

3. A new algorithm for solving FSME

Denote $P = I_m \otimes A$ and $Q = B^T \otimes I_n$. The matrix equation (2.4) can be extended to the following crisp form

$$\begin{bmatrix} P^+ & P^- \\ P^- & P^+ \end{bmatrix} \begin{bmatrix} \underline{V_{\tilde{X}}} \\ -\overline{V}_{\tilde{X}} \end{bmatrix} + \begin{bmatrix} Q^+ & Q^- \\ Q^- & Q^+ \end{bmatrix} \begin{bmatrix} \underline{V_{\tilde{X}}} \\ -\overline{V}_{\tilde{X}} \end{bmatrix} = \begin{bmatrix} \underline{V_{\tilde{C}}} \\ -\overline{V}_{\tilde{C}} \end{bmatrix}.$$

For each matrix $M \in \mathcal{M}^{m \times n}$, let $S_M \in \mathcal{M}^{2m \times 2n}$ be given by (2.2). Therefore, the matrix equation (2.4) can be extended into crisp systems of linear equations as follows:

$$(S_P + S_Q)V_{\tilde{X}}(\alpha) = V_{\tilde{C}}(\alpha),\ \alpha \in [0, 1], \tag{3.1}$$

(we write $(S_P + S_Q)V_{\tilde{X}} = V_{\tilde{C}})$ associated to the system (2.4). Denote the solution set of (3.1) with $\mathcal{ASS}$. Let us denote the subset of $\mathcal{ASS}$ which contains all representative solutions of (3.1) with $\mathcal{ASS}^{\mathcal{R}}$, i.e.,

$$\mathcal{ASS}^{\mathcal{R}}=\{V_{\tilde{X}} \in \mathcal{F}^{\mathcal{R}} |\ (S_P+S_Q)V_{\tilde{X}} = V_{\tilde{C}}\} \subseteq \{X \in \mathcal{F} |\ (S_P+S_Q)V_{\tilde{X}} = V_{\tilde{C}}\}=\mathcal{ASS}.$$

If $\mathcal{ASS}^{\mathcal{R}} \neq \emptyset$, the family (3.1) is said to be $\mathcal{R}$-consistent.

Let $G \in \mathcal{M}^{mn\times mn}$, $G = [g_{ij}] \in (P + Q)\{1\}$, and $|G| = [|g_{ij}|]$. Let $S_G \in \mathcal{M}^{2mn\times 2mn}$ be given by (2.2). The next theorem presents a necessary and sufficient condition for the $\mathcal{R}$-consistency of (3.1).

Theorem 3.1. *Let $A \in \mathcal{M}^{n\times n}$, $B \in \mathcal{M}^{m\times m}$ be the coefficient matrices of the FSME (2.3) for a given $n \times m$ matrix of fuzzy numbers $\tilde{C}$. Let $P = I_m \otimes A$ and $Q = B^T \otimes I_n$ be the coefficient matrices of the system (2.4) associated to the FSME (2.3), for given $\tilde{V_{\tilde{C}}} = \mathrm{vec}(\tilde{C}) \in \mathcal{V}_{mn}$. Let $X^* = S_G V_{\tilde{C}}$, where $G \in (P + Q)\{1\}$, and $\mathsf{R} = V_{\tilde{C}} - (S_P + S_Q)X^*$.*

The associated family of linear systems (3.1) for the system (2.4) is $\mathcal{R}$-consistent iff there exist $\mathsf{L} = \begin{bmatrix} \Lambda \\ -\Lambda \end{bmatrix}$, where $\Lambda = (\lambda_1(\alpha), \ldots, \lambda_{mn}(\alpha))^T$, such that $(S_P + S_Q)\mathsf{L} = \mathsf{O}$, and $\mathsf{T} = \begin{bmatrix} \Theta \\ \Theta \end{bmatrix}$, where $\Theta = (\theta_1(\alpha), \ldots, \theta_{mn}(\alpha))^T$, such that $(S_P + S_Q)\mathsf{T} = \mathsf{R}$, and $X^* + \frac{1}{2}\mathsf{L} + \mathsf{T} \in \mathcal{F}^R$.

Moreover,

$$\mathcal{ASS}^{\mathcal{R}} = \left\{ V_{\tilde{X}} \in \mathcal{F}^R \,|\, V_{\tilde{X}} = X^* + \frac{1}{2}\mathsf{L} + \mathsf{T},\ (S_P + S_Q)\mathsf{L} = \mathsf{O},\ (S_P + S_Q)\mathsf{T} = \mathsf{R} \right\}.$$

Proof. The proof is analogous to the proof of Theorem 1 in [1]. □

Based on Theorem 3.1, we propose a straightforward method for obtaining the general algebraic solution of the fuzzy Sylvester matrix equation:

Algorithm

Step 1. Transform the given FSME (2.3) into the equation (2.4) and compute $X^* = S_G V_{\tilde{C}}$, where $G \in (P + Q)\{1\}$.

Step 2. Compute a $mn \times 1$ functional vector Λ such that $(P + Q)\Lambda = \mathsf{O}$.

Step 3. For X^* obtained by Step 1, compute a $mn \times 1$ functional vector W such that $W = \underline{V_{\tilde{C}}} - [P^+ + Q^+\ P^- + Q^-]X^*$.

Step 4. If it exists, compute a $mn \times 1$ functional vector Θ such that $(|P| + |Q|)\Theta = W$, where W is obtained by Step 3, else, FSME has no solution.

Step 5. If it exists, compute the representative solution $V_{\tilde{X}} = X^* + \frac{1}{2}\mathsf{L} + \mathsf{T}$ of (3.1), else, FSME has no solution.

Step 6. By inverse operation of the vec operation (which is defined in Definition 2.1), we transform $V_{\tilde{X}}$ into matrix $\tilde{X}$, and we get the general fuzzy solutions of (2.3).

Notice that from all determined L and T by Step 2 and Step 4, we only consider such that for each $\alpha \in [0, 1]$ it holds $\Theta \leq \frac{\overline{X^*} - \underline{X^*}}{2}$, and all components of $\underline{X}^* + \frac{1}{2}\Lambda + \Theta$ are non-decreasing and left-continuous functions on the unite interval, whereas all components of $\overline{X}^* + \frac{1}{2}\Lambda - \Theta$ are non-increasing and left-continuous functions. Obviously, for such Λ and Θ, the family of intervals $\{[\underline{x}_i^*(\alpha)+\frac{1}{2}\lambda_i(\alpha)+\theta_i(\alpha), \overline{x}_i^*(\alpha)+\frac{1}{2}\lambda_i(\alpha)-\theta_i(\alpha)] \mid \alpha \in [0,1]\}$, for all i, determines α-cuts of $\tilde{V}_{\tilde{X}}$, which is a solution of the system (2.4).

Example 3.2. Consider the fuzzy Sylvester matrix equation $A\tilde{X} + \tilde{X}B = \tilde{C}$:

$$\begin{bmatrix} 1 & 0 \\ 0 & 2 \end{bmatrix} \begin{bmatrix} \tilde{x}_{11} & \tilde{x}_{12} \\ \tilde{x}_{21} & \tilde{x}_{22} \end{bmatrix} + \begin{bmatrix} \tilde{x}_{11} & \tilde{x}_{12} \\ \tilde{x}_{21} & \tilde{x}_{22} \end{bmatrix} \begin{bmatrix} -1 & 0 \\ 0 & \frac{1}{2} \end{bmatrix} = \tilde{C},$$

where

$$\tilde{C} = \begin{bmatrix} (-2+2\alpha, 2-2\alpha) & (\frac{3}{2}+3\alpha, 6-\frac{3}{2}\alpha) \\ (-1+3\alpha, 5-3\alpha) & (\frac{5}{2}\alpha, 5-\frac{5}{2}\alpha) \end{bmatrix},$$

for any $\alpha \in [0,1]$. According to (2.4), the given FSME is equivalent to the following equation:

$$\begin{bmatrix} 1 & 0 & 0 & 0 \\ 0 & 2 & 0 & 0 \\ 0 & 0 & 1 & 0 \\ 0 & 0 & 0 & 2 \end{bmatrix} \begin{bmatrix} \tilde{x}_{11} \\ \tilde{x}_{21} \\ \tilde{x}_{12} \\ \tilde{x}_{22} \end{bmatrix} + \begin{bmatrix} -1 & 0 & 0 & 0 \\ 0 & -1 & 0 & 0 \\ 0 & 0 & \frac{1}{2} & 0 \\ 0 & 0 & 0 & \frac{1}{2} \end{bmatrix} \begin{bmatrix} \tilde{x}_{11} \\ \tilde{x}_{21} \\ \tilde{x}_{12} \\ \tilde{x}_{22} \end{bmatrix} = \begin{bmatrix} \tilde{c}_{11} \\ \tilde{c}_{21} \\ \tilde{c}_{12} \\ \tilde{c}_{22} \end{bmatrix}.$$

The one of $\{1\}$-inverses of the matrix $P+Q = I_2 \otimes A + B^T \otimes I_2$ is in the next form:

$$G = (P+Q)^{(1)} = \begin{bmatrix} 0 & 0 & 0 & 0 \\ 0 & 1 & 0 & 0 \\ 0 & 0 & \frac{2}{3} & 0 \\ 0 & 0 & 0 & \frac{2}{5} \end{bmatrix}.$$

According to Algorithm, Step 1, we have:

$$X^* = S_G V_{\tilde{C}} = (0,\ -1+3\alpha,\ 1+2\alpha,\ \alpha,\ 0,\ -5+3\alpha,\ -4+\alpha,\ -2+\alpha)^T.$$

Step 2: $\Lambda = \big(f(\alpha), 0, 0, 0\big)^T$ is a solution vector of $(P+Q)\Lambda = \mathsf{O}$, where $y = f(\alpha)$, $\alpha \in [0,1]$, is function on the unite interval.
Next, we have:

$$W = \underline{V_{\tilde{C}}} - [P^+ + Q^+ \ P^- + Q^-]X^* = \big(-2+2\alpha,\ 6-6\alpha,\ 0,\ 0\big)^T.$$

Each system in the family of classical systems $(|P|+|Q|)\Theta = W$ has a unique solution: $\Theta = \big(-1+\alpha,\ 2-2\alpha,\ 0,\ 0\big)^T$.
Finally, the general solution of the family (3.1), $V_{\tilde{X}} \in \mathcal{ASS}^R$, is $V_{\tilde{X}} = \begin{bmatrix} \underline{V_{\tilde{X}}} & -\overline{V_{\tilde{X}}} \end{bmatrix}^T$,

$$\underline{V_{\tilde{X}}} = \underline{X^*} + \frac{1}{2}\Lambda + \Theta = \begin{bmatrix} -1+\alpha+\frac{1}{2}f(\alpha) \\ 1+\alpha \\ 1+2\alpha \\ \alpha \end{bmatrix},$$

$$\overline{V_{\tilde{X}}} = \overline{X^*} + \frac{1}{2}\Lambda - \Theta = \begin{bmatrix} 1-\alpha+\frac{1}{2}f(\alpha) \\ 3-\alpha \\ 4-\alpha \\ 2-\alpha \end{bmatrix},$$

where f is a feasible function defined on the unite interval. Let $f(\alpha) = k\alpha + n$, $k, n \in \mathbb{R}$. In order to obtain a representative vector X (all the components must be fuzzy numbers), we have $1 + \frac{k}{2} \geq 0$ and $-1 + \frac{k}{2} \leq 0$, from which we conclude that $k \in [-2, 2]$, $n \in \mathbb{R}$. For example, if we take $f(\alpha) = 2$, $\alpha \in [0, 1]$, we obtain one of the infinitely many solutions of the considered FSME:

$$\tilde{X} = \begin{bmatrix} (\alpha, 2-\alpha) & (1+2\alpha, 4-\alpha) \\ (1+\alpha, 3-\alpha) & (\alpha, 2-\alpha) \end{bmatrix}.$$

4. Conclusion

In this paper, we investigated the fuzzy Sylvester matrix equation (FSME) and proposed a new algorithm for determining its general algebraic (strong) solution. The proposed method was based on the $\{1\}$-inverse and employed the Kronecker product to transform the FSME into a dual fuzzy linear system. A necessary and sufficient condition for the $\mathcal{R}$-consistency of the associated system was established. Since every real matrix possesses at least one $\{1\}$-inverse, the proposed approach provides a reliable basis for obtaining all algebraic (strong) solutions of the FSME by means of generalized inverses, without any restrictions related to the nonpositivity (nonnegativity) or the existence of generalized inverses of the coefficient matrices involved.

References

[1] Đ. Dragić, B. Mihailović, Lj. Nedović, "The general algebraic solution of dual fuzzy linear systems and fuzzy Stein matrix equations", *Fuzzy Sets and Systems*, vol. 487, 108997, 2024.

[2] M. Friedman, M. Ming, A. Kandel, "Fuzzy linear systems", *Fuzzy Sets and Systems*, vol. 96, 201-209, 1998.

[3] M. He and H. Jiang and X. Liu, "General strong fuzzy solutions of fuzzy Sylvester matrix equations involving the BT inverse", *Fuzzy Sets and Systems*, vol. 480, 108862, 2024.

[4] H.V. Henderson and S.R. Searle, "The Vec–Permutation Matrix, The Vec Operator and Kronecker Products: A Review", *Linear and Multilinear Algebra*, vol. 9, 271–288, 1981.

[5] B. Mihailović, V. Miler Jerković, B. Malešević, "Solving fuzzy linear systems using a block representation of generalized inverses: The Moore-Penrose inverse", *Fuzzy Sets and Systems*, vol. 353, 44-65, 2018.

[6] D. K. Salkuyeh, "On the solution of the fuzzy Sylvester matrix equation", *Soft Computing*, vol. 22, 6515-6523, 2018.

The 10th Conference on Mathematics in Engineering: Theory and Applications
Novi Sad, December 12-14th 2025

3D TOMOGRAPHY RECONSTRUCTION: FROM THEORY TO APPLICATION IN MEDICAL, INDUSTRIAL AND SCIENTIFIC RESEARCH FIELDS

Lana Dujmović[1], Tibor Lukić[1] and Ana Perišić[1]

https://doi.org/10.24867/META.2025.06 Professional article

Abstract. Three-dimensional tomographic reconstruction enables volumetric analysis of internal structures across medical, biological, industrial, and geophysical applications. Building on the Radon transform, modern 3D tomography incorporates analytical inversion, iterative optimization, and deep-learning methods that address noise, limited-angle data, and low-dose constraints. This paper outlines the mathematical foundations of 3D reconstruction and presents representative applications ranging from micro-CT vasculature imaging and Brownian nanoscale tomography to muon-based inspection of shielded infrastructures. These examples demonstrate how 3D tomography increasingly connects experimental imaging with computational modeling, guiding future techniques toward more accurate and interpretable volumetric reconstruction.

AMS Mathematics Subject Classification (2020): 65D18, 68U10, 00A69

Key words and phrases: 3D tomography, image reconstruction, iterative methods, deep learning, medical imaging

1. Introduction

Tomography refers to the reconstruction of an object's internal structure from its external projections. Its mathematical foundation originates from Radon's 1917 transform, which expresses each projection as a line integral of the unknown object [3]. Early computerized tomography inverted this relation using filtered backprojection (FBP) [3, 5], enabling practical 2D slice reconstruction.

Increasing demands for higher resolution, reduced radiation dose, and improved noise robustness motivated the development of iterative and model-based reconstruction (MBIR), as well as recent deep-learning and diffusion-based approaches [5]. These advances naturally extended to three dimensions, where volumetric imaging integrates multiple projections acquired from a range of orientations.

In this context, 3D tomography provides the mathematical and computational framework for reconstructing full volumetric structure under realistic

[1]Department of Fundamental Sciences, Faculty of Technical Sciences, University of Novi Sad, e-mail: lanad@uns.ac.rs, tibor@uns.ac.rs, anaperisic@uns.ac.rs

acquisition constraints, including limited-angle sampling and noisy measurements.

2. Mathematical Framework for 3D Tomography

Three-dimensional reconstruction methods generalize 2D principles to recover full volumetric geometry. While 2D tomography reconstructs planar slices, 3D approaches integrate multiple 2D projections acquired across different orientations to recover the object's entire internal structure.

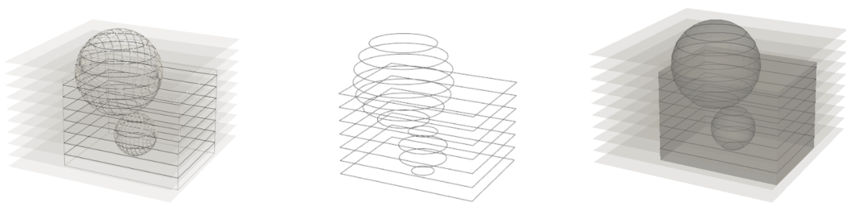

(a) (b) (c)

Figure 1: Illustration of the 3D tomographic reconstruction process.(a) Volumetric object sampled by parallel slice planes.(b) Contour information extracted from each slice. (c) Reconstructed 3D volume obtained by combining all slice measurements.

2.1. From the 2D to the 3D Radon Transform

In 3D tomography, the object is represented by a scalar field $f(x, y, z)$ describing attenuation, density, or another imaging parameter. The 3D Radon transform integrates f over planes orthogonal to a direction $\mathbf{n} = (n_x, n_y, n_z)$ [3]:

$$\mathcal{R}_3 f = \iiint f(x, y, z)\delta(\rho - xn_x - yn_y - zn_z)dxdydz. \tag{2.1}$$

Each projection image recorded on a detector corresponds to sampled values of $\mathcal{R}_3[f]$ after appropriate geometric reparameterization . The inverse 3D Radon transform reconstructs the volume via filtered angular backprojection [3]:

$$f(x, y, z) = -\frac{1}{8\pi^2}\int_{S^2} \frac{\partial^2}{\partial\rho^2}\mathcal{R}_3[f](\rho, \mathbf{n})\bigg|_{\rho = xn_x + yn_y + zn_z} d\mathbf{n}, \tag{2.2}$$

In practice, this inversion is approximated using 3D filtered backprojection, cone-beam variants, or numerical projectors implementing discrete ray-driven or voxel-driven integration [3].

2.2. Discrete Model and Inverse Problem

While the continuous 3D Radon transform describes the forward physics of tomography, practical reconstruction requires a discrete numerical model. The object is sampled into a 3D voxel grid and each detector measurement corresponds to a discretized ray–voxel interaction. This yields the linear forward system

$$b = Ax + \varepsilon, \tag{2.3}$$

where x represents the unknown 3D volume, b the stack of 2D projection images, and A the system matrix that maps rays in 3D space to detector pixels [2, 3]. In three-dimensional tomography, A becomes extremely large and cannot be inverted explicitly, motivating the use of numerical reconstruction techniques.

Iterative algorithms such as ART, SIRT, OSEM, and model-based iterative reconstruction (MBIR) solve the discrete inverse problem by minimizing

$$\min_x \|Ax - b\|^2 + \lambda R(x), \tag{2.4}$$

where $R(x)$ imposes smoothness, sparsity, or structural constraints [2, 3]. These methods are particularly important in 3D, where limited-angle sampling, noise, and low-dose acquisition lead to significant instability in the reconstruction.

Beyond classical smoothness or sparsity priors, geometric constraints play a key role in stabilizing highly underdetermined 3D inverse problems. In limited-view tomography, where large regions of Fourier space remain unsampled, shape-based regularizers help enforce global structural consistency. A notable example is the shape–centroid prior of Lukić and Balázs [7], which restricts feasible binary reconstructions to those preserving a global centroid estimate. This demonstrates how even minimal geometric information can significantly improve stability under extreme projection sparsity.

3. Challenges in Tomographic 3D Reconstruction

Although the mathematical foundations of tomographic imaging are well established, practical 3D reconstruction remains limited by several persistent issues. Sparse or limited-angle acquisition often restricts angular coverage, producing streaking artifacts and loss of detail [2, 3, 5]. Low-dose requirements further elevate noise, necessitating strong regularization or learned priors to preserve image fidelity [2].

Reconstruction accuracy is also hindered by model mismatch in heterogeneous media, where bone, concrete shielding, or fluidic nanoscale environments distort measured signals [4, 6]. In dynamic imaging scenarios, motion introduces additional inconsistency across projections, forcing algorithms to address temporal undersampling through 4D or motion-compensated reconstruction strategies [4, 5]. Finally, the computational demands of large-scale 3D inverse problems remain high, as both iterative and deep-learning-based methods depend on substantial memory and GPU acceleration [2, 3]. Recent research has begun to address these difficulties through hybrid approaches that combine physics-based modeling with data-driven priors, particularly in applications such as LC-TEM nanoscale tomography, low-dose CT, and muon imaging [4, 6].

4. Representative Applications

3D tomography enables structural analysis across scales from nanometers to meters. This section summarizes three compact examples illustrating the diversity of imaging scenarios.

4.1. Pulmonary vascular imaging with µCT

High-resolution micro-computed tomography (μCT) enables non-destructive, isotropic imaging of soft-tissue vasculature. In the developmental study of *Monodelphis domestica*, Ferner [1] reconstructed the 3D pulmonary vascular network by scanning postnatal lung samples in 2D slices and using X-ray absorption contrast to visualize fine vessels without physical sectioning.

From a methodological perspective, μCT provides a full volumetric map of the vascular tree, which can then be segmented to extract branching patterns, vessel diameters, and spatial organization (see Figure 2). The purpose of using tomography in this context is capture intact vascular geometry and quantify developmental remodeling, capabilities that conventional histology cannot provide. Such imaging is essential for studying developmental biology, organ growth, and pathological alterations in microvascular networks.

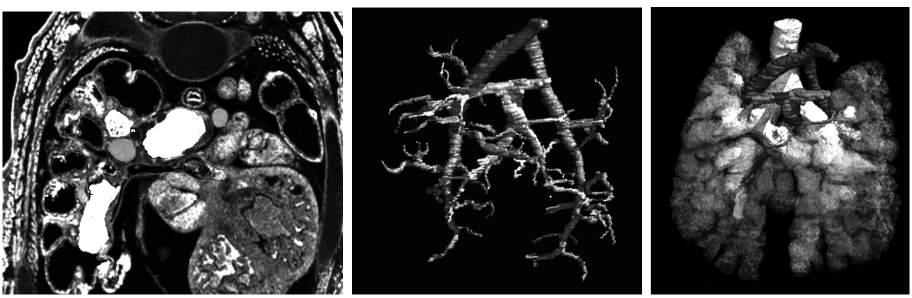

(a) (b) (c)

Figure 2: (a) µCT axial slice. (b) Segmented 3D vasculature. (c) Unsegmented µCT volume. Images adapted from [1].

4.2. Brownian Tomography at the Nanoscale

Kang et al. [4] introduced Brownian tomography, a 4D tomographic framework for reconstructing the shape and motion of single platinum nanocrystals suspended in liquid. In this setting, graphene liquid-cell TEM produces extremely noisy, anisotropic 2D projections of rapidly moving particles, conditions under which classical electron tomography fails because motion and low signal violate the assumption of consistent projection geometry. To address this, the workflow combines fast LC-TEM imaging with a deep neural network that estimates each particle's orientation and 2D contour. These contours act as constraints for voxel carving, yielding coarse 3D volumes that are subsequently refined through temporal shape optimization to ensure smooth frame-to-frame evolution. This enables reconstruction of nanoscale morphological changes (such as rounding, etching, and facet restructuring) during chemical reactions The tomographic approach is crucial because it integrates multiple projections with estimated poses to recover true 3D geometry. without it, only 2D silhouettes would be available, making volumetric and atomic-scale structural evolution impossible to quantify.

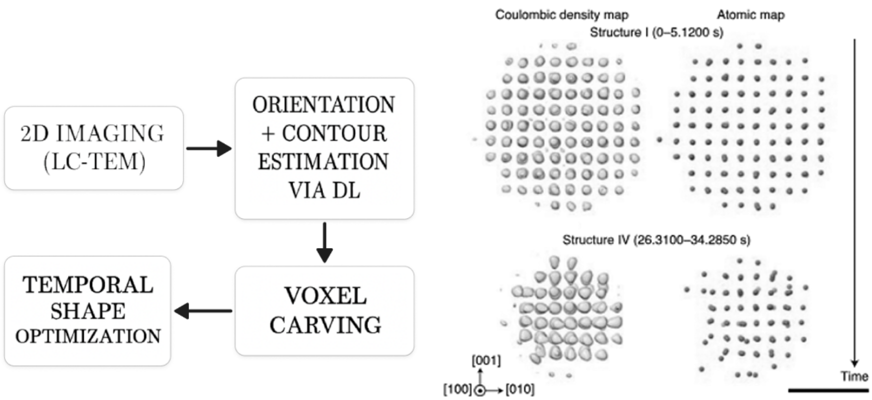

(a) (b)

Figure 3: (a) Brownian tomography workflow: LC-TEM imaging, DL-based pose/contour estimation, voxel carving, and temporal shape optimization. (b) Time-resolved 3D density representations showing nanoscale morphological evolution of a single nanocrystal [4]).

.

4.3. Muon-Based Tomographic Reconstruction of Shielded Infrastructures

Muon tomography exploits naturally occurring cosmic-ray muons, whose high penetration makes them suitable for imaging large, densely shielded structures. In the study by Lefevre et al. [6], trajectories recorded around the G3 reactor at Marcoule were used to reconstruct a 3D density distribution of the reactor core. The technique operates on a principle analogous to X-ray tomography: as muons pass through the reactor, their energy loss reflects the density of the materials along their paths. A SART-based iterative reconstruction method, refined with machine-learning corrections, processes these recorded trajectories to recover the internal density field and reveal structural anomalies within the heavily shielded environment.

This study shows that 3D tomographic principles remain applicable even under extreme physical constraints, large volumes, sparse and anisotropic ray coverage, and strong material attenuation, thereby expanding the domain of tomography to nuclear infrastructure inspection.

Taken together, these examples highlight the growing role of 3D tomographic research as a link between experimental imaging and computational modeling. Continued advances are essential for improving reconstruction reliability, quantitative accuracy, and interpretability across different domains, and for enabling integrative, simulation-driven approaches capable of revealing complex internal structures with high precision.

5. Conclusion

Three-dimensional tomographic reconstruction continues to evolve from classical analytical formulations toward iterative, model-based, and learning-driven methods capable of operating under limited data, noise, and complex physical conditions. While Radon-based operators remain the mathematical foundation, advances in regularization, statistical modeling, and data-driven priors have substantially improved reconstruction fidelity across diverse imaging settings. The applications demonstrate the versatility and expanding reach of 3D tomography across spatial scales and scientific domains. Future progress will depend on integrating physics-based models with simulation-guided and machine-learning approaches, enabling accurate, interpretable, and computationally efficient reconstructions of increasingly complex internal structures.

References

[1] K. Ferner, “Development of the Pulmonary Vasculature in the Gray Short-Tailed Opossum (*Monodelphis domestica*) - 3D Reconstruction by Micro-computed Tomography,” *The Anatomical Record*, vol. 308, pp. 1144–1163, 2024. DOI: 10.1002/ar.25542.

[2] L. L. Geyer, U. J. Schoepf, F. G. Meinel, J. W. Nance, G. Bastarrika, J. A. Leipsic, N. S. Paul, M. Rengo, A. Laghi, and C. N. De Cecco, “State of the Art: Iterative CT Reconstruction Techniques,” *Radiology*, vol. 276, no. 2, pp. 339–357, 2015. DOI: 10.1148/radiol.2015132766.

[3] A. C. Kak and M. Slaney, *Principles of Computerized Tomographic Imaging*. Philadelphia: Society for Industrial and Applied Mathematics (SIAM), 2001. Originally published by IEEE Press, 1988. Available online: `https://doi.org/10.1137/1.9780898719277`.

[4] S. Kang, J. Kim, S. Kim, H. Chun, J. Heo, C. F. Reboul, R. Meana-Pañeda, C. T. S. Van, H. Choi, Y. Lee, J. Rhee, M. Lee, D. Kang, B. H. Kim, T. Hyeon, B. Han, P. Ercius, W. C. Lee, H. Elmlund, and J. Park, “Time-Resolved Brownian Tomography of Single Nanocrystals in Liquid During Oxidative Etching,” *Nature Communications*, vol. 16, 1158, 2025. DOI: 10.1038/s41467-025-56476-8.

[5] S. Kumar, J. Zhang, R. Singh, and A. Verma, “A Methodological Review of 3D Reconstruction Techniques in Tomographic Imaging,” *International Journal of Computer Vision and Imaging Science*, 2024.

[6] B. Lefevre, J. Vogel, H. Gomez, D. Attié, L. Gallego, P. Gonzales, B. Lesage, P. Mas, and D. Pomarède, “3D Reconstruction of a Nuclear Reactor by Muon Tomography: Structure Validation and Anomaly Detection,” *PRX Energy*, vol. 4, 013002, 2025. DOI: 10.1103/PRXEnergy.4.013002.

[7] T. Lukić and P. Balázs, “Limited-View Binary Tomography Reconstruction Assisted by Shape Centroid,” *The Visual Computer*, Springer, 2021. DOI: 10.1007/s00371-021-02258-7.

The 10th Conference on Mathematics in Engineering: Theory and Applications
Novi Sad, December 12-14th 2025

EDUCATIONAL VISUALIZATION OF THE BOIDS ALGORITHM IN UNREAL ENGINE'S NIAGARA SYSTEM[1]

Lana Dujmović[2], Ana Perišić[2] and Nebojsa Ralević[2]

https://doi.org/10.24867/META.2025.07 Professional article

Abstract. Graphical representations of mathematical concepts often tend to appear too abstract and disconnected from intuitive understanding. To bring these principles closer to students, this work explores the simulation of flocking behavior based on the Boids model, implemented through the Niagara Particle System in Unreal Engine. By utilizing procedural functions to define local interaction rules, such as alignment, cohesion, and separation, the study demonstrates how mathematical ideas underlying motion dynamics can be visualized in real time. The research is envisioned as a foundation for future applications within courses such as Simulation in Animation, Engineering Animation and Other Media, and Design of 3D Space and Environments, highlighting the value of visual and interactive approaches in understanding algorithmic and physical systems.

AMS Mathematics Subject Classification (2020): 00A72, 37M05

Key words and phrases: simulation, Unreal Engine, Niagara Particle System, applied mathematics, boids algorithm

1. Introduction

The Boids algorithm (short for "bird-oid objects") represents a groundbreaking concept in computer graphics and Artificial Life. Developed in 1986 by Craig Reynolds, Boids introduced a distributed behavioral model for simulating collective motion observed in flocks of birds, schools of fish, or herds of animals. Its primary goal was to achieve visually convincing and computationally efficient procedural animation, eliminating the need for laborious manual scripting of individual object paths. The significance of the model lies in its demonstration of emergent behavior, complex, synchronized group motion arising solely from simple local interaction rules applied to autonomous agents [1][2]. Modern game engines such as Unreal Engine 5 (UE5) enable

[1]This research is partially supported by the Science Fund of the Republic of Serbia, #GRANT no. 7632, the project "Mathematical Methods in Image Processing under Uncertainty" MaMIPU and by the project "Socio-technological aspects of improving the teaching process in the English language in fundamental disciplines"

[2]Department of Fundamental Sciences, Faculty of Technical Sciences, University of Novi Sad, e-mail: lanad@uns.ac.rs, anaperisic@uns.ac.rs, nralevic@uns.ac.rs

both visual and procedural, implementation of such systems through the Niagara particle framework providing the capability for real-time simulation of complex behaviors within virtual environments This paper explores the implementation of emergent behavior within a modern VFX context by integrating the Boids model and the Niagara particle system in Unreal Engine [5]. Focusing on the visualization of mathematical and procedural principles, it illustrates applied mathematics through creative simulation, with potential uses in games, interactive media, and intelligent animation systems related to courses such as *Simulation in Animation*, *Engineering Animation and Other Media* and *Design of 3D Space and Environments.*

2. Theoretical Framework and current implementations

For further understanding of this paper, it will be necessary to define the problems that will be analysed. A brief overview of all important concepts will be given in this chapter, as well as some of the recent implementations and visualisations.

2.1. Mathematical Model of the Boids System

In his seminal paper "Flocks, Herds, and Schools: A Distributed Behavioral Model" (1987), Craig Reynolds defined three simple behavioral rules that govern how each agent, boid, moves through space. These rules form the foundation of emergent group behavior, showing how coordinated structures arise solely from local interactions, without any central control or global plan [1].

Mathematically, the position and velocity of the i-th boid at time t are represented as:

$$\vec{x}_i(t), \quad \vec{v}_i(t)$$

The evolution of the system is governed by a coupled set of differential equations:

$$\frac{d\vec{x}_i(t)}{dt} = \vec{v}_i(t), \qquad \frac{d\vec{v}_i(t)}{dt} = \mathbf{F}_i^{\text{sep}} + \mathbf{F}_i^{\text{ali}} + \mathbf{F}_i^{\text{coh}} \tag{2.1}$$

where the three components represent local behavioral rules:

Separation (F_i^{sep}) - Each boid tends to avoid getting too close to its neighbors. Reynolds describes this as the avoidance of collisions with nearby flockmates. The rule ensures that individuals maintain a minimal distance, creating a natural spread within the flock and preventing overlaps [2].

Alignment (F_i^{ali}) - A boid aligns its direction and velocity with those of its nearby flockmates (matching velocity with nearby flockmates). This produces synchronized, fluid motion characteristic of real flocks or schools moving cohesively in one direction [2].

Cohesion (F_i^{coh})- Each boid seeks to remain part of the group by moving toward the average position of its neighbors (tendency to move toward the average position of local flockmates). This keeps the flock spatially compact and prevents dispersion [2].

2.2. Implementation using C++ / OpenGL

This is a practical, low-level implementation of the Boids algorithm built with C++, OpenGL, and Dear ImGui, focusing on developing a high-performance and fully controllable flocking simulation from the ground up. The algorithm follows Reynolds's three behavioral rules (alignment, separation, and cohesion) where each agent calculates forces based on its neighbors and updates its position and velocity in every frame (Figure 1). The simulation integrates these rules through a weighted system of parameters (for example, α, β, γ coefficients), enabling interactive adjustment of flock dynamics in real time [3].

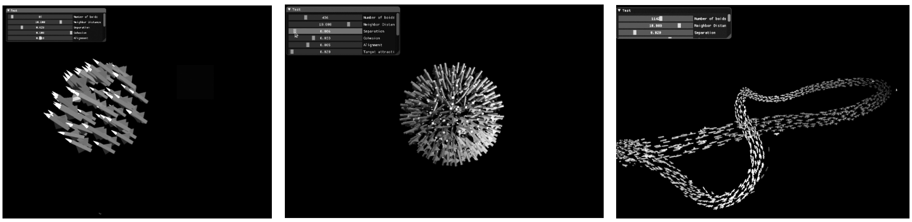

(a) (b) (c)

Figure 1: Visualization of Boids in OpenGL: (a) initialization, (b) flock formation, (c) emergent flow [3].

While the system produces smooth and realistic flocking behavior, boids are rendered as simple geometric shapes. It also requires solid programming skills in C++ and a basic understanding of the graphics pipeline. This makes the implementation useful for demonstrating the mathematical and computational principles behind emergent behavior and serves as a reference for higher-level frameworks like Unreal Engine's Niagara system, where similar concepts can be applied without low-level coding.

2.3. Implementation in Unity

In "Simulation of Boid Type Behaviours in Unity Environment" (2021), the authors implemented Reynolds's three behavioral rules, separation, alignment, and cohesion, directly within Unity's 3D environment using C# scripting and the built-in physics system [4]. Each boid was represented as a lightweight particle or simple 3D object that continuously updated its position and velocity based on nearby agents detected within a fixed perception radius (Figure 2). This neighborhood detection was optimized using Unity's spatial query functions to ensure real-time performance even for larger swarms. The visualization made use of Unity's Scene View and Game View for simultaneous inspection of both algorithmic behavior and rendered motion. The authors noted that the emergent flocking patterns, turning, grouping, and smooth avoidance, were "visually convincing and stable across various population densities."

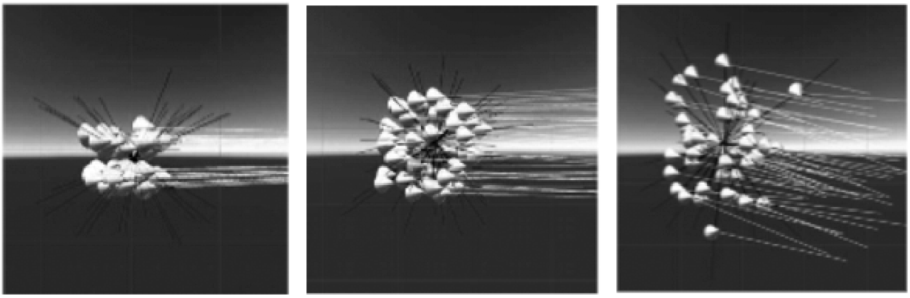

(a) (b) (c)

Figure 2: Visualization of a BOID group in the Unity environment. The Reynolds forces (separation, alignment, and cohesion) were parameterized through a frequency coefficient. Subfigures (a), (b), and (c) illustrate the resulting variations in behavior as this coefficient is adjusted [4].

While the presented models are relatively simple and computationally efficient, it remains an open question how the same system would perform with complex, animated meshes, where per-agent updates could significantly increase processing cost.

3. Applications in UE 5.6

This chapter presents the visualization and simulation of the Boids algorithm, specifically the flocking behavior of birds and fish, developed in Unreal Engine 5.6 using the Niagara particle system (see Figures 3 and 4).

While the Unity implementation relied on object-based simulation, the Niagara framework treats each boid as an individual particle instance governed by user-defined behavior modules. These modules are constructed through node-based scripts, allowing procedural control of particle position, velocity, and interaction directly within the editor's visual environment. Each particle operates as an autonomous agent that continuously evaluates its surroundings according to Reynolds's three behavioral rules: separation, alignment, and cohesion. The system utilizes GPU-accelerated rendering, which supports higher population counts and smoother real-time performance compared to CPU-based approaches, offering an efficient platform for studying emergent motion.

3.1. Mathematical Vector-Based Forces in Niagara

In Unreal Engine's Niagara system, particle motion is defined through vector-based mathematical functions acting in three-dimensional space. These functions modify particle position and velocity via transformations that reflect physical or behavioral principles such as turbulence, drag, attraction, and rotation. Each force represents a vector field $\vec{F}(\vec{r},t)$ influencing motion according to

$$\frac{d\vec{v}}{dt} = \frac{\vec{F}(\vec{r},t)}{m}. \tag{3.1}$$

By combining several operators, Niagara reproduces complex emergent behaviors from simple local interactions, aligning with Reynolds's flocking dynamics model.

(a) (b) (c)

Figure 3: Visualization of bird flocking behaviour (a) initialization, (b) flock formation, (c) emergent flow.

The *Curl Noise Force* adds spatially coherent turbulence by applying the curl of a 3D noise field. *Drag* simulates viscous damping proportional to velocity, ensuring smooth motion. *Point Attraction Force* drives particles toward a target, modeling cohesion or goal-seeking behavior. *Add Velocity* integrates multiple computed influences into a single motion update. *Vortex Force* induces rotational flow around an axis, and *Point Force* generalizes attraction and repulsion for obstacle avoidance or spatial structuring [5].

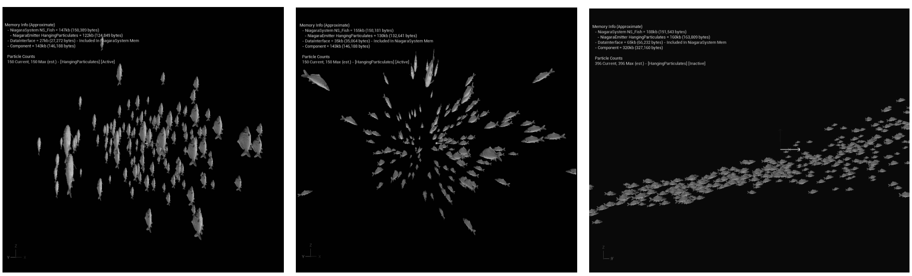

(a) (b) (c)

Figure 4: Visualization of fish shoaling behaviour (a) initialization, (b) shoaling formation, (c) emergent flow.

Together, these modules illustrate how Niagara's procedural system transforms mathematical vector operations into visually coherent simulations of collective motion, merging physics-based modeling with real-time graphics.

3.2. Discussion and observation

Compared to object-oriented implementations in Unity and low-level C++/OpenGL simulations, Niagara provides a higher degree of procedural flexibility and visual realism. The node-based system abstracts the underlying mathematics while maintaining control over physical accuracy, enabling rapid experimentation with large agent populations. Its GPU-driven architecture supports complex emergent behavior without significant performance loss, demonstrating how mathematical concepts can be effectively visualized through modern VFX workflows. Future applications may extend toward interactive scenarios, such as Blueprint-driven character responses or virtual crowd visualization, where behavioral rules can dynamically adapt through fuzzy or AI-based control schemes [2].

4. Conclusion

Overall, the Niagara implementation confirms that Unreal Engine 5 provides a robust foundation for real-time visualization of emergent systems, bridging scientific simulation with cinematic-quality rendering. The resulting workflow illustrates how behavioral algorithms such as Boids can evolve from purely computational experiments into expressive, interactive, and visually rich simulations. The research is expected to support future work in courses such as Simulation in Animation, Engineering Animation and Other Media, and Design of 3D Space and Environments, by providing a framework for demonstrating motion simulations through the Niagara particle system. This system relies on vector algebra, local-space transformations, and particle lifecycle management, offering students a more intuitive and visual approach to understanding algorithmic and physical motion.

References

[1] C. W. Reynolds, "Flocks, herds, and schools: A distributed behavioral model," *Computer Graphics (SIGGRAPH '87 Conference Proceedings)*, vol. 21, no. 4, pp. 25–34, 1987.

[2] I. L. Bajec, M. Mraz, and N. Zimic, "The computational beauty of flocking: Boids revisited," *Mathematical and Computer Modelling of Dynamical Systems*, vol. 13, no. 4, pp. 331–347, Aug. 2007.

[3] M. Grinberg, "Mastering Flock Simulation with Boids, C++, OpenGL, and ImGui," *Better Programming*, Medium, 2020. Available at: https://medium.com/better-programming/mastering-flock-simulation-with-boids-c-opengl-and-imgui-5a3ddd9cb958.

[4] T. Lypovyi and J. Montusiewicz, "Simulation of Boid Type Behaviours in Unity Environment," *International Journal of Computer Science and Engineering*, vol. 9, pp. 1–10, 2021.

[5] Epic Games, "Getting Started in Niagara Effects for Unreal Engine," *Unreal Engine Documentation*, Epic Games, 2024. Available at: `https://dev.epicgames.com/documentation/en-us/unreal-engine/getting-started-in-niagara-effects-for-unreal-engine`.

The 10th Conference on Mathematics in Engineering: Theory and Applications
Novi Sad, December 12-14th 2025

SHAPE CONVEXITY DESCRIPTORS: A COMPARATIVE STUDY

Vladimir Ilić [1] and Jelena Ivetić [2]

https://doi.org/10.24867/META.2025.08 Original research article

Abstract. This paper presents a comparative study of shape convexity descriptors with a particular focus on a newly proposed measure based on the first Hu moment invariant. While conventional convexity measures such as area- and perimeter-based ratios offer intuitive interpretations, they lack full invariance under geometric transformations. We propose a novel convexity measure which leverages the relation between the first Hu moment invariant and the integral of squared distances over shape regions. This measure is shown to be invariant under translation, rotation, and scaling, and satisfies all essential properties expected from a convexity descriptor. Experimental results on a variety of planar shapes confirm its discriminative power and robustness, particularly in scenarios involving non-convex and multi-component shapes.

AMS Mathematics Subject Classification (2020): 68U10

Key words and phrases: Shape analysis, convexity measure, Hu moment invariant, moment-based descriptors

1. Introduction

Convexity is one of the fundamental geometric properties of planar shapes, closely related to structural integrity, boundary regularity, and spatial compactness. Quantitative convexity descriptors aim to numerically express how much a shape deviates from being convex. These descriptors play a central role in digital shape analysis, with wide applications across multiple scientific and engineering disciplines.

In engineering, convexity measures are used in automated quality control and defect detection on manufactured parts, where deviation from convexity often signals damage or misalignment. In precision agriculture, shape convexity helps in plant species recognition, leaf disease detection, and crop phenotyping using drone or satellite imagery. In medical imaging, convexity descriptors assist in segmentation and classification tasks—particularly for detecting tumors, lesions, or anatomical irregularities where shape deformities provide diagnostic cues.

[1]Department of Fundamental Sciences, Faculty of Technical Sciences, University of Novi Sad, e-mail: vlada.mzsvi@uns.ac.rs

[2]Department of Fundamental Sciences, Faculty of Technical Sciences, University of Novi Sad, e-mail: jelenaivetic@uns.ac.rs

While many convexity measures have been proposed—most notably area- and perimeter-based ones — these are often sensitive to non-similarity transformations or limited in their ability to capture subtle shape deviations. Moment-based descriptors, on the other hand, offer strong mathematical foundations and allow for invariance under translation, rotation, and scaling. In this work, we build upon a recent interpretation of the first Hu moment invariant and derive a new convexity descriptor denoted as $\mathcal{C}^{Hu}(S)$. This measure is theoretically sound and practically robust, especially when dealing with non-convex and multi-component shapes.

The paper is structured as follows: in Section 2, we recall the necessary mathematical preliminaries. Section 3 introduces the $\mathcal{C}^{Hu}(S)$ measure and analyzes its theoretical properties. Section 4 presents comparative experimental results with classical convexity descriptors.

2. Preliminaries

We begin by listing basic definitions to support understanding of the main results and to establish assumptions ensuring theoretical correctness.

A shape, as a fundamental object property similar to color or texture, is typically represented as a bounded (not necessarily connected) region in the plane, defined by foreground pixels in a binary image. For a planar shape S, the *moment of order* $p+q$, denoted as $m_{p,q}(S)$, is defined as:

$$m_{p,q}(S) = \iint\limits_{S} x^p y^q dxdy. \tag{2.1}$$

The zero-order moment $m_{0,0}(S)$ gives the area of the shape, while $\left(\frac{m_{1,0}(S)}{m_{0,0}(S)}, \frac{m_{0,1}(S)}{m_{0,0}(S)}\right)$ determines its centroid. Since translation does not affect the shape, *central moments*, denoted by $\overline{m}_{p,q}(S)$, are introduced:

$$\overline{m}_{p,q}(S) = \iint\limits_{(x,y)\in S} (x - x_c(S))^p\,(y - y_c(S))^q\,dx\,dy. \tag{2.2}$$

However, central moments are not invariant to scaling. To achieve scale invariance, we define the *normalized central moments* as:

$$\mu_{p,q}(S) = \frac{1}{m_{0,0}(S)^{(p+q+2)/2}} \cdot \overline{m}_{p,q}(S). \tag{2.3}$$

Achieving rotational invariance is more challenging. In his seminal work [3], Hu introduced a set of seven algebraic moment invariants with respect to rotation. This paper focuses on the first Hu invariant, which involves only second-order shape moments:

$$\mathcal{H}u(S) = \mu_{2,0}(S) + \mu_{0,2}(S) = \frac{1}{m_{0,0}(S)^2} \cdot \left(\overline{m}_{2,0}(S) + \overline{m}_{0,2}(S)\right). \tag{2.4}$$

Note that all Hu invariants are also geometric moment invariants, as they can be derived from geometric primitives [4]. This enables their use as shape descriptors in image processing and computer vision.

We will evaluate the behavior of our proposed convexity measure against two common alternatives: $\mathcal{C}^{Area}(S)$ and $\mathcal{C}^{Per}(S)$ [1], defined as:

$$\mathcal{C}^{Area}(S) = \frac{Area(S)}{Area(S^{ch})}, \qquad \mathcal{C}^{Per}(S) = \frac{Perimeter(S^{ch})}{Perimeter(S)}, \tag{2.5}$$

where S^{ch} denotes the convex hull of the shape S.

3. Convexity measure based on the first Hu moment invariant

In this section, we present the new measure of shape convexity originally defined in [5] and which is based on a new interpretation of the first Hu moment invariant, introduced in [2], which serves as the base for deriving a new shape measure. Following by this result, we started from the quantity $\mathcal{I}_{SD}(S)$, representing the integral of the square of the distance between all pairs of points of the shape S, defined as follows (for the full derivation, see [5]):

$$\begin{aligned} \mathcal{I}_{SD}(S) &= \frac{1}{2} \cdot \iint\limits_{(x,y)\in S} \iint\limits_{(z,t)\in S} \left((x-z)^2 + (y-t)^2\right) dx\,dy\,dz\,dt \\ &= m_{0,0}(S) \cdot (\overline{m}_{2,0}(S) + \overline{m}_{0,2}(S)). \end{aligned} \tag{3.1}$$

Now, based on (2.4) and (3.1) it follows that

$$\frac{1}{m_{0,0}(S)^3} \cdot \mathcal{I}_{SD}(S) \;=\; \frac{1}{m_{0,0}(S)^2} \cdot (\overline{m}_{2,0}(S) + \overline{m}_{0,2}(S)) \;=\; \mathcal{H}u(S). \tag{3.2}$$

This result, originally introduced in [2], implies that the first Hu moment invariant can be expressed by means of the integral of the squared distance between all pairs of points belonging to the shape normalized by the the area of the shape itself. Given the quantity $\mathcal{I}_{SD}(S)$ can be expressed in terms of the area and the first Hu moment invariant related to the shape considered, it is invariant to translation and rotation. Based on this, if the same reasoning is applied to the convex hull of S, denoted with S^{ch}, the following holds:

$$\begin{aligned} \mathcal{I}_{SD}(S^{ch}) &= \frac{1}{2} \cdot \iint\limits_{(x,y)\in S^{ch}} \iint\limits_{(z,t)\in S^{ch}} \left((x-z)^2 + (y-t)^2\right) dx\,dy\,dz\,dt \\ &\geq \frac{1}{2} \cdot \iint\limits_{(x,y)\in S} \iint\limits_{(z,t)\in S} \left((x-z)^2 + (y-t)^2\right) dx\,dy\,dz\,dt \;=\; \mathcal{I}_{SD}(S). \end{aligned} \tag{3.3}$$

The latter represents a key result that provides the foundation for deriving in [5] a new shape measure evaluating the degree to which a given shape is convex. In this context, we present the following lemma, whose results are a direct consequence of the last inequality in (3.3).

Lemma 3.1. *For an arbitrary shape S, the following statements hold:*

(a) $0 < \dfrac{\mathcal{I}_{SD}(S)}{\mathcal{I}_{SD}(S^{ch})} \leq 1$*;*

(b) $\mathcal{I}_{SD}(S) \ = \ \mathcal{I}_{SD}(S^{ch}) \ \Leftrightarrow \ \ S \equiv S^{ch}$*.*

Based on the results in Lemma 3.1, we can conclude that the observed ratio can be used in a certain way to characterize how much the shape S deviates from its convex hull, i.e., how convex it is. Accordingly, we have the following definition.

Definition 3.2. Given a shape S, the *shape convexity measure* $\mathcal{C}^{Hu}(S)$ is defined as

$$\mathcal{C}^{Hu}(S) \ = \ \frac{\mathcal{I}_{SD}(S)}{\mathcal{I}_{SD}(S^{ch})} \ = \ \frac{m_{0,0}(S)^3 \cdot \mathcal{H}u(S)}{m_{0,0}(S^{ch})^3 \cdot \mathcal{H}u(S^{ch})}. \tag{3.4}$$

Such a defined convexity measure $\mathcal{C}^{Hu}(S)$ also satisfies all the basic properties that any well-defined convexity measure should satisfy. Some of these properties are given in the following theorem, which we state here without proof. For more details about $\mathcal{C}^{Hu}(S)$ and its properties, the reader is referred to the paper [5] where the measure $\mathcal{C}^{Hu}(S)$ itself was originally designed.

Theorem 3.3. *For the convexity measure* $\mathcal{C}^{Hu}(S)$ *the following holds:*

(a) $\mathcal{C}^{Hu}(S) \in (0, 1]$, for all shapes S*;*

(b) $\mathcal{C}^{Hu}(S) = 1 \ \Leftrightarrow \ S$ is a convex shape;

(c) $\mathcal{C}^{Hu}(S)$ *is invariant under similarity transformations (i.e., translation, rotation and scaling);*

(d) the lower bound 0 *for* $\mathcal{C}^{Hu}(S)$ *is the best possible, i.e., for each* $\epsilon > 0$ *there exists a shape* S *such that* $0 < \mathcal{C}^{Hu}(S) < \epsilon$*.*

4. Experimental illustration of the convexity measures

In this section, we present several illustrative experiments to compare the behavior of the shape convexity measure $\mathcal{C}^{Hu}(S)$ with two commonly used convexity measures: $\mathcal{C}^{Area}(S)$ and $\mathcal{C}^{Per}(S)$ [1]. The performance of these measures is illustrated on synthetically generated shapes, with modifications including the size and relative position of the holes within the shape.

The first experiment illustrates the behavior of the three convexity measures with respect to the relative position of the indentation within the shape, without changing its size (shape examples are shown in Figure 1, (a)–(c)). As observed from the first plot in Figure 2, the area and perimeter of both the shape and its convex hull remain unchanged, causing $\mathcal{C}^{Area}(S)$ and $\mathcal{C}^{Per}(S)$ to be insensitive to the indentation's position. This can be considered a weakness compared to $\mathcal{C}^{Hu}(S)$, which is able to distinguish between the given shapes. Notably, the measured $\mathcal{C}^{Hu}(S)$ value is invariant with respect to the symmetrical placement of the indentation. This behavior aligns with the theoretical results established in the previous section, confirming that the proposed measure is invariant under shape similarity transformations (the examined shape pairs are rotation-invariant around the vertical axis of symmetry).

In the second experiment, we examine how the convexity measures respond when the width of the indentation increases (Figure 1, (d)–(f)). As expected, the convexity decreases, which is reflected in both $\mathcal{C}^{Hu}(S)$ and $\mathcal{C}^{Area}(S)$ (see the central plot in Figure 2). In contrast, the perimeter-based measure $\mathcal{C}^{Per}(S)$ remains unchanged, indicating its insensitivity to such deformation. This is consistent with its definition: increasing the indentation width does not alter the perimeters of the shape or its convex hull, while the area of the shape decreases relative to the unchanged convex hull area.

In the final experiment, we consider the case where the side length of the square hole within the shape increases (Figure 1, (g)–(i)). As anticipated, the convexity decreases, which is captured by all three measures (see the third plot in Figure 2). This behavior is in full accordance with their definitions: a larger internal hole leads to a greater deviation between the shape and its convex hull.

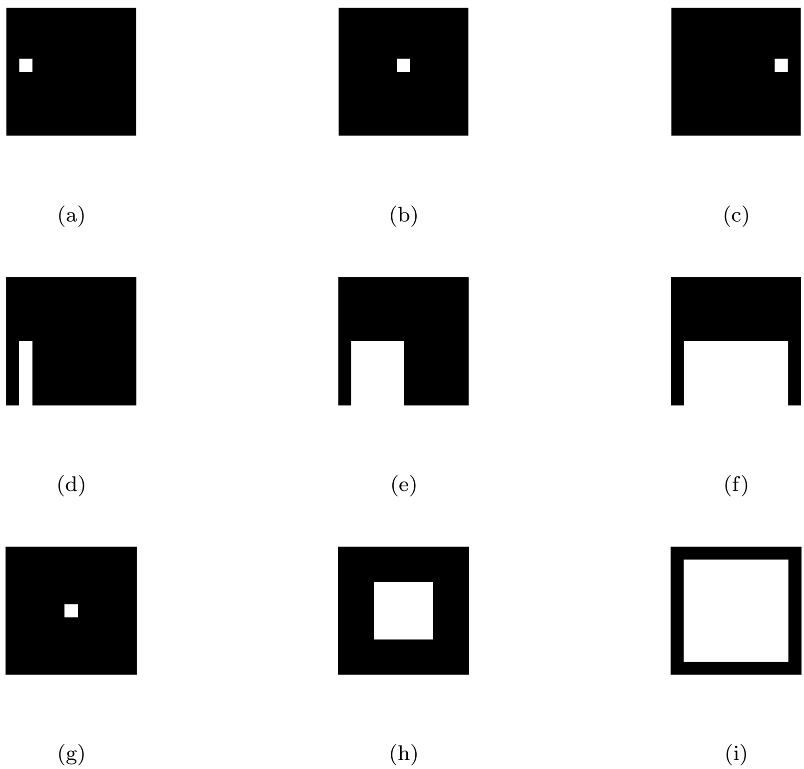

Figure 1: Shapes obtained from the squares for different hole positions (first row), indentation width (second row) and size of the holes (third row).

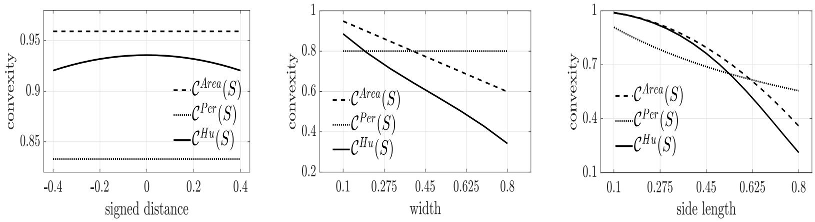

Figure 2: Plots of computed $\mathcal{C}^{Hu}(S), \mathcal{C}^{Area}(S)$ and $\mathcal{C}^{Per}(S)$ values with respect to hole position, indentation width, and hole size within the shape.

Acknowledgement

This research was supported by the Department of Fundamental Disciplines in Engineering through the project entitled "Socio-technological aspects of improving the teaching process in the English language in fundamental disciplines".

References

[1] M. Sonka, V. Hlavac, R. Boyle, "Image Processing, Analysis, and Machine Vision", 3rd Edition, Thomson Learning 2008.

[2] J. Žunić, P. L. Rosin, V. Ilić, "Disconnectedness: A new moment invariant for multi-component shapes", Pattern Recognition, vol. 78, pp. 91–102, 2018.

[3] M. K. Hu, "Visual pattern recognition by moment invariants", IRE Transactions on Information Theory, vol. 8 (2), pp. 179–187, 1962.

[4] D. Xu, H. Li, "Geometric moment invariants", Pattern Recognition, vol. 41 (1), pp. 240–249, 2008.

[5] V. Ilić, J.Ivetić, "Shape convexity based on the first Hu moment invariant", Submitted, 2025.

The 10th Conference on Mathematics in Engineering: Theory and Applications
Novi Sad, December 12-14th 2025

SECOND-ORDER MOMENT INVARIANTS WITH APPLICATIONS IN IMAGE ANALYSIS

Vladimir Ilić [1] and Júlia Kiš [2]

https://doi.org/10.24867/META.2025.09 Review Article

Abstract. In this paper, we consider three well-known second-order moment invariants, such as the first two Hu moment invariants and the first affine moment invariant. These invariants are not computationally demanding, they are simple, and easy to understand. Their dependencies and shape interpretation are also included in the paper, along with an experimental illustration of their behavior on synthetically generated shapes.

AMS Mathematics Subject Classification (2020): 68U10

Key words and phrases: Shape, Moment invariants, Shape descriptors, Image understanding

1. Introduction

Shape, as a fundamental object property akin to color and texture, is traditionally identified as a bounded, not necessarily connected region in the plane, represented by foreground pixels in a binary digital image. For the planar shape S, the *moment of order* $p+q$, denoted as $m_{p,q}(S)$, is defined as follows

$$m_{p,q}(S) = \iint_S x^p y^q dx\, dy. \tag{1.1}$$

The zero-order moment $m_{0,0}(S)$ represents the area of the shape, while $\left(\frac{m_{1,0}(S)}{m_{0,0}(S)}, \frac{m_{0,1}(S)}{m_{0,0}(S)}\right)$ represents its centroid. Since the shape remains unchanged during translation of the object itself, central moments, denoted by $\overline{m}_{p,q}(S)$, are introduced as follows:

$$\overline{m}_{p,q}(S) = \iint_{(x,y)\in S} (x - x_c(S))^p\, (y - y_c(S))^q\, dx\, dy \tag{1.2}$$

and as such they are translation invariant. However, given that the shape of the object does not change under translation for an arbitrary vector, without

[1]Department of Fundamental Sciences, Faculty of Technical Sciences, University of Novi Sad, e-mail: vlada.mzsvi@uns.ac.rs
[2]Faculty of Technical Sciences, University of Novi Sad, e-mail: kiss.zs.julia@gmail.com

loss of generality, we can suppose that the shape considered is translated so that its centroid coincides with the origin. In this regard, if we assume that

$$m_{1,0}(S) = 0 \text{ and } m_{0,1}(S) = 0, \tag{1.3}$$

then $\overline{m}_{p,q}(S) = m_{p,q}(S)$. Given that a shape of the object does not change under the translation transformation, this assumption is not a restriction in the shape based object analysis tasks.

Additionally, in the design tasks of shape-based object analysis tools, the requirement of invariance with respect to object scaling is particularly important, since the shape of the object does not change under such transformations. Therefore, it is useful to define an appropriate moment invariant, denoted e.g. $\mu_{p,q}(S)$, such that for an arbitrary shape S and a scaling factor $\lambda > 0$ the following equality holds:

$$\mu_{p,q}(\lambda \odot S) \;=\; \mu_{p,q}(S) \tag{1.4}$$

where $\lambda \odot S = \{(\lambda \cdot x, \lambda \cdot y) \Big| (x, y) \in S\}$ denotes shape S scaled by factor $\lambda > 0$.

To design such a moment-based shape feature, notice that

$$\begin{aligned} m_{p,q}(\lambda \odot S) \;&=\; \iint\limits_{\lambda \odot S} (\lambda \cdot x)^p (\lambda \cdot y)^q d(\lambda \cdot x)\, d(\lambda \cdot x) \\ &=\; \lambda^{p+q+2} \cdot \iint\limits_{S} x^p y^q dx\, dy = \lambda^{p+q+2} \cdot m_{p,q}(S), \end{aligned} \tag{1.5}$$

while in the case $p = q = 0$, we get that $m_{0,0}(\lambda \odot S) = \lambda^2 \cdot m_{0,0}(S)$, respectively $\lambda = \left(\frac{m_{0,0}(\lambda \odot S)}{m_{0,0}(S)}\right)^{1/2}$. Hence, after substituting the last relation in (1.5), we obtain the following:

$$m_{p,q}(\lambda \odot S) \;=\; \left(\frac{m_{0,0}(\lambda \odot S)}{m_{0,0}(S)}\right)^{(p+q+2)/2} \cdot m_{p,q}(S) \tag{1.6}$$

i.e.,

$$\frac{m_{p,q}(\lambda \odot S)}{m_{0,0}(\lambda \odot S)^{(p+q+2)/2}} \;=\; \frac{m_{p,q}(S)}{m_{0,0}(S)^{(p+q+2)/2}} \tag{1.7}$$

Now from the latter we get that the normalized moments are defined as

$$\mu_{p,q}(S) = \frac{m_{p,q}(S)}{m_{0,0}(S)^{(p+q+2)/2}}$$

and they are invariant w.r.t. translation and scaling of the shape. Since the shape of the object does not change when scaled by an arbitrary factor, in the rest of the paper we assume that all considered shapes have unit area, i.e. $m_{0,0}(S) = 1$. Therefore, we have that $\mu_{p,q}(S) = m_{p,q}(S)$, which does not diminish the generality of the presented results.

2. Main results

For the results presented in this paper, the first two Hu moment invariants derived from second-order moments are of particular importance. From a mathematical point of view, the moment invariant $I(m_{p,q})$ refers to a moment function of $m_{p,q}$ that does not change its value under various transformations, e.g. similarity or affine ones, i.e., that satisfies the condition $I(m_{p,q}(S)) = I(m_{p,q}(T[S]))$ where $T[S]$ denotes the transformed shape of S itself. These quantities represent the two best-known and most widely used moment invariants among all seven presented in [1]. The latter follows from their low computational complexity, since only second-order moments are needed for their calculation. Thus, for a given shape S of a unit area, centered at the origin, the first two Hu moment invariants are defined as follows:

$$\mathcal{H}_1(S) = \mu_{2,0}(S) + \mu_{0,2}(S), \tag{2.1}$$

$$\mathcal{H}_2(S) = \left(\mu_{2,0}(S) - \mu_{0,2}(S)\right)^2 + 4\mu_{1,1}(S)^2. \tag{2.2}$$

In addition, we will also mention here the first affine moment invariant [2], which is defined using second-order moments as follows:

$$\mathcal{A}_1(S) \quad = \quad \mu_{2,0}(S) \cdot \mu_{0,2}(S) - \mu_{1,1}(S)^2. \tag{2.3}$$

Using elementary calculation, it is easy to verify that the first affine moment invariant in (2.3) can be expressed as a combination of the first two Hu moment invariants in (2.1) and (2.2), i.e. the following holds:

$$\begin{aligned}
\mathcal{H}_1(S)^2 - \mathcal{H}_2(S) \ &= \left(\mu_{2,0}(S) + \mu_{0,2}(S)\right)^2 - \left(\left(\mu_{2,0}(S) - \mu_{0,2}(S)\right)^2 + 4\mu_{1,1}(S)^2\right) \\
&= \mu_{2,0}(S)^2 + 2 \cdot \mu_{2,0}(S) \cdot \mu_{0,2}(S) + \mu_{0,2}(S)^2 \\
&\quad - \left(\mu_{2,0}(S)^2 - 2 \cdot \mu_{2,0}(S) \cdot \mu_{0,2}(S) + \mu_{0,2}(S)^2 + 4\mu_{1,1}(S)^2\right) \\
&= 4 \cdot \left(\mu_{2,0}(S) \cdot \mu_{0,2}(S) - \mu_{1,1}(S)^2\right) = 4 \cdot \mathcal{A}_1(S).
\end{aligned}$$

It is worth noting that all three considered second-order moment invariants are also geometric moment invariants, since they can be derived using the corresponding geometric invariants [3]. Based on this, $\mathcal{H}_1(S)$ can be expressed as the integral of the square of the distance of all points $A(x, y)$ inside the shape S (of unit area) from its centroid (i.e., origin) $O(0, 0)$:

$$\boxed{\iint\limits_{A(x,y)\in S} \left|\overrightarrow{r_A}\right|^2 dx\, dy} = \iint\limits_{(x,y)\in S} (x^2 + y^2)\, dx\, dy = \boxed{\mathcal{H}_1(S)}$$

where, for simplicity, the position vector of point A is denoted by $\overrightarrow{r_A}$. Regarding $\mathcal{H}_2(S)$ and $\mathcal{A}_1(S)$, they can be expressed as a multiple integral of the corresponding geometric invariants, e.g. $\Phi(\overrightarrow{r_A}, \overrightarrow{r_B})$, for all pairs of points $A(x, y)$ and $B(u, v)$ varying through S. Thus, for $\mathcal{H}_2(S)$, resp. $\mathcal{A}_1(S)$, the geometric invariant $\Phi(\overrightarrow{r_A}, \overrightarrow{r_B})$ has the form $\Phi(\overrightarrow{r_A}, \overrightarrow{r_B}) = \left|\overrightarrow{r_A}\right|^2 \cdot \left|\overrightarrow{r_B}\right|^2 \cdot \cos 2\angle(\overrightarrow{r_A}, \overrightarrow{r_B})$, resp. $\Phi(\overrightarrow{r_A}, \overrightarrow{r_B}) = 2 \cdot \left(\frac{1}{2} \cdot \left|\overrightarrow{r_A} \times \overrightarrow{r_B}\right|\right)^2$. Now the equality of the considered second-order moment invariants and the multiple integrals of the corresponding invariants can be easily shown using elementary calculus as follows:

$$\boxed{\iint\limits_{A(x,y)\in S}\iint\limits_{B(u,v)\in S} \left|\overrightarrow{r_A}\right|^2 \cdot \left|\overrightarrow{r_B}\right|^2 \cdot \cos 2\angle(\overrightarrow{r_A},\overrightarrow{r_B})\, dx\, dy\, du\, dv}$$

$$= \iint\limits_{(x,y)\in S}\iint\limits_{(u,v)\in S} (x^2+y^2)\cdot(u^2+v^2)\cdot\cos 2\varphi\, dx\, dy\, du\, dv \ (\text{for } \varphi = \angle(\overrightarrow{r_A},\overrightarrow{r_B}))$$

$$= \iint\limits_{(x,y)\in S}\iint\limits_{(u,v)\in S} (x^2+y^2)\cdot(u^2+v^2)\cdot\left(2\cos^2\varphi - 1\right)\, dx\, dy\, du\, dv$$

$$= \iint\limits_{(x,y)\in S}\iint\limits_{(u,v)\in S} 2\cdot(x^2+y^2)\cdot(u^2+v^2)\cdot\cos^2\varphi\, dx\, dy\, du\, dv$$

$$- \iint\limits_{(x,y)\in S}\iint\limits_{(u,v)\in S} (x^2+y^2)\cdot(u^2+v^2)\, dx\, dy\, du\, dv$$

$$= \iint\limits_{(x,y)\in S}\iint\limits_{(u,v)\in S} 2\cdot\left(\sqrt{x^2+y^2}\cdot\sqrt{u^2+v^2}\cdot\cos\varphi\right)^2\, dx\, dy\, du\, dv$$

$$- \iint\limits_{(x,y)\in S}\iint\limits_{(u,v)\in S} (x^2u^2+x^2v^2+y^2u^2+y^2v^2)\, dx\, dy\, du\, dv$$

$$= \iint\limits_{(x,y)\in S}\iint\limits_{(u,v)\in S} 2\cdot((x,y)\circ(u,v))^2\, dx\, dy\, du\, dv \ (\circ \text{ denotes the dot product})$$

$$- \iint\limits_{(x,y)\in S}\iint\limits_{(u,v)\in S} (x^2u^2+x^2v^2+y^2u^2+y^2v^2)\, dx\, dy\, du\, dv$$

$$= \iint\limits_{(x,y)\in S}\iint\limits_{(u,v)\in S} \left(2\cdot(xu+yv)^2 - (x^2u^2+x^2v^2+y^2u^2+y^2v^2)\right)\, dx\, dy\, du\, dv$$

$$= \iint\limits_{(x,y)\in S}\iint\limits_{(u,v)\in S} \left(x^2u^2 - x^2v^2 - y^2u^2 + y^2v^2 + 4\cdot xyuv\right)\, dx\, dy\, du\, dv$$

$$= \mu_{2,0}(S)^2 - 2\cdot\mu_{2,0}(S)\cdot\mu_{0,2}(S) + \mu_{0,2}(S)^2 + 4\cdot\mu_{1,1}(S)^2$$

$$= \left(\mu_{2,0}(S) - \mu_{0,2}(S)\right)^2 + 4\cdot m\mu_{1,1}(S)^2 = \boxed{\mathcal{H}_2(S)}$$

where the moments $\mu_{p,q}(S)$ comes from the equality

$$\iint\limits_{(x,y)\in S}\iint\limits_{(u,v)\in S} x^p y^q u^r v^s\, dx\, dy\, du\, dv$$

$$= \iint\limits_{(x,y)\in S} x^p y^q\, dx\, dy \cdot \iint\limits_{(u,v)\in S} u^r v^s\, du\, dv = \mu_{p,q}(S)\cdot\mu_{r,s}(S), \tag{2.4}$$

while for the first affine moment invariant the following applies:

$$\boxed{\iint\limits_{A(x,y)\in S}\ \iint\limits_{B(u,v)\in S} 2\cdot\left(\frac{1}{2}\cdot\left|\overrightarrow{r_A}\times\overrightarrow{r_B}\right|\right)^2\, dx\,dy\,du\,dv}$$
$$= 2\cdot\iint\limits_{(x,y)\in S}\iint\limits_{(u,v)\in S}\frac{1}{4}\cdot(x\cdot v-y\cdot u)^2\, dx\,dy\,du\,dv$$
$$= \frac{1}{2}\cdot\iint\limits_{(x,y)\in S}\iint\limits_{(u,v)\in S}\left(x^2\cdot v^2-2\cdot x\cdot y\cdot u\cdot v+y^2\cdot u^2\right)\, dx\,dy\,du\,dv$$
$$= \frac{1}{2}\cdot\left(\mu_{2,0}(S)\cdot\mu_{0,2}(S)-2\cdot\mu_{1,1}(S)^2+\mu_{2,0}(S)\cdot\mu_{0,2}(S)\right)$$
$$= \mu_{2,0}(S)\cdot\mu_{0,2}(S)-\mu_{1,1}(S)^2=\boxed{\mathcal{A}_1(S)}.$$

Such a geometric interpretation of the moment invariant paved the way for the definition of diverse shape-based object descriptors whose behavior can be relatively easily understood and predicted in some applications, even before a specific shape-based object analysis task is performed [4, 5].

3. Experimental illustration of the behavior of the second-order moment invariants

Here we present experimental results related to three second-order moment invariants, i.e. $\mathcal{H}_1(S), \mathcal{H}_2(S)$ and $\mathcal{A}_1(S)$, applied to synthetically generated rectangular shapes centered at the origin and of unit area, i.e., $R(t) = \{(x,y)\big| x\in[-\frac{t}{2},\frac{t}{2}], y\in[-\frac{1}{2t},\frac{1}{2t}]\}$, defined for $t>0$. Therefore, for the second-order shape moments, the following applies:

$$\mu_{1,1}(R(t)) = \int\limits_{-\frac{t}{2}}^{\frac{t}{2}}\int\limits_{-\frac{1}{2t}}^{\frac{1}{2t}} xy\,dx\,dy = \int\limits_{-\frac{t}{2}}^{\frac{t}{2}} x\,dx\cdot\int\limits_{-\frac{1}{2t}}^{\frac{1}{2t}} y\,dy = 0$$

$$\mu_{2,0}(R(t)) = \int\limits_{-\frac{t}{2}}^{\frac{t}{2}}\int\limits_{-\frac{1}{2t}}^{\frac{1}{2t}} x^2\,dx\,dy = \int\limits_{-\frac{t}{2}}^{\frac{t}{2}} x^2\,dx\cdot\int\limits_{-\frac{1}{2t}}^{\frac{1}{2t}} dy = 2\cdot\frac{x^3}{3}\Big|_0^{\frac{t}{2}}\cdot 2\cdot y\Big|_0^{\frac{1}{2t}}$$
$$= \frac{\cancel{2}}{3}\cdot\frac{\cancel{t^3}\ t^2}{\cancel{8}\ 4}\cdot\cancel{2}\cdot\frac{1}{\cancel{2}\cancel{t}} = \frac{t^2}{12}$$

$$\mu_{0,2}(R(t)) = \int\limits_{-\frac{t}{2}}^{\frac{t}{2}}\int\limits_{-\frac{1}{2t}}^{\frac{1}{2t}} y^2\,dx\,dy = \int\limits_{-\frac{t}{2}}^{\frac{t}{2}} dx\cdot\int\limits_{-\frac{1}{2t}}^{\frac{1}{2t}} y^2\,dy = 2\cdot x\Big|_0^{\frac{t}{2}}\cdot 2\cdot\frac{y^3}{3}\Big|_0^{\frac{1}{2t}}$$
$$= \cancel{2}\cdot\frac{\cancel{t}}{\cancel{2}}\cdot\frac{\cancel{2}}{3}\cdot\frac{1}{\cancel{8}\ 4\ \cancel{t^3}\ t^2} = \frac{1}{12t^2}$$

while for the second-order moment invariants we get the following results:

$$\mathcal{H}_1(R(t)) = \mu_{2,0}(R(t)) + \mu_{0,2}(S) = \frac{t^2}{12} + \frac{1}{12t^2} = \frac{t^4+1}{12t^2}$$
$$\mathcal{H}_2(R(t)) = (\mu_{2,0}(R(t)) - \mu_{0,2}(R(t)))^2 + 4\mu_{1,1}(R(t))^2$$
$$= \left(\frac{t^2}{12} - \frac{1}{12t^2}\right)^2 = \left(\frac{t^4-1}{12t^2}\right)^2$$
$$\mathcal{A}_1(R(t)) = \mu_{2,0}(R(t)) \cdot \mu_{0,2}(R(t)) - \mu_{1,1}(R(t))^2 = \frac{t^2}{12} \cdot \frac{1}{12t^2} = \frac{1}{144}$$

Notice that for $t = 1$, the rectangle $R(t)$ becomes a unit square, centered at the origin, with second-order moment invariants given as follows:

$$\mathcal{H}_1(R(t=1)) = \frac{1}{6}, \quad \mathcal{H}_2(R(t=1)) = 0, \quad \mathcal{A}_1(R(t=1)) = \frac{1}{144}.$$

On the other hand, in the case when $t \to \infty$, the rectangle $R(t)$ degenerates into an infinitely long horizontal strip, giving $\lim_{t\to\infty} \mu_{2,0}(R(t)) = \infty$ and $\lim_{t\to\infty} \mu_{0,2}(R(t)) = 0$, i.e. $\lim_{t\to\infty} \mathcal{H}_1(R(t)) = \infty$ and $\lim_{t\to\infty} \mathcal{H}_2(R(t)) = \infty$. Conversely, in the case when $t \to 0$, $R(t)$ becomes an infinitely long vertical strip with $\mu_{2,0}(R(t)) \to 0$ and $\mu_{0,2}(R(t)) \to \infty$, while both $\mathcal{H}_1(R(t))$ and $\mathcal{H}_2(R(t))$ remain infinite.

Interestingly, in all cases for arbitrary values of t the first affine moment invariant $\mathcal{A}_1(R(t))$ does not change, i.e. it is invariant during modification of a horizontally oriented rectangle via a square to a vertically oriented rectangle and vice versa. The latter follows from the fact that the square and the rectangle are affine-invariant shapes shapes (obtained by scaling by different factors along different axes), so the value of $\mathcal{A}_1(R(t))$ remains unchanged as expected (equal to $\frac{1}{144}$ in this case). In contrast, the values of the Hu moment invariants change as expected, given the observed modification of the rectangle is not a similarity transformation.

References

[1] M. K. Hu, "Visual pattern recognition by moment invariants", IRE Transactions on Information Theory, vol. 8 (2), pp. 179–187, 1962.

[2] J. Flusser, T. Suk, "Pattern Recognition by Affine Moment Invariants", Pattern Recognition, vol. 26 (1), pp. 167–174, 1993.

[3] D. Xu, H. Li, "Geometric moment invariants", Pattern Recognition, vol. 41 (1), pp. 240–249, 2008.

[4] V. Ilić, N. Ralević, "Hexagonality as a New Shape-Based Descriptor of Object", Journal of Mathematical Imaging and Vision, vol. 62, pp. 1136–1158, 2020.

[5] J. Žunić, D. Žunić, "Shape interpretation of second-order moment invariants", Journal of Mathematical Imaging and Vision, vol. 56(1), pp. 125–136, 2016.

The 10th Conference on Mathematics in Engineering: Theory and Applications
Novi Sad, December 12-14th 2025

FUZZY MODEL FOR NOISE REMOVAL IN MONTE CARLO RENDERING BASED ON AGGREGATION FUNCTION[1]

Julijana Kilibarda [2] and Nebojša Ralević [3]

https://doi.org/10.24867/META.2025.10 Article type

Abstract. Monte Carlo rendering represents a modern and highly precise technique for simulating light behavior in three-dimensional scenes, enabling a high level of photorealism. However, a limited number of samples per pixel often leads to the occurrence of pronounced statistical noise, which significantly affects the quality and usability of rendered images. To address this issue, this paper proposes a fuzzy model for noise removal in Monte Carlo rendering, based on aggregation functions (and an adaptive window size during the filtering process). The model applies fuzzy principles to determine the degree of similarity between neighboring pixels and dynamically adjusts the filter parameters according to the local image structure. This ensures efficient noise reduction while preserving important visual details and avoiding artifacts. Experimental results indicate that the proposed approach provides a better trade-off between image quality and computational complexity compared to standard filtering methods.

AMS Mathematics Subject Classification (2020): 68U10, 94A08

Key words and phrases: Monte Carlo rendering, fuzzy filter, aggregation functions, adaptive processing, noise removal, visual quality

1. Introduction

Denoising digital images is one of the basic problems in image processing and computer visualization. The quality of the image affects the reliability of the analysis and the visual experience, so the development of effective filtering methods is of great importance. In computer graphics, Monte Carlo rendering generates stochastically noise due to random sampling of light paths, which appears as low-intensity variational noise ("grain noise") and occasional extreme outliers ("fireflies"). These phenomena degrade visual quality and increase rendering time by requiring a larger number of samples per pixel. This work builds on a previously developed fuzzy model for removing impulse noise

[1]

[2] Artificial Intelligence & Information Technology, Banja Luka and Department of Fundamental Sciences, Faculty of Technical Sciences, University of Novi Sad, e-mail: julijanakapor142@gmail.com

[3] Department of Fundamental Sciences, Faculty of Technical Sciences, University of Novi Sad, e-mail: nralevic@uns.ac.rs

using the *AWAM* (Adaptive Weighted Aggregation Mean) filter [3], which combines noise detection and adaptive filtering with dynamic window expansion. In this research the model is extended to Monte Carlo noise through introduction of statistical detection based on local mean and standard deviation, as well as special processing of extremely bright pixels ("fireflies"). The proposed fuzzy-*AWAM* approach introduces a combined spatial photometric weighted aggregation mechanism that enables efficient noise removal while preserving image structure and realistic light transitions. Experiments show that the model gives more stable and natural results in comparison with standard filtering methods [1] and provides a basis for further development of advanced fuzzy algorithms in rendering.

2. Monte Carlo rendering

Monte Carlo rendering is a method for creating realistic images by simulating the movement of light through a scene using random sampling. It is employed because an analytical solution to the integrals that describe light material interactions is often infeasible, especially in complex scenes with reflections, refractions, and volumetric effects [2]. The goal is to calculate the average contribution of a large number of light paths for each pixel.

The main challenge of Monte Carlo rendering is the high estimation variance, which manifests as random ("grain") noise pixels may appear slightly brighter or darker than the true value. Noise is particularly pronounced when the number of samples per pixel is low, which is common in practice due to limited computational resources and rendering time.

To reduce variance, techniques such as importance sampling, stratified sampling, and adaptive sampling are applied, but these methods do not eliminate noise completely. Therefore, post-filtering (denoising) is used to remove the remaining variations by exploiting information from neighboring pixels or additional geometric and lighting data.

Approaches to noise reduction are generally divided into methods that improve sampling during rendering and those applied as post-processing on the final image. In recent years, deep-learning-based models have become dominant; however, they require large training data sets, substantial computational resources, and often exhibit limited generalization and detail preservation.

For these reasons, this paper considers a statistical and fuzzy approach to Monte Carlo denoising, similar to the method presented in [5], where the distribution of samples for each pixel is analyzed and relevant neighbors are selected for filtering. Fuzzy logic, unlike classical filters with sharp thresholds, uses degrees of membership that enable adaptive decision-making regarding the contribution of each pixel. This allows better preservation of edges and fine details, does not require pretrained models, and can be directly applied to rendered images resulting in flexible and efficient noise removal suitable for production-level rendering.

3. Image filtering - algorithm

The proposed model is based on the principles of fuzzy aggregation and adaptive weighted filtering in the spatial-photometric domain. The algorithm consists of two basic phases: noise detection and a filtering phase incorporating a dynamic window expansion mechanism that enables stable estimation even in areas of high lighting variance. Unlike the impulse noise treated in the previous work, this study considers variational Monte Carlo noise and extreme light values ("fireflies"), which require a statistical detection approach.

3.1. Noise detection phase

For each image point $A(i,j)$, a local window $W_{i,j}$ of size $m \times m$ is defined. Within this window, the local arithmetic mean and standard deviation are computed:

$$\mu_{i,j} = \frac{1}{|W_{i,j}|} \sum_{(p,q)\in W_{i,j}} A(p,q), \quad \sigma_{i,j} = \sqrt{\frac{1}{|W_{i,j}|} \sum_{(p,q)\in W_{i,j}} (A(p,q) - \mu_{i,j})^2}.$$

Based on these values, the deviation of the pixel from the local average is computed:

$$d(i,j) = |A(i,j) - \mu_{i,j}|.$$

A pixel is marked as "noisy" if the deviation exceeds the threshold proportional to the local variance:

$$b(i,j) = \begin{cases} 255, & d(i,j) > T \cdot \sigma_{i,j} \\ 0, & \text{otherwise} \end{cases}.$$

The parameter T represents the detection threshold, which is experimentally determined sets in the range $T \in [1.5, 3.0]$. In this way, a binary noise mask $b(i,j)$ is formed, where a value of 255 denotes noise and 0 denotes a "clean" pixel. To identify rare extreme values ("fireflies"), a more robust criterion based on the local median $M_{i,j}$ is used:

$$b_f(i,j) = \begin{cases} 255, & A(i,j) > M_{i,j} + K\sigma_{i,j} \\ 0, & \text{otherwise} \end{cases},$$

where K is a constant that determines the threshold for identification outliers (most often $K \in [4, 8]$). Pixels detected as fireflies are corrected in a preprocessing step by replacing them with the local median, preventing extreme values from negatively affecting the filtering phase.

3.2. Filtering phase

For each pixel marked as noisy, a set of clean neighboring pixels is determined as $S_{i,j} = \{A(p,q)|b(p,q) = 0\}$ (b is the binary noise mask) within the window $W_{i,j}$. If the number of clean pixels in the current window is insufficient ($|S_{i,j}| < n$), the window is dynamically expanded $W_{i,j}^{(m)} \to W_{i,j}^{(m+2)}$ (index m

- indicates the size of the window in pixels, is changing) until the condition $|S_{i,j}| \geq n)$ is met or until the maximum size m_{max} is reached.

Let the pixel values in the set $S_{i,j}$ be denoted by p_k, and their distances from the center by d_k. Spatial weights and photometric weights are defined as follows:

$$\alpha_k = \frac{1}{\beta^{d_k}}, \quad s_k = \exp(-\frac{|p_k - A(i,j)|}{\sigma_I}),$$

where $\beta > 1$ is a parameter that controls the weight decay with distance, and σ_I is the coefficient controlling sensitivity to intensity differences.

The combined weight for each neighbor is:

$$w_k = \frac{\alpha_k \cdot s_k}{\sum_r \alpha_r s_r}.$$

The reconstruction of the damaged pixel is performed using the weighted power-root mean (WAM):

$$\hat{A}(i,j) = (\sum_k w_k p_k^{\kappa})^{1/\kappa}.$$

where the parameter κ enables interpolation between different types of means:
$\kappa = 1$: arithmetic mean,
$\kappa \to 0$: approximately the geometric mean,
$\kappa > 1$ more weight to larger values.

This defines the $AWAM$ fuzzy aggregation operator adapted to Monte Carlo noise.

3.3. Final reconstruction

After filtering all detected pixels, the resulting image $\hat{A}$ represents the denoised estimate of the original image. To evaluate the performance of the model, the following metric functions are used:

$$MAE = \frac{1}{N}\sum|A - \hat{A}|, \quad PSNR = 10\log_{10}\frac{255^2}{MSE},$$

where $MSE = \frac{1}{N}\sum(A - \hat{A})^2$.

4. Experimental setup and evaluation

A custom $3D$ scene was used to evaluate the proposed fuzzy model. The scene was rendered in the Autodesk 3ds Max environment using the V-Ray renderer. The image was generated in multiple variants with different numbers of samples per pixel (spp): 2, 4, 8, 16, and 32 spp. The reference image was obtained by rendering at 128 spp, which provides a visually and numerically stable ground truth.

The developed algorithm was then applied to the rendered images. The results obtained using the proposed method were compared with standard filters commonly used in practice: Median, Gaussian, Bilateral, and Non-Local

Means (NLM). The comparison was performed using two error metrics MAE and $PSNR$ computed relative to the reference render.

The obtained results show that the proposed $AWAM$ model significantly outperforms all benchmark methods across all noise levels. $AWAM$ achieves the lowest MAE values (often 36 times lower than those of the other filters) and the highest $PSNR$ values, with improvements of up to $+7$ dB in favor of the proposed method. These findings indicate that the fuzzy $AWAM$ approach better corresponds to the statistical nature of Monte Carlo noise and enables more stable and precise image reconstruction compared to classical filtering techniques.

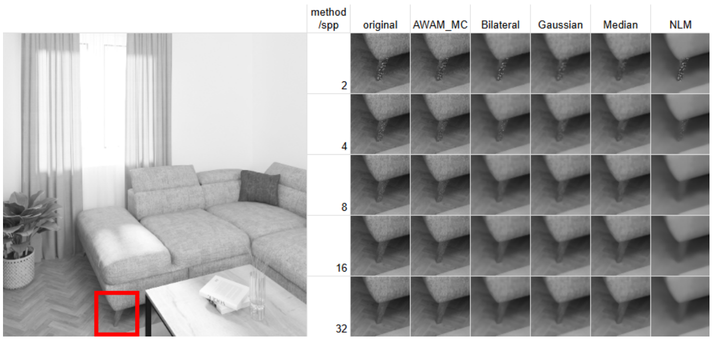

Figure 1: Comparative visualization of Monte Carlo noise filtering results on a local image segment. Rendered versions with different spp values and the filtering outputs of the $AWAM\_MC$ method and standard filters are shown. The $AWAM\_MC$ method produces the most visually faithful results.

Acknowledgement

This research is partially supported by the Science Fund of the Republic of Serbia, #GRANT no. 7632, the project "Mathematical Methods in Image Processing under Uncertainty" MaMIPU.

References

[1] C. R. Gonzalez and E. R. Woods, *Digital Image Processing*, 3rd ed., Pearson Education Inc., 2008.

[2] M. Pharr, W. Jakob and G. Humphreys, *Physically based rendering: From theory to implementation*, Morgan Kaufmann is an imprint of Elsevier 50 Hampshire Street, 5th Floor, Cambridge, MA 02139, USA, 2017

[3] N. M. Ralević and J. Kapor, "Filter za uklanjanje šuma na digitalnoj slici zasnovan na agregacionim funkcijama", *9th Conference on Mathematics in Engineering: Theory and Applications, Conference proceedings, META 2024*, pp. 138-143, May 31-June 2, 2024, Novi Sad, Serbia

[4] N. M. Ralević, D. Karaklić and N. Pištinjat, "Fuzzy metric and its applications in removing the image noise", *Soft Computing*, Vol. 23, Issue 22, pp. 12049-12061, 2019.

[5] H. Sakai, C. Freude, T. Auzinger, D. Hahn, and Michael Wimmer, "A Statistical Approach to Monte Carlo Denoising", *In SIGGRAPH Asia 2024 Conference Papers (SA Conference Papers '24)*, 11 pages, December 03-06, 2024, Tokyo, Japan. ACM, New York, NY, USA, 2024.

The 10th Conference on Mathematics in Engineering: Theory and Applications
Novi Sad, December 12-14th 2025

LEARNING MATHEMATICS THROUGH AN EDUCATIONAL ROLE-PLAYING VIDEO GAME[1]

Mikloš Kovač [2], Goran Radojev [3] and Mirjana Brdar [4]

https://doi.org/10.24867/META.2025.11 professional article

Abstract. This paper presents an educational adventure role-playing video game designed to support learning of mathematics, focusing on linear equations and systems of linear equations. The game integrates curricular content into an interactive environment where students solve problems as part of the storyline. By providing immediate feedback, autonomy, and opportunities for active learning, it promotes critical thinking, problem-solving, and engagement.

AMS Mathematics Subject Classification (2020): 97B50, 97U50

Key words and phrases: Educational video games, mathematics learning, linear equations.

1. Introduction

Humans are inherently creative and social, capable of shaping their environment while exploring rich inner worlds of imagination. Traditional art forms, such as literature, music, and painting, have long provided means to experience alternative realities. In the contemporary era, video games have emerged as a digital bridge between imagination and reality, offering immersive worlds where players can experiment, solve problems, and engage in complex narratives [4]. They foster cognitive, social, and emotional skills, including decision-making, problem-solving, communication, and adaptability, while providing safe spaces for exploration and failure [1, 2].

In education, video games offer dynamic and interactive environments that support active learning, personalized pacing, and the development of critical thinking and computational skills [5, 7]. By combining engaging narratives with problem-solving, games can complement traditional instruction and facilitate the practice of curriculum content in motivating ways.

[1]This research has been supported by the Ministry of Science, Technological Development and Innovation of the Republic of Serbia under grants No. 451-03-137/2025-03/200134 (Mirjana Brdar); 451-03-137/2025-03/200125 and 451-03-136/2025-03/200125 (Goran Radojev).

[2]Electrotechnical School “Mihajlo Pupin”, Novi Sad, Serbia, e-mail: kovac.miklos@gmail.com

[3]Department of Mathematics and Informatics,, Faculty of Science, University of Novi Sad, Serbia, e-mail: radojev@dmi.uns.ac.rs

[4]Faculty of Technology Novi Sad, University of Novi Sad, Serbia, e-mail: mirjana.brdar@uns.ac.rs

Building on these principles, we developed "Secrets of Algebria", an educational role-playing game (RPG) designed to integrate mathematics learning with adventure gameplay. The game focuses on linear equations with one variable and systems of linear equations with two variables, embedding curricular tasks within a rich narrative and interactive mechanics. Players solve problems through story-driven challenges, supported by a mind map technique that visually organizes steps, concepts, and relationships, helping students structure reasoning and understand solution processes.

This study presents the design and features of the game, highlighting how educational content, RPG elements, and interactive tools can be combined to create a motivating and effective environment for mathematics practice. The game demonstrates the potential of educational video games as a complementary tool for enhancing learning outcomes and developing 21st-century competencies in students.

2. Main results

Video games serve as an exceptionally effective medium for promoting self-directed learning among players—and, by extension, among students in informal learning contexts—owing to their distinctive attributes. They create a safe and engaging environment where experimentation and failure carry no real-world consequences, while simultaneously granting learners a high level of autonomy. These characteristics enable students to advance at their own pace and receive immediate, continuous feedback within the game setting, fostering the development of a wide range of cognitive and metacognitive competencies [6].

Figure 1: Theodora's shop in Tangent Valley

Building on these principles, the video game "Secrets of Algebria" was created as an innovative and, thus far, unique digital environment for mathematics learning and knowledge acquisition. Conceived as a complementary didactic resource to be used in parallel with regular classroom instruction, the game runs on Windows-based computers and enables students to engage in independent exploration and practice of mathematical topics. Its content focuses on linear equations with one unknown and systems of linear equations with two unknowns. While fundamental concepts are introduced during standard lessons, practice activities are delivered through the game, serving as an interactive extension of homework. Additionally, a built-in theoretical module supports students who may have missed classes, allowing them to study the material independently.

The technical part of educational RPG video game was developed between May 2024 and February 2025 by Mikloš Kovač using the RPG Maker MV software. Throughout this period, a fully functional game was created, incorporating all the typical features of the RPG genre while embedding mathematics curriculum content. The game falls within the RPG (role-playing game) genre, specifically of the adventure type, and features turn-based combat mechanics. Set in a richly designed fantasy world, it incorporates all the characteristic elements of a traditional RPG experience. Players control a team of four characters—a warrior, an arcanist, a mage, and a cleric—who progress through successive levels by earning experience points, enhancing their attributes according to class roles, and acquiring new weapons, armor, and spells. The combat system emphasizes logical reasoning and strategic planning, while the option to save progress promotes continuity and regular engagement. Additionally, each save records the total time the student has spent playing.

To fulfill its educational goals, the game introduces an imaginative setting known as Algebria. The central narrative revolves around a young sorceress—exceptionally talented yet deeply averse to mathematics—who, in an act of defiance, attempts to imprison and erase mathematics from the world. Although her plan is only partially successful, she manages to seal a fragment of mathematics' very essence within a magical medallion, disrupting the balance of the realm. In response, four heroes—metaphorical representations of typical students with limited mathematical confidence and motivation—set out on a journey to retrieve the medallion and restore harmony to Algebria.

The storyline unfolds in Tangent Valley (Figure 1), a village that serves as the game's main hub and visual centerpiece. Within this setting, players can explore several themed locations, including the tavern The Playful Logarithm, the shop At the Obtuse Angle, the school The Merry Integral—where students can review or catch up on missed lessons—and the Mathematics Gym, designed to assist players in problem solving through the use of mind maps.

Mathematical challenges are seamlessly integrated into the game's narrative. Each time a player encounters a treasure chest containing rewards such as experience points, items, or equipment, they must solve a word problem to unlock it. Correct solutions grant access to the reward, while skipping the task reduces the amount of experience points and resources obtained. To assist students in solving these problems, the game incorporates a mind map technique (Figure 2), which visually organizes the steps, relevant concepts, and relationships between elements of the problem. This approach helps learners structure their reasoning, understand the solution process, and make connections across different mathematical ideas. In certain sections, mandatory tasks

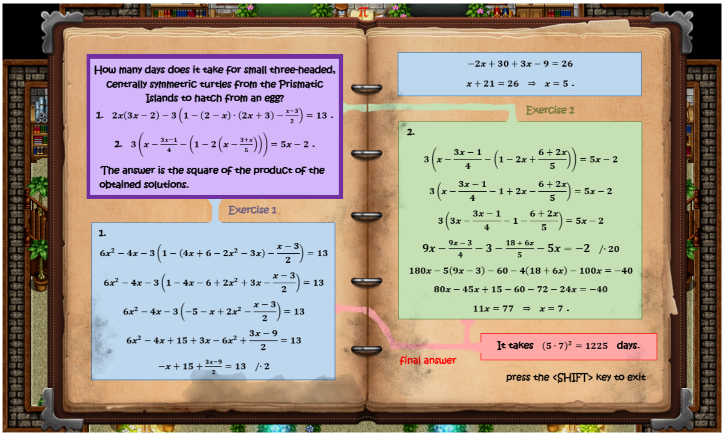

Figure 2: An example of a task solution using the mind map technique

are presented—two standard mathematical problems accompanied by short, humorous instructions—which must be solved and combined to progress further. By combining interactive gameplay with visual problem-solving support, the game effectively balances entertainment with curriculum-aligned practice.

Mathematical challenges are intricately embedded into the game's narrative structure. Whenever a player discovers a treasure chest containing rewards such as experience points, items, or equipment, they are prompted to solve a word problem in order to unlock it. Providing the correct solution grants access to the reward, whereas skipping the task reduces the amount of earned experience and available resources. In this way, the game effectively merges its entertainment components with systematic practice of mathematics aligned with the school curriculum.

Figure 3: Layout of the menu with equipment and basic characteristics of the hero

The distinctive advantage of this approach lies in its capacity to reveal different levels of student engagement—specifically, whether learners limit themselves to the mandatory tasks necessary for game progression or take additional initiative by completing optional challenges. While the game can indeed be finished without solving optional problems—since experience points, equipment, and treasures are also gained through required tasks—students who choose to skip them forfeit part of the overall experience points and valuable rewards that facilitate advancement.

In addition, the game includes a variety of NPCs (non-player characters) who enrich the narrative world through humorous dialogues and mathematically themed riddles. Every conversation and task bears a clear mathematical reference. Items collected throughout the game—such as armor (Robe of Hypothesis, Armor of Determinants), weapons (Sum of Fate, Dance of Variables, Revenge of the Right Triangle, Song of Fractions, Function of Forgetting, Perimeter of the Full Moon, Radius of Dawn), jewelry (Power of Algorithms, Trigonometric Thought, Arithmetic Whisper), and consumables (Linear Owl's Egg)—are all named after mathematical concepts (Figure 3). The heroes' spells and special abilities likewise carry symbolic mathematical names, including Spark of Equivalence, Flame of Logic, Irrational Strike, Ballad of Theorems, Blade of the Golden Ratio, and Mirror of Symmetry, thereby reinforcing the game's immersive mathematical atmosphere.

3. Conclusion

In this study, we presented the educational RPG Secrets of Algebria, a unique game designed to integrate mathematics learning with engaging role-playing elements. By combining curriculum-based tasks on linear equations with adventure gameplay, the game allows students to practice mathematics in an interactive, motivating environment. Its design supports independent learning, problem-solving, and student engagement, while maintaining a balance between education and entertainment. This game demonstrates the potential of digital tools to complement traditional mathematics instruction, offering an innovative approach that connects abstract concepts with immersive, hands-on experiences.

This RPG video game now needs to be tested among high school students. It is necessary to determine how much time students will spend on average playing the game, as well as how many tasks they will complete on average. After that, it should be examined whether students who use the game achieve better results in the subject area covered by the game compared to students who learned in the traditional way, using an experimental and a control group. It is also extremely important to determine to what extent such games should be included in teaching, especially considering that among high school students there is a large number of individuals who are addicted to video games [3].

References

[1] M. Barr, "Video games can develop graduate skills in higher education students: a randomised trial", *Computers & Education*, vol. 113, pp. 86–

97, 2017.

[2] D. Bavelier, C. S. Green, A. Pouget, and P. Schrater, "Brain plasticity through the life span: learning to learn and action video games", *Annual Review of Neuroscience*, vol. 35, pp. 391–416, 2012.

[3] H. Choujaa, S. Zoukal, M. Agoub, "Internet and video game addiction among adolescents: A preliminary study", *L'Encephale, 2025*, https://doi.org/10.1016/j.encep.2024.11.012.

[4] I. Granic, A. Lobel, and R. C. M. E. Engels, "The benefits of playing video games", *American Psychologist*, vol. 69(1), pp. 66–78, 2014.

[5] R. E. Mayer, "Computer games in education", *Annual Review of Psychology*, vol. 70(1), pp. 531–549, 2019.

[6] W. Toh and D. Kirschner, "Self-directed learning in video games, affordances and pedagogical implications for teaching and learning", *Computers & Education*, vol. 154(5), art. 103912, 2020.

[7] W. Zhao and V. J. Shute, "Can playing a video game foster computational thinking skills?", *Computers & Education*, vol. 141(3), art. 103633, 2019.

The 10th Conference on Mathematics in Engineering: Theory and Applications
Novi Sad, December 12-14th 2025

MATHEMATICAL MODELS IN VINE DISEASE DETECTION

Levente Tamás, [1] Tibor Lukić [2] and Stefan Gubo [3]

https://doi.org/10.24867/META.2025.12 Review article

Abstract. This paper presents a short description of an automated proximal aerial image-based vine disease detection approach, developed specifically for the region of the Carpathian Basin. Particular focus is given to the description of the applied Convolutional Neural Network architecture. Several experimental results are shown comparing results obtained from data collected in different geographical regions.

AMS Mathematics Subject Classification (2020): 68U10, 42B10

Key words and phrases: Vine Disease Detection, Convolution, Drone Imaging, Convolutional Neural Networks.

1. Introduction

Precision viticulture has evolved into a multidisciplinary research area where autonomous robots, multisensory perception, and deep learning are central to real-time plant health monitoring. Efficient vineyard management requires early detection of foliar diseases, accurate canopy segmentation, and robust cross-regional generalization. The reviewed works [1, 2, 3] collectively demonstrate how UAV-based remote sensing and ground-level proximal imaging contribute to building adaptable vision systems for viticulture.

A recurring challenge is the spatial and temporal variability of vineyards: grape cultivars, canopy morphology, disease expression, and illumination conditions vary across regions. The three studies address these challenges through multi-domain datasets, convolutional neural network (CNN) architectures, and domain transfer techniques.

1.1. Geographically Distributed Vine Disease Detection

The work in [1] examines disease detection in vineyards of the Carpathian Basin using low-altitude UAV platforms equipped with RGB cameras. The study emphasises the need for regional transfer learning because visual disease symptoms differ across cultivars and climatic zones. The authors constructed a large dataset exceeding 10,000 annotated images and employed YOLOv7 with COCO pretrained weights to detect diseased leaf regions.

[1]Automation Department, Technical University of Cluj-Napoca, Romania, e-mail: Levente.Tamas@aut.utcluj.ro

[2]Department of Fundamental Sciences, Faculty of Technical Sciences, University of Novi Sad, Serbia, e-mail: tibor@uns.ac.rs

[3]Faculty of Economics and Informatics, J. Selye University, Komárno, Slovakia, e-mail: gubos@ujs.sk

1.2. Segmentation of Diseased Leaf Regions

The authors of the paper [2] study segmentation methods for detecting the affected areas on individual vine leaves. The authors compare five techniques: Otsu thresholding, SegNet, Mask R-CNN, Feature Pyramid Networks, and MobileNetV3. Their dataset includes laboratory images (PlantVillage) and in-field leaf crops collected from multiple locations.

1.3. Proximal Canopy Segmentation Using FPN

The work [3] presents an FPN-based approach for proximal canopy segmentation using drone and ground-robot imagery. Unlike leaf-level segmentation, canopy segmentation must account for heterogeneous foliage, occlusions, and mixed backgrounds.

2. Mathematical background and CNN architectures of the methods

The automatic detection of vine leaf diseases in aerial close-range images relies heavily on mathematical models rooted in modern computer vision and deep learning. At the core of these models lie convolutional operators, which act as learnable filters capable of extracting hierarchical image features. A convolutional operator computes a weighted sum between a small kernel and localized image regions, enabling the detection of fundamental structures such as edges, color transitions, and texture variations. When stacked in multiple layers, these operators provide increasingly abstract representations that map low-level pixel patterns to meaningful biological indicators of leaf abnormalities. This mechanism is particularly important in vineyards, where disease symptoms manifest as subtle chromatic or structural changes on leaf surfaces.

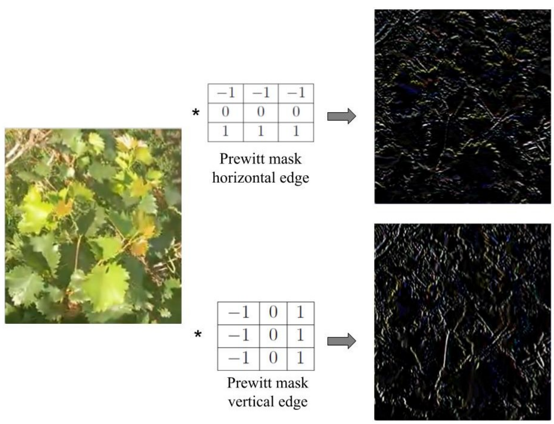

Figure 1: Extracting horizontal and vertical edges by applying two convolutional filters.

Building upon convolutional operators, Convolutional Neural Networks (CNNs) form the backbone of the applied detection models. CNNs exploit the shift-invariance and compositional nature of convolutions to achieve robust feature extraction across diverse grape varieties and geographical regions. Figure 1 shows an example of extracting horizontally and vertically oriented image features from an image belonging to the training set. Early layers typically capture local gradients, while deeper layers learn disease-specific morphology, such as lesion boundaries or necrotic spot textures. Pooling operators, often max-pooling, complement convolutions by introducing spatial downsampling, thereby reducing computational load while preserving the most informative activations. The general pipeline of the applied CNN model is presented in Figure 2. Nonlinearities such as ReLU further enhance the representational power of CNNs by enabling the modeling of complex, non-linear disease patterns.

In this work, CNN-based architectures are employed through the YOLOv7 detection framework, which integrates convolutional backbones with real-time object localization heads. The backbone network uses a sequence of convolutional blocks to build a multiscale representation capable of detecting both large and small disease spots. The detection head predicts bounding boxes and associated class probabilities using feature maps produced by these convolutional layers. YOLO-type networks rely on anchor-based or anchor-free mechanisms, but in either case, convolutional operators translate learned spatial patterns into actionable predictions. A crucial mathematical element is the IoU-based loss function, which quantifies the overlap between predicted and ground-truth regions and guides the optimization process during training. The model constantly updates convolutional parameters by minimizing this loss using stochastic gradient descent.

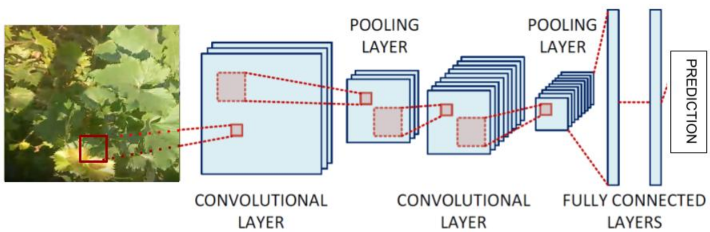

Figure 2: General pipeline of the applied Convolutional Neural Network model. The prediction (or output) contains a list of bounding box coordinates corresponding to the diseased leaf patches.

The extended pipeline also incorporates data augmentation, which can be viewed as applying mathematical transformations such as rotations, scalings, or color perturbations to expand the training distribution. These transformations improve the generalization of the convolutional filters, especially when the dataset contains images from geographically diverse wine regions. Transfer learning plays an additional role: convolutional backbones pretrained on large image datasets provide generic filters that are later fine-tuned to the specific spectral and structural characteristics of grape leaves. Because many disease features share cross-regional similarities, convolutional operators trained in one region can adapt effectively to datasets acquired elsewhere. This adaptability demonstrates the fundamental strength of CNNs as universal feature extractors.

Overall, the mathematical foundation of convolutional filtering, nonlinear activations, pooling, and gradient-based optimization [4, 5] enables reliable modeling of disease signatures in complex vineyard environments. The integration of these elements in CNNs such as YOLOv7 ensures that the system captures both fine-grained lesion patterns and broader contextual cues from aerial images. As a result, convolution-based architectures provide a scalable and region-transferable framework for automatic vine disease detection in precision agriculture.

3. Experimental results

Aerial data collection was conducted in four viticultural districts of the Carpathian Basin (Transylvania wine region in Romania, Eger wine region in Hungary, Východoslovenská wine region in Slovakia, and Fruška Gora wine region in Croatia) utilizing remotely operated quadcopters. All flights were conducted under mild weather circumstances (light wind and no precipitation) using manual piloting at low altitudes (maximum 6 meters above ground level).

For recording the dataset in a vineyard at Cluj-Napoca (Transylvania wine region), Szücsi (Eger wine region) and Ilok (Fruška Gora wine region), we used a small and light quadcopter, DJI Mini 3 with 12 MP integrated camera. At a vine parcel near Hrhov (Východoslovenská wine region), a DJI Phantom 3 Professional drone was employed. A DJI P4 Multispectral drone was also used at Cluj-Napoca. In all four locations, the video recordings and images were captured in the maximum resolution possible.

We compared various models trained in different geographical regions with our base model from Transylvania, which contains more than 10,000 annotated images and over 30,000 labels of manually annotated and validated grape leaves exhibiting abnormalities. This large-scale dataset enables geographically distributed analyses and comparisons.

We investigated the cross-domain relationship between the base Transylvanian region and the data collected in Szücsi, Hrhov, and Ilok regions. The results in terms of the Mean Average Precision (mAP) are shown in Figure 3. The mAP metrics [6] measures how well an object-detection model identifies and localizes objects by averaging the precision values computed at different recall levels. It summarizes the model's overall detection performance by combining both classification accuracy and bounding-box quality into a single score, form 0 to 1. Zero means the model detects nothing correctly, while one means perfect detection and localization. The mAP50 metric refers to the mean average precision at an intersection-over-union (IoU) threshold of 0.5, which measures how well the model predicts bounding boxes with at least 50% overlap with ground truth.

The presented results show that the best performance (highest precision) is achieved for the Cluj-Napoca region, which is a consequence of the larger available dataset used for the training process. The lower performance observed for the Szücsi region can be attributed to the fact that the grape leaves there differ significantly in texture, shape, and color from those in the other regions.

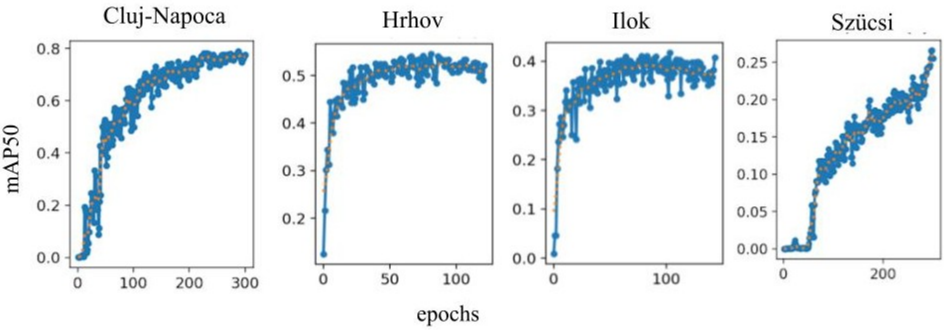

Figure 3: Mean Average Precision (mAP) metrics based on data collected in the four considered different geographical regions.

4. Conclusion

This paper presents research focused on examining disease detection in vineyards across the Carpathian Basin using low-altitude UAV platforms equipped with RGB cameras. Transfer learning plays a specific role, as convolutional backbones pretrained on large image datasets (Cluj-Napoca region) provide generic filters that are later fine-tuned to the specific spectral and structural characteristics of grape leaves in the other analysed regions (Hrhov, Ilok and Szücsi). Since many disease features share cross-regional similarities, we conclude that convolutional operators trained in one region can adapt effectively to datasets acquired in other regions. CNNs provide an excellent platform for this transfer-learning approach. As a possible future research direction, we foresee extending the field of application of the developed CNN-based algorithm, particularly to problems related to disease detection in various agricultural settings, especially for crops with characteristic leaves such as tobacco, cabbage or cotton.

Acknowledgement

The authors acknowledge the support received from the Hungarian Academy of Sciences through the Domus Hungarica project.

References

[1] L. Tamás, S. Gubo, and T. Lukić, “Vine Diseases Detection Trials in the Carpathian Region with Proximity Aerial Images,” *Proceedings of the SAMI 2024*, 2024.

[2] S. Molnár and L. Tamás, "Segmentation methods evaluation on grapevine leaf diseases," *Proceedings of the FedCSIS 2023*, 2023.

[3] S. Molnár, B. Keresztes, and L. Tam´as, "Feature pyramid network based proximal vine canopy segmentation," *Proceedings of the IFAC 2023*, 2023.

[4] T. Lukić and A. Lukity, "A Spectral Projected Gradient Optimization for Binary Tomography," *in Computational Intelligence in Engineering, vol. 313 of SCI, pp. 263–272, Springer-Verlag*, 2010.

[5] T. Lukić and P. Balázs, "Moment preserving tomographic image reconstruction model," *Image and Vision Computing, vol. 146, p. 105036*, 2024.

[6] R. Padilla, W. L. Passos, T. L. B. Dias, S. L. Netto, and E. A. B. da Silva, "A Comparative Analysis of Object Detection Metrics with a Companion Open-Source Toolkit," *Electronics, vol. 10, no. 3*, 2021.

The 10th Conference on Mathematics in Engineering: Theory and Applications
Novi Sad, December 12-14th 2025

MATHEMATICAL INSIGHT INTO THE FOURIER TRANSFORM FOR 2D IMAGE ANALYSIS[1]

Danijela Milekić [2], Tibor Lukić [3] and Lidija Krstanović [4]

https://doi.org/10.24867/META.2025.13 Review article

Abstract. This paper presents the mathematical foundations of the Fourier transform and its use in edge detection on digital images. Beyond a practical implementation, the focus is on providing a mathematical insight into how frequency-domain analysis relates to spatial intensity variations in images, including its role in modern applications such as super-resolution. A high-pass filter is applied in the frequency domain to isolate high-frequency components that correspond to edges. The theoretical concepts are supported by a numerical implementation of the 1D and 2D Fast Fourier Transform using the Python programming language. The results demonstrate that frequency-domain filtering provides a global and mathematically robust method for edge extraction, offering a deeper understanding of how changes in pixel intensity relate to frequency characteristics in digital images.

AMS Mathematics Subject Classification (2020): 68U10, 42B10

Key words and phrases: Fourier Transform, Image Analysis, Python

1. Introduction

The Fourier transform is a fundamental tool in signal and image processing, providing a link between the spatial and frequency domains. Through the Discrete Fourier Transform (DFT) and its efficient implementation, the Fast Fourier Transform (FFT), images can be analyzed and filtered based on their spectral components [1, 2].

Edges in digital images correspond to high-frequency variations, which represent rapid transitions in intensity or color. Studies have shown that combining spatial and frequency-domain information improves the robustness of edge

[1]This research has been supported by the Science Fund of the Republic of Serbia, #7449, Multimodal multilingual human-machine speech communication - AI-SPEAK, and by the Faculty of Technical Sciences, University of Novi Sad, through the project "Scientific and artistic research work of researchers in teaching and associate positions at the Faculty of Technical Sciences, University of Novi Sad 2025" (no. 01-50/295).

[2]Department of Fundamental Sciences, Faculty of Technical Sciences, University of Novi Sad, e-mail: danijelamilekic@uns.ac.rs

[3]Department of Fundamental Sciences, Faculty of Technical Sciences, University of Novi Sad, e-mail: tibor@uns.ac.rs

[4]Department of Fundamental Sciences, Faculty of Technical Sciences, University of Novi Sad, e-mail: lidijakrstanovic@uns.ac.rs

detection in complex scenes [3], while emphasizing high-frequency components enhances the extraction of fine details [4].

Beyond edge detection, frequency-domain analysis has found new applications in modern computer vision. In particular, Fourier-based techniques have contributed to super-resolution, where recovering high-frequency information leads to sharper and more detailed images [5].

This work aims to provide a concise mathematical perspective on the use of the 2D DFT in image analysis, focusing on both edge detection and resolution enhancement. The goal is to explore how classical frequency-domain techniques continue to shape modern image analysis, bridging fundamental theory with contemporary computational approaches.

2. Mathematical Foundations of the Fourier Transform

This section introduces the main mathematical concepts underlying the Fourier transform and its application to signal and image analysis.

A *signal* is a function that conveys information about a physical process over time or space. It can be either continuous (analog) or discrete (sampled, digital), with examples including audio waves, electric voltage, or images. The basic characteristics of a signal include its *amplitude* (the maximum value relative to zero, indicating signal strength), *frequency* (number of oscillations per unit time, measured in Hz) and *phase* (the wave change relative to a reference point) [6].

2.1. Discrete Fourier Transform (DFT)

The Discrete Fourier Transform converts a discrete signal from the time domain to the frequency domain.

Definition 2.1 (1D Discrete Fourier Transform [1])**.** Let $x[n]$ be a discrete signal of length N. Its DFT is defined as:

$$X[k] = \sum_{n=0}^{N-1} x[n] e^{-i\frac{2\pi}{N}kn}, \quad k = 0, 1, \ldots, N-1$$

Figure 1 illustrates a simple one-dimensional discrete signal composed of two sinusoidal components. Figure 1a shows the discrete signal in the time domain, while Figure 1b displays the corresponding magnitude spectrum obtained via the Fast Fourier Transform (FFT). The magnitude spectrum represents the strength of each frequency component: peaks appear at 50 Hz and 120 Hz, corresponding to the signal's frequency components.

The term FFT refers to a family of efficient algorithms for implementing the discrete Fourier transform [1]. While direct computation of an N-*point* DFT requires N^2 complex multiplications, FFT methods reduce this to the order of $N \log_2 N$ complex multiplications.

Remark 2.2 ([1])*.* The inverse DFT reconstructs the original signal:

$$x[n] = \frac{1}{N} \sum_{k=0}^{N-1} X[k] e^{i\frac{2\pi}{N}kn}$$

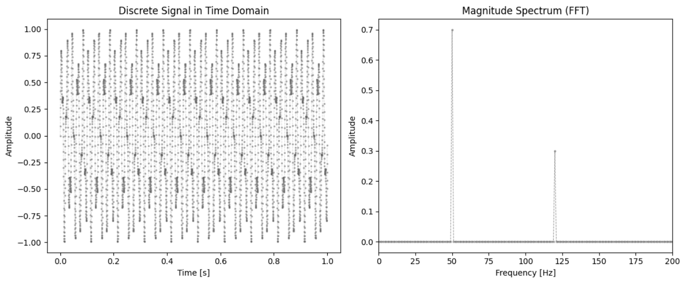

Figure 1: 1D discrete signal: (a) time domain; (b) frequency domain

2.2. 2D Discrete Fourier Transform for Images

A digital image can be interpreted as a 2D signal, i.e., a function of two discrete variables (m, n).

Definition 2.3 (2D Discrete Fourier Transform [2])**.** Let $f[m,n]$ be a 2D signal of size $M \times N$. Its 2D DFT is defined as:

$$F[u,v] = \sum_{m=0}^{M-1} \sum_{n=0}^{N-1} f[m,n] e^{-i2\pi\left(\frac{um}{M}+\frac{vn}{N}\right)}, \quad u = 0,\ldots,M-1,\ v = 0,\ldots,N-1$$

Here, $F[u,v]$ represents the *frequency spectrum* of the image, where each pair of coordinates (u,v) corresponds to a specific spatial frequency component. Low frequencies are concentrated near the center of the spectrum, describing smooth intensity variations, while high frequencies (located toward the edges) represent rapid intensity changes, such as edges and fine details [7].

Remark 2.4 ([2]). The inverse 2D DFT reconstructs the original image:

$$f[m,n] = \frac{1}{MN} \sum_{u=0}^{M-1} \sum_{v=0}^{N-1} F[u,v] e^{i2\pi\left(\frac{um}{M}+\frac{vn}{N}\right)}$$

2.3. Frequency-Domain Edge Detection

Edges in images correspond to rapid spatial intensity variations, which are captured by high-frequency components in the Fourier domain.

Definition 2.5 (High-Pass Filter [8])**.** A high-pass filter is a frequency-domain filter that suppresses low frequencies while preserving high frequencies corresponding to image edges.

Remark 2.6 ([8]). Applying the high-pass filter in the frequency domain and performing the inverse 2D DFT produces an image emphasizing edges.

Remark 2.7 ([8]). Mathematically, the filtering operation in the frequency domain can be expressed as:

$$\tilde{F}[u,v] = F[u,v] \cdot H(u,v),$$

where $H(u, v)$ is the high-pass filter mask defined as:

$$H(u, v) = \begin{cases} 0, & (u - u_0)^2 + (v - v_0)^2 \leq r^2, \\ 1, & \text{otherwise.} \end{cases}$$

Here, (u_0, v_0) denotes the center of the frequency spectrum, and r is the radius of the suppressed low-frequency region. This operation removes smooth intensity variations while retaining high-frequency components corresponding to image edges, and corresponds to the ideal high-pass filter formulation.

3. Application: Edge Detection Using FFT

The implementation of frequency-domain edge detection was carried out in Python using the `NumPy`, `Matplotlib`, and `scikit-image` libraries. A color image was first loaded and converted to grayscale, forming a two-dimensional discrete signal $f[m, n]$.

The 2D Fast Fourier Transform (FFT) was applied to map the image from the spatial domain, where pixel intensities vary with position, to the frequency domain, where the same information is represented as a combination of sinusoidal components of different frequencies. For practical filtering and visualization, the resulting frequency spectrum must be shifted (using a function `np.fft.fftshift`) to move the zero-frequency component from the corners to the center of the spectrum (see Figure 2b). In this domain, low frequencies correspond to slowly varying intensity regions (smooth areas), while high frequencies correspond to rapid intensity changes - that is, edges and fine details.

After constructing and applying the high-pass filter as defined in Section 2, the inverse FFT (`np.fft.ifft2`) was used to reconstruct the filtered image back into the spatial domain. Since only high-frequency components remain, the resulting image highlights regions with strong intensity gradients - the edges.

This implementation demonstrates the connection between the Fourier transform and edge detection: frequency-domain filtering emphasizes high-frequency components globally, which mathematically correspond to the spatial derivatives approximated by methods like Sobel or Canny edge detector.

Figure 2 shows the complete workflow of frequency-domain edge detection.

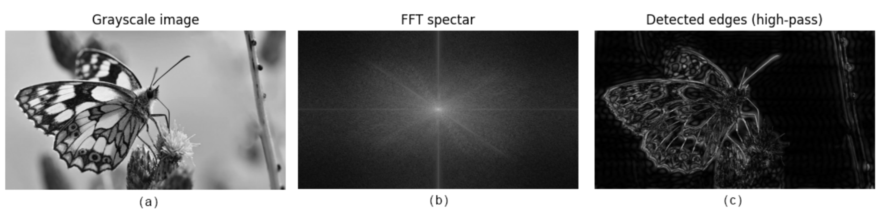

Figure 2: Edge detection: (a) original image in grayscale; (b) logarithmic magnitude spectrum; (c) edge-detected image after high-pass filtering

4. Modern Applications of the Fourier Transform

Beyond the classical applications of the Fourier transform (e.g., filtering for edge detection), recent research has explored its integration with modern machine learning and image enhancement techniques. For example, in the study [9] it was demonstrated that applying FFT-based frequency-domain conversion prior to convolutional processing significantly improves classification accuracy.

In another line of work, super-resolution methods exploit the recovery of high-frequency components via Fourier encodings to enhance image resolution. As a practical example, the method from the work [5] was implemented in Python, producing the upsampled image shown in Figure 3. The implementation was performed on a grayscale butterfly image, upsampled by a factor of four in the frequency domain. The resulting red-tinted image highlights recovered fine details and improved sharpness, while the extracted high-frequency components emphasize edges, showing how Fourier-based enhancement preserves structural boundaries and contrast.

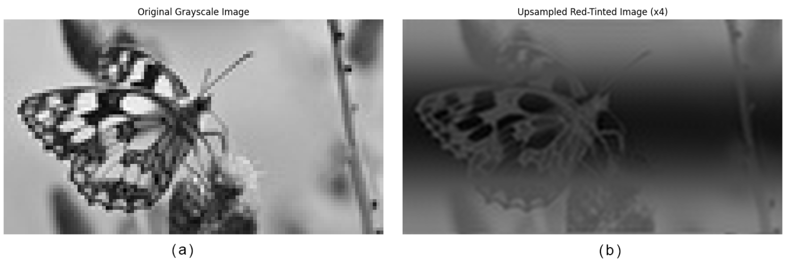

Figure 3: Super-resolution result: (a) original image; (b) upsampled image

These developments underscore that the Fourier transform remains not only a fundamental mathematical tool, but also a gateway to hybrid methods combining signal processing and deep learning. While the present study focuses on the use of the 2D DFT and high-pass filtering for edge detection, the above works point to promising future directions such as frequency-domain neural networks and super-resolution pipelines.

5. Conclusion

This paper has presented the mathematical foundations of the 2D Discrete Fourier Transform and its practical applications in image analysis. This study shows how frequency-domain filtering can be used to extract edges by isolating high-frequency components, highlighting the connection between spatial intensity variations and their spectral representation. Additionally, it discusses the role of the Fourier transform in modern image enhancement, such as super-resolution, demonstrating its continued relevance in both classical and contemporary applications. Overall, the presented work provides a clear mathematical perspective that can serve as a basis for further exploration of frequency-domain methods in image processing and hybrid approaches combining Fourier analysis with modern computational techniques.

References

[1] G. Clifford, "Chapter 3: The Discrete Fourier Transform," *Lecture Notes for 6.555/6.556 Biomedical Signal and Image Processing*, Massachusetts Institute of Technology (MIT), 2005. Available: `https://web.mit.edu/~gari/teaching/6.555/lectures/ch_DFT.pdf`

[2] ETH Zürich, "Introduction to the 2D Discrete Fourier Transform," *Lecture Notes for Signals and Systems*, ETH Zürich, 2017. Available: `https://ethz.ch/content/dam/ethz/special-interest/mavt/dynamic-systems-n-control/idsc-dam/Lectures/Signals-and-Systems/ProgEx/Introduction_2D_DFT.pdf?utm_source=chatgpt.com`

[3] Y. Guo, B. Li, W. Zhang, W. Dong, "Multi-scale image edge detection based on spatial-frequency domain interactive attention," *Frontiers in Neurorobotics*, 2025. `https://doi.org/10.3389/fnbot.2025.1550939`

[4] X. Lyu, J. Wang, T. Huang, "Spatial Frequency Enhanced Salient Object Detection," *Information Sciences*, 2024. `https://doi.org/10.1016/j.ins.2023.119460`

[5] L. Uwaydah, "Super-Resolution Using Fourier Image Transformer," *Journal of Applied Mathematics and Physics*, 2025. `https://doi.org/10.4236/jamp.2025.135097`

[6] S. Aburakhia, A. Shami, G. K. Karagiannidis, "On the Intersection of Signal Processing and Machine Learning: A Use-Case-Driven Analysis Approach," *Journal of Signal Processing and Machine Learning*, 2024. `https://doi.org/10.48550/arXiv.2403.17181`

[7] A. De Cesarei, P. Codispoti, "Early Spatial Frequency Processing of Natural Images: An ERP Study," *PLoS ONE*, 2013. `https://doi.org/10.1371/journal.pone.0065103`

[8] M. S. Sali, P. Kumar, and R. Verma, "Image Quality and Performance Analysis Using Frequency Domain High Pass Filters," *International Journal of Innovative Science, Engineering and Technology*, 2023. `https://doi.org/10.35940/ijisme.B9789.13020225`

[9] G.E. Daği, E. Gökçay, H. Tora, "Fourier-Based Image Classification Using CNN," *Journal of Science, Technology and Engineering Research*, 2024. `https://doi.org/10.53525/jster.1501920`

The 10th Conference on Mathematics in Engineering: Theory and Applications
Novi Sad, December 12-14th 2025

VIŠEKRITERIJUMSKO ODLUČIVANJE ZASNOVANO NA ENERGIJAMA FAZI SOFT SKUPOVA

Ljubica Mudrić - Staniškovski [1]

https://doi.org/10.24867/META.2025.14 Pregledni članak

Sažetak. Ovaj rad fokusiran je na metode višekriterijumskog odlučivanja zasnovane na energijama fazi soft skupova. Prikazana je primena singularnih vrednosti matrica za definisanje energije i λ-energije nekog fazi soft skupa, što omogućava efikasno donošenje odluka u uslovima nesigurnosti. Analizirane su prednosti ovog pristupa u poređenju sa drugim metodama višekriterijumskog odlučivanja, a ilustracije i praktične primene pokazuju njegovu primenljivost i pouzdanost.

AMS klasifikacija (2020): 03B52, 91B06

Ključne reči: fazi soft skupovi, energija, λ-energija, rangiranje alternativa, višekriterijumsko odlučivanje.

1. Uvod

Donošenje odluka u prisustvu nesigurnosti i nepreciznosti predstavlja jedan od ključnih izazova u mnogim naučnim i praktičnim oblastima, uključujući ekonomiju, inženjerstvo, medicinu i informacione tehnologije. Tradicionalni matematički pristupi često nisu dovoljni za modelovanje nesigurnih i nepotpunih informacija, što je motivisalo istraživače da razvijaju metode zasnovane na soft skupovima i njihovim generalizacijama.

Fazi skupovi, uvedeni od strane Zadeha [12], predstavljaju jedan od prvih formalnih pristupa za modelovanje nesigurnosti i nepreciznosti u podacima. Ovi skupovi omogućavaju predstavljanje elemenata univerzuma sa pripadnošću odredjenim stepenom, što pruža fleksibilnost u opisivanju situacija u kojima klasična logika nije dovoljna. Primena fazi skupova je naročito značajna u problemima donošenja odluka, optimizacije i kontrole, gde se parametri često ne mogu izraziti preciznim vrednostima.

Soft skupovi, uvedeni od strane Molodtsova [7], predstavljaju parametarski definisane kolekcije podskupova univerzuma, na taj način omogućavajući fleksibilno i intuitivno predstavljanje nesigurnih podataka kroz atribute i njihove vrednosti. Dalja generalizacija dovela je do fazi soft skupova, koji kombinuju fleksibilnost fazi logike sa parametrizacijom soft skupova, omogućavajući preciznije modelovanje nesigurnih i subjektivnih informacija uz relativno manju računsku složenost.

[1]Fakultet inženjerskih nauka, Univerzitet u Kragujevcu, e-mail: ljubica.mudric@kg.ac.rs

U okviru fazi soft skupova razvijen je koncept energije i λ-energije [9], koji se definiše preko singularnih vrednosti matrica reprezentacija skupa. Ovi energetski parametri omogućavaju kvantifikaciju doprinosa pojedinih elemenata sistema i predstavljaju osnovu za kreiranje efikasnih metoda višekriterijumskog odlučivanja. Korišćenjem energije fazi soft skupova moguće je sagledati i uporediti različite alternative u složenim problemima donošenja odluka, posebno kada se suočavamo sa višestrukim kriterijumima i nesigurnim informacijama.

Cilj ovog preglednog rada je da predstavi teorijske osnove fazi soft skupova, analizira koncept energije i λ-energije, i pruži pregled njihovih primena u metodama višekriterijumskog odlučivanja. Rad takođe upoređuje prednosti ovog pristupa sa drugim metodama donošenja odluka u uslovima nesigurnosti, ističući njegovu fleksibilnost i efikasnost u praktičnim problemima.

2. Fazi soft skupovi i koncept energija u visekriterijumskom odlučivanju

Fazi soft skupovi predstavljaju proširenje klasičnih soft skupova i fazi soft skupova, omogucavajući modelovanje nesigurnih i subjektivnih informacija u okviru više parametara. Svaki fazi soft skup može se prikazati u matričnom obliku [2], gde redovi odgovaraju elementima univerzuma, a kolone parametrima. Elementi matrice izražavaju stepen pripadnosti pojedinih elemenata odgovarajućim parametrima, čime se dobija numerička reprezentacija fazi soft skupa.

Pojam energije fazi soft skupa motivisan je analogijom sa energijom grafa, koju je uveo Gutman [5](1978) kao zbir apsolutnih vrednosti sopstvenih vrednosti matrice susedstva grafa. Slično tome, energija fazi soft skupa izrazava „ukupni doprinos“ elemenata sistema, kvantifikujući njegovu informativnu snagu.

Pošto svaki fazi soft skup možemo predstaviti odgovarajućom pravougaonom matricom A [2], možemo odrediti sopstvene vrednosti kvadratne matrice $A \cdot A^T$, a time i singularne vrednosti na dobro poznat način. U analizi fazi soft matrica ključnu ulogu imaju singularne vrednosti. One su kvadratni koreni nenultih sopstvenih vrednosti matrice $A \cdot A^T$ i pružaju informacije o strukturi matrice, njenoj stabilnosti i raspodeli doprinosa elemenata sistema. Singularne vrednosti omogućavaju kvantifikaciju značaja i informativnosti elemenata, što predstavlja osnovu za definisanje energija fazi soft skupova. Ovo nas dovodi do sledećih pojmova.

Definicija 2.1. [9] Energija fazi soft skupa Γ_A, u oznaci $\mathbf{E}(\Gamma_A)$, se definiše kao $\mathbf{E}(\Gamma_A) = \sum_{i=1}^{m} \sigma_i$, gde su $\sigma_1 \geqslant \sigma_2 \geqslant \ldots \geqslant \sigma_m \geqslant 0$ singularne vrednosti matrice A koja odgovara fazi soft skupu Γ_A.

Definicija 2.2. [9] λ-energija fazi soft skupa Γ_A, u oznaci $\mathbf{LE}(\Gamma_A)$, se definiše kao $\mathbf{LE}(\Gamma_A) = \sum_{i=1}^{m} \sigma_i^2$, gde su $\sigma_1 \geqslant \sigma_2 \geqslant \ldots \geqslant \sigma_m \geqslant 0$ singularne vrednosti matrice A koja odgovara fazi soft skupu Γ_A.

Ove veličine omogućavaju numeričku kvantifikaciju doprinosa elemenata sistema, i zbog svoje veze sa singularnim vrednostima predstavljaju efikasan alat za analizu i poređenje alternativa u metodama višekriterijumskog odlučivanja.

3. Primena energija fazi soft skupova u donošenju odluka

U ovom odeljku prikazujemo kako se energija i λ-energija fazi soft skupova mogu primeniti prilikom donošenja odluka. Bitan aspekt u sistemima sa više faktora jeste međuzavisnost svih elemenata: sistem funkcioniše optimalno kada svaki faktor doprinosi na svoj način. Pojedini faktori mogu da preuzmu odgovornost u nekim segmentima sistema, dok drugi segmenti ostaju nepokriveni, što može dovesti do problema ako ne postoji faktor koji pokriva određeni segment svojim kvalifikacijama. Ilustracije ovih situacija mogu se pronaći u radovima [2] i [11], pri čemu u radu [9] odluke donose na osnovu definisanih energija fazi soft skupova.

Autori u svom radu [2] uvode pojmove kardinalnog skupa i agregiranog fazi soft skupa zbog primene u algoritmu za donošenje odluka. Neka je Γ_A fazi soft skup nad univerzumom $U = \{u_1, u_2, \ldots, u_m\}$ i skupom parametara $E = \{x_1, x_2, \ldots, x_n\}$.

Kardinalni skup $c\Gamma_A$ je fazi skup nad E koji meri relativni doprinos svakog parametra skupu U. Funkcija pripadnosti kardinalnog skupa definisana je kao

$$\mu_{c\Gamma_A}(x) = \frac{|\Gamma_A(x)|}{|U|}, \quad x \in E,$$

gde $|\Gamma_A(x)|$ označava skalarnu kardinalnost fazi skupa $\Gamma_A(x)$.

Fazi soft skup Γ_A^* kombinuje informacije iz kardinalnog skupa $c\Gamma_A$ i originalnog fazi soft skupa Γ_A, tako da se funkcija pripadnosti za svaki element $u \in U$ računa kao

$$\mu_{\Gamma_A^*}(u) = \frac{1}{|E|} \sum_{x \in E} \mu_{c\Gamma_A}(x) \cdot \mu_{\Gamma_{A(x)}}(u).$$

Ovaj skup omogućava sumiranje doprinosa svih parametara za svaki element univerzuma i služi kao osnova za izbor najpovoljnijeg rešenja u algoritmu.

Metoda iz [2] sadrži algoritam za izbor najpovoljnije odluke u 4 koraka, koji glasi:

1. Konstruišemo fazi soft skup Γ_A nad U;
2. Odredimo kardinalni skup $c\Gamma_A$ od fazi soft skupa Γ_A;
3. Odredimo Γ^* na osnovu formiranog fazi soft skupa Γ_A;
4. Izaberemo najprihvatljivije rešenje tako što odredimo maksimalnu vrednost $\max \mu_{\Gamma_A^*}(u)$.

U radu [9] autori predstavljaju sličan algoritam, ali koristeći definisane pojmove energije i λ-energije fazi soft skupova. Algoritam za donošenje odluka zasnovan na energijama glasi:

1. Formiramo fazi soft skup Γ_A nad U;
2. Formiramo fazi soft skupove Γ_{A_i} nad $U \setminus \{u_i\}$ za svako $u_i \in U$;

3. Odredimo energije $E(\Gamma_{A_i})$ (ili λ-energije $LE(\Gamma_{A_i})$) za svaki fazi soft skup Γ_{A_i};

4. Odredimo minimalnu energiju od svih energija fazi soft skupova dobijenih u koraku 3 i interpretiramo dobijeni rezultat.

4. Analiza i diskusija

Metode višekriterijumskog odlučivanja zasnovane na energijama fazi soft skupova pružaju sistematičan pristup u evaluaciji alternativa pri prisustvu nesigurnosti i nepreciznih podataka. Energija i λ-energija fazi soft skupova, omogućavaju kvantifikaciju doprinosa svake alternative i identifikaciju ključnih faktora u sistemu.

Ovaj pristup je praktično primenjen, u radu [10] pri izboru cloud platformi u IT sektoru, gde rangiranje alternativa i kvantifikacija doprinosa atributa omogućavaju precizno donošenje odluka i povećanje zadovoljstva korisnika.

Upoređujući različite metode, možemo izdvojiti sledeće karakteristike:

1. Metoda zasnovana na fs-agregaciji ([2]) omogućava agregaciju fazi soft skupova i daje jedinstveno rešenje, ali zahteva upotrebu brojnih novih termina i konceptualno je složenija.

2. Metoda zasnovana na vrednostima nivoa soft skupa ([4]) koristi relativno grube kriterijume i ne garantuje jedinstveno rešenje, što može dovesti do nepreciznosti pri donošenju odluka.

3. Metode zasnovane na energiji i λ-energiji fazi soft skupova [9] daju jedinstveno rešenje u većini slučajeva.

Pored toga, metode zasnovane na energijama fazi soft skupova mogu se integrisati sa drugim metodama višekriterijumskog odlučivanja, što dodatno proširuje njihove mogućnosti u složenim problemima odlučivanja. Konkretno, kombinovanje sa metodama poput IT2FTOPSIS [8] ili drugim pristupima zasnovanim na tip-2 fazi skupovima [3], [6] omogućava dodatnu fleksibilnost i preciznost u rangiranju alternativa. Poredjenje ovih pristupa sa standardnim metodama izvršeno je u radu [10], gde je pokazano da primena energije i λ-energije fazi soft skupova dovodi do konzistentnih i pouzdanih rezultata pri izboru cloud platformi u IT sektoru.

Prednosti metoda zasnovanih na energijama fuzzy soft skupova uključuju:

1. Jedinstvenu identifikaciju najboljih alternativa u većini problema, uz mogućnost rangiranja svih alternativa.

2. Jasnu interpretaciju doprinosa pojedinih atributa u ukupnom sistemu.

3. Konzistentnost sa postojećim metodama i mogućnost integracije sa standardnim tehnikama višekriterijumskog odlučivanja.

4. Fleksibilnost u primeni na različite vrste problema, uključujući one sa nesigurnim i nepreciznim podacima.

Glavne ograničenja uključuju subjektivnost u definisanju kriterijuma, jednako ponderisanje atributa u trenutnim modelima i relativno složen izračunavanje energija za velike skupove podataka. Medjutim, prednost ovih metoda u preciznom rangiranju i identifikaciji ključnih faktora čini ih značajnim alatom u donošenju odluka u realnim scenarijima.

5. Zaključak

U ovom radu analizirane su metode višekriterijumskog odlučivanja zasnovane na energijama i λ-energiji fazi soft skupova. Ključna zapažanja su:

- Uvođenje energije i λ-energije kao numeričkih karakteristika fazi soft skupova omogućava kvantifikaciju doprinosa alternativa i atributa.
- Metode zasnovane na energijama omogućavaju jedinstveno rangiranje alternativa, dok u izuzetnim slučajevima više rešenja nastaje samo u specifičnim uslovima jednakosti matrica.
- Pristup zasnovan na korišćenju energija pruža jasnu i intuitivnu interpretaciju doprinosa atributa i alternativa u ukupnom sistemu.
- Poređenje sa postojećim metodama pokazuje da pristup zasnovan na energijama fazi soft skupova kombinovan sa singularnim vrednostima matrica omogućava preciznija i konzistentnija rešenja.
- Metodologija je fleksibilna i primenljiva na različite probleme višekriterijumskog odlučivanja sa nesigurnim podacima.

Buduća istraživanja mogu se fokusirati na:

- Istraživanje maksimuma energije fazi soft skupa i konstrukciju fuzzy soft skupova sa zadatom energijom.
- Primenu različitih tipova fazi brojeva i ponderisanja kriterijuma za povećanje fleksibilnosti metoda.
- Razvoj softverskih alata koji automatizuju izračunavanje energije i λ-energije za velike skupove podataka.
- Generalizaciju metoda na (a, b)-fazi soft skupove uvedene u radu [1], kao i dodatna istraživanja u vezi sa singularnom vrednošću matrica.

Integracija energije iz teorije grafova kao motivacije, uz upotrebu singularnih vrednosti matrica, omogućava konceptualno novu perspektivu u analizi fazi soft skupova i njihovoj primeni u višekriterijumskom odlučivanju.

Literatura

[1] T. M. Al-shami, J. C. R. Alcantud, A. Mhemdi, "New generalization of fuzzy soft sets: (a, b)–Fuzzy soft sets", AIMS Mathematics, vol. 8(2), pp. 2995-3025, 2023.

[2] N. Çağman, S. Enginoglu, F. Citak, "Fuzzy Soft Set Theory and Its Applications", Iranian Journal of Fuzzy Systems vol. 8 (3), pp. 137-147, September and October 2011.

[3] E. Celik, M. Gul, N. Aydin, A. T. Gumus, A. F. Guneri, "A comprehensive review of multi criteria decision making approaches based on interval type-2 fuzzy sets", Knowledge-Based Systems, vol. 85, pp. 329-341, 2015.

[4] F. Feng, J. B. Jun, X. Liu, L. Li, "An adjustable approach to fuzzy soft set based decision making", Journal of Computational and Applied Mathematics, vol. 234, pp. 10-20, May 2010.

[5] I. Gutman, "The energy of a graph", Ber. Math.Statist. Sekt. Forschungsz. Graz 103, pp. 1-22, 1978.

[6] N. Komatina, D. Tadić, G. Djurić, A. Aleksić, "Determination of manufacturing process failures priority under type 2 fuzzy environment: Application of genetic algorithm and Variable neighborhood search", Proceedings of the Institution of Mechanical Engineers, Part E, Journal of Process Mechanical Engineering, 09544089231160510, 2023.

[7] D. Molodtsov, "Soft set theory-first results", Computers and Mathematics with Applications vol. 37, pp. 19-31, February and March 1999.

[8] J. M. Mendel, "Uncertain rule-based fuzzy systems", Introduction and new directions, 684, 2017.

[9] Lj. Mudrić- Staniškovski, Lj. Djurović, N. Stojanović, "Energy of a fuzzy soft set and its application in decision-making", Iranian Journal of Fuzzy Systems, vol. 21(2), pp. 35-49, March and April 2024.

[10] Lj. Mudrić- Staniškovski, I. Spasenić, D. Tadić, N. Stojanović, "Evaluation and selection of cloud platforms in a fuzzy environment", Journal of Intelligent and Fuzzy Systems: Applications in Engineering and Technology, vol 49. pp. 1-13, July 2025.

[11] S. K. Pezuk, G. Senel, "An Application of Soft Multisets to a Decision-Making Problem Concerning Side Effects of COVID-19 Vaccines", Journal of New Theory, vol. 35, pp. 103-113, June 2021.

[12] L. A. Zadeh, "Fuzzy sets", Information and Control, vol. 8, pp. 338-353, June 1965.

The 10th Conference on Mathematics in Engineering: Theory and Applications
Novi Sad, December 12-14th 2025

ORIENTATION-ASSISTED NULL SPACE SEARCH FOR TOMOGRAPHY RECONSTRUCTION

Tamara Palalić [1] and Tibor Lukić [2]

https://doi.org/10.24867/META.2025.15 Review article

Abstract. This paper contains a review of Tomography Reconstruction based on Null Space Search, with an accent on application and using orientation as a prior information.

AMS Mathematics Subject Classification (2020): 68U10, 94A08

Key words and phrases: Tomography, Null Space, Orientation

1. Introduction

Tomography is a branch of image processing concerned with reconstructing unknown images from given projection data. Mathematically, an image can be represented as a function whose range may be continuous or discrete. In Computerized Tomography (CT), this image function has a continuous range. Discrete Tomography (DT) is a subfield of tomography in which the image function takes values from a finite and discrete set. When this range includes only a few predefined intensity levels, the method is called Multi-Level Tomography. A special case of this is Binary Tomography, where the image contains only two intensity values—usually 0 and 1.

Numerous methods have been proposed in the literature to solve the tomography reconstruction problem. Among the most well-known iterative algorithms are the Algebraic Reconstruction Technique (ART)[[8]], the Simultaneous Iterative Reconstruction Technique (SIRT)[[7]], the Discrete Algebraic Reconstruction Technique (DART)[[9]], the Spectral Projected Gradient (SPG) method[[10]], and the Difference of Convex functions (DC) algorithm. A common characteristic of these approaches is that they iteratively adjust the pixel intensities to reduce the projection error—i.e., they minimize the difference between the measured and reconstructed projections during convergence.

This limitation motivated us to develop a new reconstruction technique in which the projection error remains unchanged throughout the iterative process. Since the projection data are typically the most reliable information about the unknown image, maintaining a minimal projection error is crucial. The proposed method addresses this issue by ensuring that, during reconstruction, the projection error theoretically remains constant at zero or in practical applications, very close to zero.

[1]Department of Fundamental Sciences, Faculty of Technical Sciences, University of Novi Sad, e-mail: palalict@uns.ac.rs

[2]Department of Fundamental Sciences, Faculty of Technical Sciences, University of Novi Sad, e-mail: tibor@uns.ac.rs

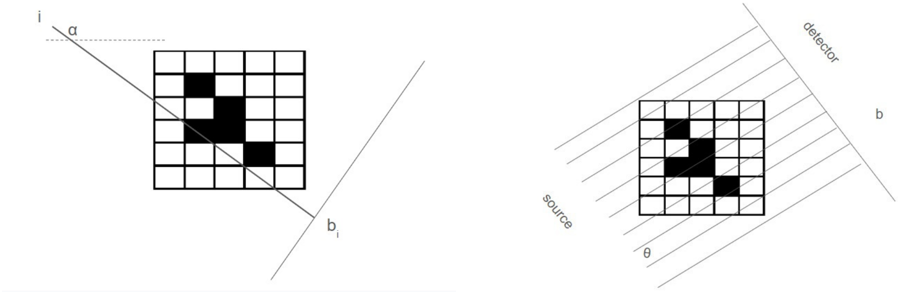

Figure 1: Transmision tomography reconstruction model from two different projection angles. Left image represent i-th projection ray from the projection angle α passing through the object, and it's detected projection value b_i. Right image represent set of parallel projection rays from the projection angle θ.

2. Definitions

Mathematically, the problem of tomography reconstruction may be formulated by the following system of linear equations

$$Au = b, \quad A \in \mathbb{R}^{m\times n}, \;\; u \in \mathbb{R}^n, \;\; b \in \mathbb{R}^m, \tag{2.1}$$

where u represents the unknown image that should be reconstructed. In the case of binary tomography, the components of vector u have only two different values, usually 0 and 1. Rows of matrix A (projection matrix) hold information about the length of the projection ray that passes through the pixel. The assumption is that each pixel is represented as a square with unit side length, see Figure 1. The figure represents the projection value calculation for a given image from one projection direction denoted by angle α. The another projection direction is obtained by rotation source-detector system around of the center of the circle. Each projection direction contributes a new parallel set of the projection rays. Detected projection values are placed in the projection vector b.

In the reconstruction problem, both the matrix A and the projection vector b are given, as a calculated or measured data. The task is to determine the unknown image u. The system (2.1) is often underdetermined ($m << n$), and consequently, in general case, we can count on an infinite number of possible solutions.

3. Tomography Reconstruction Based on Null Space Search (NSST)

The main idea uses the fact that any solution of the projection linear system of equations (2.1)

$$Au = b,$$

can be represented as a sum of one particular solution u_p ($A\,u_p = b$) and an appropriate vector belongs to the null space of the matrix A, defined by

$$\mathcal{N}(A) = \{x \in \mathbb{R}^n \mid A\,x = 0\}.$$

It is known the set of all solutions can be represented as

$$u_p + z, \quad \text{where} \quad z \in \mathcal{N}(A).$$

We will denote a basis of the vector space $\mathcal{N}(A)$ by the set of vectors $\{\mathbf{b}_1, \mathbf{b}_2, \ldots \mathbf{b}_k\}$, where $k = n - m$. Each solution of the system (2.1) may be represented in the following form

$$\begin{gathered} w(\alpha) = u_p + \alpha_1\mathbf{b}_1 + \alpha_2\mathbf{b}_2 + \ldots + \alpha_k\mathbf{b}_k, \\ \text{where } \alpha = (\alpha_1, \alpha_2, \ldots, \alpha_k) \in \mathbb{R}^k \text{ and } \mathbf{b}_i \in \mathbb{R}^n \text{ for all } i = 1, \ldots, k. \end{gathered} \tag{3.1}$$

Further, it is necessary to choose coefficients $\alpha_1, \alpha_2, \ldots \alpha_k$ in α in a such way that the obtained solution $w(\alpha) \in \mathbb{R}^n$ lies in a predefined area, for example in the hyper cube $[0,1]^n$. There, we get an optimization problem that has to be solved. The whole procedure is described in detail in the paper [[1], [3]]. The described NSST method is significantly practical and applicable for low-dose and limited-angle computed tomography (CT). Because the method can reconstruct images from a small number of projections, it is valuable in scenarios where radiation exposure must be minimized (e.g., pediatric imaging). It can also reconstruct images when full rotational access around the patient is not possible, such as in mobile CT systems or dental imaging. In industrial non-destructive testing, components are often too large or heavy to rotate freely, leading to incomplete projection data. The approach is particularly beneficial for composite materials or additive manufacturing quality control, where internal structures may be known to possess certain regularities or symmetries that can be incorporated as prior information.

4. Orientation

In this section, we want to use orientation of the object to improve quality of Tomography Reconstruction. First, we will give a short reminder of object orientation. The most usual definition refers on axis of the least second moment of inertia.This is the line which minimizes the integral of the squared distances of the points (whose belong to the object) to the line. Mathematicaly, we want to optimize the integral

$$\iint_S r^2(x, y, \alpha, \rho)\,dxdy \tag{4.1}$$

where $r(x, y, \alpha, \rho)$ is the distance from the point (x, y) to the line $X\sin\alpha - Y\cos\alpha = \rho$. As a result of the optimization, it is obtained formula for the shape orientation θ given by

$$\mathrm{tg}(2\theta) = \frac{2\overline{m}_{1,1}(S)}{\overline{m}_{2,0}(S) - \overline{m}_{0,2}(S)} \tag{4.2}$$

where $\overline{m}_{i,j}(S)$ is central geometric moment i, j [[2]] for the planar shape S. On the other hand, we can observe orientation as a line u on which there is the greatest dispersion of the projected points of the object, ie. this one who takes a maximum of information of object:

$$\max_u \sum_i \left(x_i^T \cdot u\right)^2 u^T u = 1,$$

where x_i is point that belong to the object. Therefore, we have the optimization problem with constraint whose solution satisfies a matrix equation. The eigenvector of that matrix represents shape orientation. Also, it is the principal component 1 (PC1) whose carry maximum of information of object.

We will use orientation as an angle of projection and also the angle which is normal to orientation [[2]] to improve reconstruction.

We used original phantom images, Fig 2.

PH1 PH2

Figure 2: Original phantom images used in our experimental work

Here, it is presented a short experimental work with previous phantoms. We tested if using orientation will improve reconstruction process. The common feature of these phantoms is object elongation, ie. object with high elongation are suitable for this type of improving reconstruction process. In all cases, regardless of the projective direction projection error (PE) has a very small value, approximately $9.8 \cdot 10^{-8}$. That is expected because it's the main advantage of NSST. Reconstruction error $E_R(u^r) = \sum_{i=1}^{n} |u_i^r - u_i^*|$, is significantly smaller in case we use shape orientation and angle normal to orientation. For phantom PH1 reconstruction error is 537 in case using horizontal and vertical projection direction, and 59 when using orientation, see Figure 3. First column is for central reconstruction, second for binary reconstructions and third for presentation of misclassified pixel. For phantom PH2, situation is 740 to 42 in favor of NSST, Figure 4. The best situation is absolute reconstruction, i.e. when error is equal to zero, but we are satisfied when it is as much as possible close to zero.

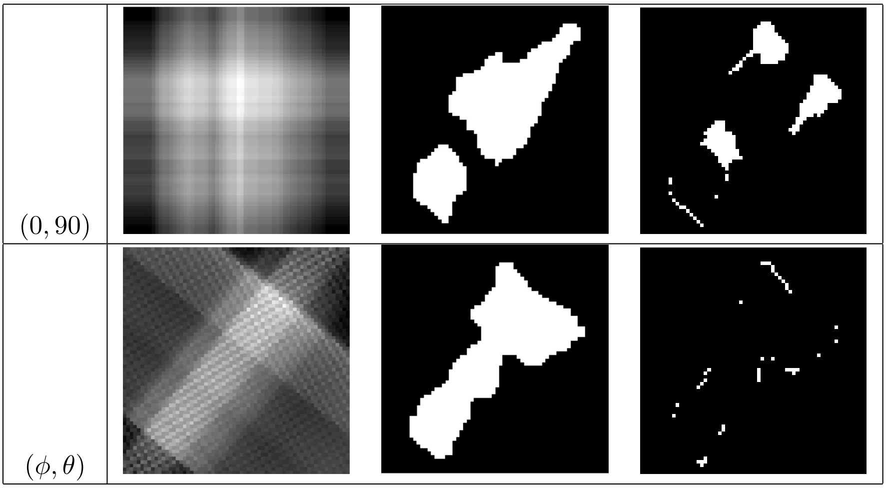

Figure 3: Comparison of central reconstruction, binary reconstruction and difference between original and binary reconstruction for PH1 in case using $(0, 90)$ or (ϕ, θ) where θ is angle of orientation and ϕ is normal to orientation.

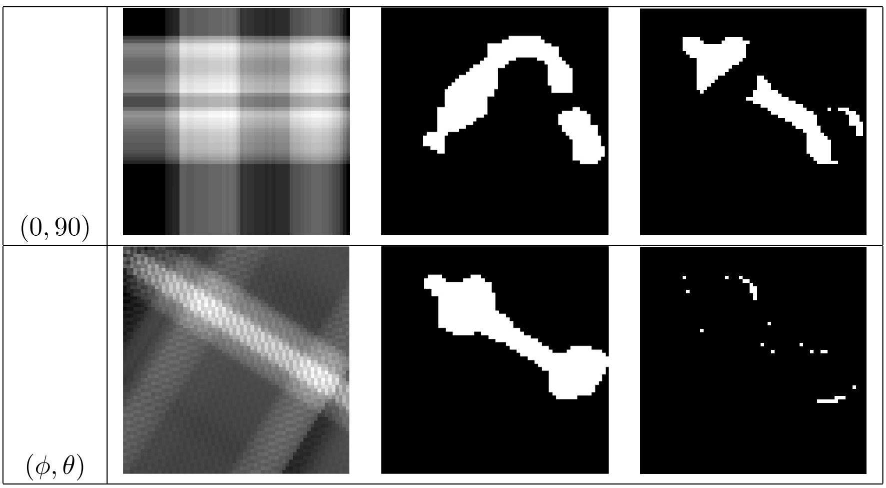

Figure 4: Comparison of central reconstruction, binary reconstruction and difference between original and binary reconstruction for PH2 in case using $(0, 90)$ or (ϕ, θ) where θ is angle of orientation and ϕ is normal to orientation.

5. Conclusion

The Tomography Reconstruction based on Null Space Search is briefly described with the emphasis on application. Also, we used an orientation to improve reconstruction. There are several ways to continue the research, both by using a prior information and by changing the focus on multi-level images.

Acknowledgement

Authors acknowledge the financial support of Department of Fundamental Sciences, Faculty of Technical Sciences, University of Novi Sad, in the frame of the Project "Socio-technological aspects of improving the teaching process in the English language in fundamental disciplines".

References

[1] T.Palalić, T. Lukić, "Tomografska rekonstrukcija bazirana na pretraživanju nula prostora", *The 9th Conference on Mathematics in Engineering: Theory and Applications Novi Sad*, June 01-03th 2024

[2] T.Palalić, T. Lukić, "Izbor projektivnog pravca u tomografskoj rekonstrukciji", *The 8th Conference on Mathematics in Engineering: Theory and Applications Novi Sad*, May 26-28th, 2023

[3] T. Lukić, T. Kopanja *Tomography Reconstruction Based on Null Space Search.* Proceedings of the twenty-first International Workshop on Combinatorial Image Analysis (IWCIA 2022), Messina, Italy, Lecture Notes in Computer Science,Volume 13348, pp. 247–259, Springer-Verlag, 2023.

[4] G. T. Herman, *Image reconstruction from Projections.* Springer-Verlag, 1980

[5] G. T. Herman, A. Kuba, *Advances in Discrete Tomography and Its Applications.*, Birkhauser, 2007

[6] G. T. Herman, A. Kuba *Discrete Tomography: Foundations, Algorithms and Applications.* Birkhauser, 1999

[7] P. Gilbert, *Iterative methods for the three-dimensional reconstruction of an object from projections.* Journal of Theoretical Biology 36(1), 105–117, 1972.

[8] R. Gordon, R. Bender, G. T. Herman, *Algebraic reconstruction techniques (ART) for three-dimensional electron microscopy and xray photography.* Journal of Theoretical Biology 29(3), 471–481, 1970.

[9] K.J. Batenburg, J. Sijbers, *Dart: A practical reconstruction algorithm for discrete tomography.* IEEE Transactions on Image Processing 20, 2011

[10] E. Birgin, J. Martinez. *Spectral Conjugate Gradient Method for Unconstrained Optimization.* Appl. Math. Optimization 43, 117–128, 2001

[11] T.I.Jolliffe *Principal Component Analysis.* Springer, 2002 / 2016.

The 10th Conference on Mathematics in Engineering: Theory and Applications
Novi Sad, December 12-14th 2025

USREDNJENE KVADRATURNE FORMULE NA PROSTORU TRIGONOMETRIJSKIH POLINOMA

Nevena Z. Petrović [1]

https://doi.org/10.24867/META.2025.16 Pregledni članak

Sažetak.
U ovom radu predstavićemo usrednjene kvadraturne formule bazirane na Gaussovim i anti-Gaussovim kvadraturnim formulama koje su definisane na prostoru trigonometrijskih polinoma, kao i usrednjene Szegő ve kvadraturne formule. Daćemo kratak opis načina njihovog konstruisanja i na kraju analizirati prednosti korišćenja jednog metoda u odnosu na drugi.

AMS klasifikacija (2020): 65D30, 65D32

Ključne reči: kvadraturne formule, ortogonalni polinomi, rekurentne relacije, težinske funkcije

1. Uvod

Numerička integracija je oblast numeričke matematike koja se bavi približnim izračunavanjem vrednosti određenih integrala, koristeći vrednosti podintegralne funkcije na nekom skupu tačaka. Formule za aproksimaciju vrednosti jednostrukih integrala nazivamo kvadraturnim formulama ili kvadraturama. Poznate Gaussove kvadraturne formule, uvedene 1814. godine [1], postižu maksimalni algebarski stepen tačnosti. Od tada su ove kvadraturne formule razmatrane od strane mnogih naučnika i generalizovane u više pravaca. Konstruisane su formule Gaussovog tipa na drugim linearnim prostorima, kao što su prostor trigonometrijskih polinoma, prostor racionalnih funkcija, itd. Prvi radovi u oblasti kvadraturnih formula Gaussovog tipa za trigonometrijske polinome publikovani su od strane ruskih matematičara Turetzkiiog i Mysovskikhog [11, 12, 15], a u poslednje dve decenije su se ovom oblašću bavili i profesori G. V. Milovanović, M. P. Stanić, A. S. Cvetković i T. V. Tomović Mladenović [8, 9, 10, 14]. Njihova pažnja bila je usmerena na proučavanje trigonometrijskih polinoma celobrojnog i polu-celobrojnog stepena, njihovu primenu na konstruisanje kvadraturnih formula, kao i ocene njihovih ostataka.

Označimo sa w težinsku funkciju, koja je integrabilna i nenegativna na intervalu $[-\pi, \pi)$. Za svaki nenegativan ceo broj n, $\mathcal{T}_n$ će predstavljati linearni prostor svih trigonometrijskih polinoma stepena manjeg ili jednakog n.

[1]Katedra za opšte obrazovne nauke, Fakultet za mašinstvo i građevinarstvo u Kraljevu, Univerzitet u Kragujevcu, e-mail: nevena.z.petrovic@pmf.kg.ac.rs

Posmatrajmo integral:

$$\widehat{I}f = \int_{-\pi}^{\pi} f(x)w(x)dx.$$

U nastavku ćemo analizirati usrednjene kvadraturne formule za aproksimaciju ovog integrala.

2. Usrednjene GAUSSove kvadraturne formule

Sa $\{A_k\}_{k\in\mathbb{N}_0}$, $A_k \in \mathcal{T}_n$, označimo niz trigonometrijskih polinoma ortogonalnih na intervalu $[-\pi, \pi)$ u odnosu na skalarni proizvod

$$\langle f, g\rangle_w = \widehat{I}(fg). \tag{2.1}$$

Tada je odgovarajuća GAUSSova kvadraturna formula

$$\widehat{G}_{\widetilde{n}+1} f = \sum_{k=0}^{\widetilde{n}} \omega_k f(x_k), \quad \widetilde{n} = 2(n-1/2), \tag{2.2}$$

tačna za sve trigonometrijske polinome $t \in \mathcal{T}_{2n-1}$ ako i samo ako su čvorovi x_k, $k = 0, 1, \ldots, \widetilde{n}$ nule trigonometrijskog polinoma $A_n \in \mathcal{T}_n$.

Vođeni idejom DIRK LAURIEja [7], koji je 1996. godine uveo pojam anti-GAUSSovih kvadraturnih formula na prostoru algebarskih polinoma, sa osobinom da daju grešku jednake veličine ali suprotnog znaka u odnosu na grešku nastalu primenom odgovarajuće GAUSSove kvadrature, krećemo u konstruisanje anti-GAUSSovih kvadraturnih formula $\widehat{H}_{\widetilde{n}+3}$ na prostoru trigonometrijskih polinoma (videti [13]). Postavljajući navedeni uslov $(\widehat{H}_{\widetilde{n}+3} - \widehat{I})f = -(\widehat{G}_{\widetilde{n}+1} - \widehat{I})f$, dolazimo do posmatranja bilinearne forme:

$$(f, g)_w = (2\widehat{I} - \widehat{G}_{\widetilde{n}+1})(fg). \tag{2.3}$$

Sa $\{B_k\}_{k\in\mathbb{N}_0}$ ćemo označavati niz trigonometrijskih polinoma ortogonalnih u odnosu na bilinearnu formu (2.3). Odgovarajuća GAUSSova kvadratura ima $\widetilde{n}+1$ čvor, dok će odgovarajuća anti-GAUSSova kvadraturna formula imati $\widetilde{n}+3$ čvora (zbog $n \mapsto n+1$), pa će ona biti oblika $\widehat{H}_{\widetilde{n}+3} = \sum_{k=0}^{\widetilde{n}+3} \widehat{\omega}_k f(\widehat{x}_k)$. Čvorovi ove anti-GAUSSove kvadraturne formule su zapravo nule trigonometrijskog polinoma

$$B_{n+1}(x) = \sum_{k=0}^{n+1} \left(p_k \cos(kx) + q_k \sin(kx)\right), \quad |p_{n+1}| + |q_{n+1}| \neq 0.$$

Specijalno, izborom $(p_{n+1}, q_{n+1}) = (1, 0)$ i $(p_{n+1}, q_{n+1}) = (0, 1)$ dobijamo trigonometrijske polinome sa vodećim kosinusnim, odnosno sinusnim, termom

$$B_{n+1}^C(x) = \cos(n+1)x + \sum_{k=0}^{n} \left(p_k^{(n+1)} \cos(kx) + q_k^{(n+1)} \sin(kx)\right),$$

$$B_{n+1}^S(x) = \sin(n+1)x + \sum_{k=0}^{n} \left(r_k^{(n+1)} \cos(kx) + s_k^{(n+1)} \sin(kx)\right),$$

redom. Nadalje ćemo posmatrati samo parne težinske funkcije w na intervalu $(-\pi,\pi)$. Tada imamo:

$$B_{n+1}^C(x)=\sum_{k=0}^{n+1} p_k^{(n+1)}\cos(kx),\qquad \text{pri čemu je}\qquad p_{n+1}^{(n+1)}=1,$$
$$B_{n+1}^S(x)=\sum_{k=0}^{n+1} s_k^{(n+1)}\sin(kx),\qquad \text{pri čemu je}\qquad s_{n+1}^{(n+1)}=1.$$

Lako se dolazi do zaključka da polinomi B_{n+1}^C i B_{n+1}^S zadovoljavaju tročlane rekurentne relacije:

$$B_{n+1}^C(x)=\left(2\cos x-a_{n+1}^{(1)}\right)B_n^C(x)-a_{n+1}^{(2)}B_{n-1}^C(x),\tag{2.4}$$
$$B_{n+1}^S(x)=\left(2\cos x-d_{n+1}^{(1)}\right)B_n^S(x)-d_{n+1}^{(2)}B_{n-1}^S(x),\tag{2.5}$$

pri čemu se koeficijenti računaju na osnovu vrednosti odgovarajućih bilinearnih formi. Formule za određivanje ovih koeficijenata mogu se naći u radu [13], gde je takođe pokazano da važi $B_k^C(x)=A_k^C(x)$ i $B_k^S(x)=A_k^S(x)$ za sve $k=0,1,\dots,n$, pa je za određivanje polinoma $B_{n+1}(x)$ dovoljno samo jednom primeniti navedenu rekurentnu relaciju.

U radu [13] pokazali smo kako na jednostavan način možemo konstruisati anti-Gaussove kvadrature na prostoru trigonometrijskih polinoma, koristeći čvorove i težinske koeficijente iz već poznatih anti-Gaussovih kvadratura na prostoru algebarskih polinoma. U nastavku navodimo ove rezultate bez dokaza.

Lema 2.1 ([13])**.** *Neka je w parna težinska funkcija na intervalu $(-\pi,\pi)$ i neka su τ_k i σ_k, $k=1,\dots,n+1$, čvorovi i težinski koeficijenti anti-*Gauss*ove kvadraturne formule sa $n+1$ čvorom, konstruisane na prostoru algebarskih polinoma u odnosu na težinsku funkciju $u_1(x)=w(\arccos x)/\sqrt{1-x^2}$ na $(-1,1)$. Tada se težinski koeficijenti $\widehat{\omega}_k$ i čvorovi $\widehat{x}_k$, $k=0,1,\dots,2n+1$, anti-*Gauss*ove kvadrature sa $2n+2$ čvora, konstruisane u odnosu na težinsku funkciju w, mogu odrediti pomoću formula:*

$$\begin{aligned}\widehat{\omega}_k&=\widehat{\omega}_{2n+1-k}=\sigma_{k+1}, && k=0,1,\dots,n,\\ \widehat{x}_k&=-\widehat{x}_{2n+1-k}=-\arccos\tau_{k+1}, && k=0,1,\dots,n.\end{aligned}$$

Lema 2.2 ([13])**.** *Neka je w parna težinska funkcija na intervalu $(-\pi,\pi)$ i neka su τ_k i σ_k, $k=1,\dots,n+1$, čvorovi i težinski koeficijenti anti-*Gauss*ove kvadraturne formule sa $n+1$ čvorom, konstruisane na prostoru algebarskih polinoma u odnosu na težinsku funkciju $u_2(x)=\sqrt{1-x^2}\,w(\arccos x)$ na $(-1,1)$. Tada se težinski koeficijenti $\widehat{\omega}_k$ i čvorovi $\widehat{x}_k$, $k=0,1,\dots,2n+1$, anti-*Gauss*ove kvadraturne formule sa $2n+2$ čvora, konstruisane u odnosu na težinsku funkciju w, mogu odrediti na sledeći način:*

$$\begin{aligned}\widehat{\omega}_k&=\widehat{\omega}_{2n+1-k}=\frac{\sigma_{k+1}}{1-\tau_{k+1}^2}, && k=0,1,\dots,n,\\ \widehat{x}_k&=-\widehat{x}_{2n+1-k}=-\arccos\tau_{k+1}, && k=0,1,\dots,n.\end{aligned}$$

Sada, kada imamo konstruisane GAUSSove kvadraturne formule $\widehat{G}_{\widetilde{n}+1}f$ i anti-GAUSSove kvadraturne formule $\widehat{H}_{\widetilde{n}+3}f$, možemo uvesti takozvane *usrednjene* GAUSS*ove kvadraturne formule* na prostoru trigonometrijskih polinoma:

$$\widehat{A}_{2\widetilde{n}+4}f = \frac{1}{2}\left(\widehat{G}_{\widetilde{n}+1} + \widehat{H}_{\widetilde{n}+3}\right) f.$$

Ove formule će imati tačnost $\widetilde{n}+2$, odnosno jednakost $\widetilde{I}f = \widehat{A}_{2\widetilde{n}+4}f$ će biti ispunjena za sve $f \in \mathcal{T}_{\widetilde{n}+2}$.

3. Usrednjene SZEGŐve kvadraturne formule

Poznato je da su SZEGŐve kvadraturne formule primenljive na integraciju periodičnih funkcija na jediničnoj kružnici. Godine 2007. KIM i REICHEL su u radu [6] uveli anti-SZEGŐve kvadraturne formule koje karakteriše osobina da je greška nastala primenom ove kvadraturne formule na LAURENTove polinome stepena ne većeg od n jednaka proizvodu negativne konstante i greške dobijene primenom SZEGŐve kvadraturne formule sa n čvorova, odnosno

$$(I - A^{(n)}_{\mu,\tau})p = -c(I - S^{(n)}_{\mu,\tau})p, \qquad \text{za sve} \qquad p \in \Lambda_{-n,n},$$

gde je sa $S^{(n)}_{\mu,\tau}$ označena SZEGŐva kvadraturna formula sa n čvorova, a sa $A^{(n)}_{\mu,\tau}$ odgovarajuća anti-SZEGŐva kvadratura. Koristeći ove kvadraturne formule, JAGELS, REICHEL i TANG su u radu [5] definisali uopštene usrednjene SZEGŐve kvadrature koje su tačne za sve LAURENTove polinome prostora $\Lambda_{-n+1,n-1}$.

Bazirano na analizi odgovarajućih para-ortogonalnih polinoma, pokazano je da se čvorovi uopštene usrednjene SZEGŐve kvadraturne formule računaju kao sopstvene vrednosti unitarne gornje HESSENBERGove matrice $\breve{H}_{2n-2}(\tau)$, dimenzije $(2n-2)\times(2n-2)$. Ova matrica određena je parametrom τ sa jedinične kružnice i takozvanim SCHURovim parametrima $\gamma_1,\ldots,\gamma_{n-1}$, koji se javljaju kao koeficijenti u rekurentnim relacijama ovih polinoma. Težinski koeficijenti se tada mogu izračunati kao kvadrati prvih komponenti odgovarajućih jediničnih sopstvenih vektora (videti [5], [6]). Takođe, pokazano je da se pomenuta gornja HESSENBERGova matrica $\breve{H}_{2n-2}(\tau)$ može predstaviti u obliku $\breve{H}_{2n-2}(\tau) = \widehat{D}^{-1/2}_{2n-2}\widehat{H}_{2n-2}(\tau)\widehat{D}^{1/2}_{2n-2}$, gde je

$$\widehat{H}_{2n-2}(\tau) = \begin{bmatrix} -\bar{\gamma}_0\gamma_1 & -\bar{\gamma}_0\gamma_2 & \cdots & -\bar{\gamma}_0\gamma_{n-1} & -\bar{\gamma}_0\gamma_{n-2} & \cdots & -\bar{\gamma}_0\gamma_1 & -\bar{\gamma}_0\tau \\ 1-|\gamma_1|^2 & -\bar{\gamma}_1\gamma_2 & \cdots & -\bar{\gamma}_1\gamma_{n-1} & -\bar{\gamma}_1\gamma_{n-2} & \cdots & -\bar{\gamma}_1\gamma_1 & -\bar{\gamma}_1\tau \\ 0 & 1-|\gamma_2|^2 & \cdots & -\bar{\gamma}_2\gamma_{n-1} & -\bar{\gamma}_2\gamma_{n-2} & \cdots & -\bar{\gamma}_2\gamma_1 & -\bar{\gamma}_2\tau \\ \vdots & & & & & & & \\ 0 & 0 & & \cdots & & 0 & 1-|\gamma_1|^2 & -\bar{\gamma}_1\tau \end{bmatrix},$$

kao i $\gamma_0 = 1$, $\widehat{D}_{2n-2} = diag[\widehat{\delta}_0, \widehat{\delta}_1, \ldots, \widehat{\delta}_{2n-3}]$, $\widehat{\delta}_0 = 1$, $\widehat{\delta}_j = \widehat{\delta}_{j-1}\left(1 - |\widehat{\gamma}_j|^2\right)$, $j = 1,\ldots,2n-3$, $\widehat{\gamma}_j = \gamma_j$, $j = 1,\ldots,n-1$ i $\widehat{\gamma}_j = \gamma_{2n-2-j}$, $j = n,\ldots,2n-3$. Postoji nekoliko algoritama za dekompoziciju ovakvih matrica (videti [4], [3], [2]), a izračunavanje sopstvenog sistema može se izvesti veoma efikasno korišćenjem kompaktne reprezentacije HESSENBERGove matrice (videti npr. [4], [2]).

4. Poređenje metoda

Kao što smo u prethodnim poglavljima naveli, usrednjene GAUSSove kvadraturne formule definisane u radu [13] mogu se primenjivati na prostoru trigonometrijskih polinoma samo u slučajevima kada je težinska funkcija parna, dok uopštene usrednjene SZEGŐve kvadraturne formule [5] imaju širu oblast primene. Međutim, naš metod usrednjenih GAUSSovih kvadraturnih formula koristi rekurentne relacije za određivanje potrebnih ortogonalnih sistema kako bi se izbegla numerička nestabilnost koja je karakteristična za GRAM-SCHMIDTov postupak. Takođe, rekurentne relacije obezbeđuju stabilan način za izračunavanje vrednosti trigonometrijskih polinoma u odnosu na korišćenje proširenih formi.

Koristeći usrednjene GAUSSove kvadraturne formule za trigonometrijske polinome uspeli smo da postignemo mnogo veću tačnost u poređenju sa usrednjenim SZEGŐvim kvadraturama na klasi simetričnih težinskih funkcija, koju ćemo demonstrirati u narednom primeru.

Primer 4.1 ([13])**.** Posmatrajmo težinsku funkciju $w(x) = 2\sin^2\left(\frac{x}{2}\right)$ na $(-\pi,\pi)$ i integrand $f(x) = \frac{1}{2}\log(5+4\cos x)$. U tabeli 1 predstavljene su greške nastale primenom SZEGŐve $S_1^n(f)$, anti-SZEGŐve $A_1^n(f)$, uopštene usrednjene SZEGŐve kvadrature $\widehat{S}_1^{(2n-2)}(f)$, kao i GAUSSove $\widehat{G}_{\widetilde{n}+1}f$, anti-GAUSSove $\widehat{H}_{\widetilde{n}+3}f$ i usrednjene GAUSSove kvadrature $\widehat{A}_{2\widetilde{n}+4}f$, uz uslov $\widetilde{n}+1=n$. Možemo primetiti da su greške koje nastaju primenom GAUSSovih i SZEGŐvih, odnosno anti-GAUSSovih i anti-SZEGŐvih kvadratura, približne. Međutim, očigledno je da usrednjene GAUSSove kvadrature za trigonometrijske polinome daju značajno poboljšanje u odnosu na uopštene usrednjene SZEGŐve kvadrature, koje su predstavljale najbolje rezultate u radu [5]. To poboljšanje je značajnije sa porastom broja čvorova.

Tabela 1: GREŠKE U SZEGŐVOJ ($S_1^n(f)$), ANTI-SZEGŐVOJ ($A_1^n(f)$), UOPŠTENOJ USREDNjENOJ SZEGŐVOJ ($\widehat{S}_1^{(2n-2)}(f)$), GAUSSOVOJ ($\widehat{G}_{\widetilde{n}+1}f$), ANTI-GAUSSOVOJ ($\widehat{H}_{\widetilde{n}+3}f$) I USREDNjENOJ GAUSSOVOJ ($\widehat{A}_{2\widetilde{n}+4}f$) KVADRATURI ZA $w(x) = 2\sin^2\left(\frac{x}{2}\right)$, $x\in(-\pi,\pi)$, I $f(x) = \frac{1}{2}\log(5+4\cos x)$

Pravilo	$n=12$	$n=18$
$S_1^n(f)$	$-2,2\cdot10^{-5}$	$-2,3\cdot10^{-7}$
$A_1^n(f)$	$2,3\cdot10^{-5}$	$2,4\cdot10^{-7}$
$\widehat{S}_1^{(2n-2)}(f)$	$-1,5\cdot10^{-7}$	$-6,7\cdot10^{-10}$
$\widehat{G}_{\widetilde{n}+1}f$	$-1,98\cdot10^{-5}$	$-2\cdot10^{-7}$
$\widehat{H}_{\widetilde{n}+3}f$	$1,98\cdot10^{-5}$	$2\cdot10^{-7}$
$\widehat{A}_{2\widetilde{n}+4}f$	$-5,31\cdot10^{-10}$	$-8,75\cdot10^{-14}$

Literatura

[1] C. F. Gauss, "Methodus nova integralium valores per approximationem inveniendi", *Commentationes Societatis Regiae Scientarium Recentiores*, vol. 3, pp. 123-162, 1814.

[2] W. B. Gragg, "The QR algorithm for unitary Hessenberg matrices", *J. Comput. Appl. Math.*, vol. 16, pp. 1-8, 1986.

[3] W. B. Gragg and L. Reichel, "A divide and conquer method for the unitary and orthogonal eigenproblems", *Numer. Math.*, vol. 57, pp. 695-718, 1990.

[4] M. Gu, R. Guzzo, X-B. Chi and X-Q. Cao, "A stable divide and conquer algorithm for the unitary eigenproblem", *SIAM J. Matrix Anal. Appl.*, vol. 25, pp. 385-404, 2003.

[5] C. Jagels, L. Reichel and T. Tang, "Generalized averaged Szegő quadrature rules", *J. Comput. Appl. Math.*, vol. 311, pp. 645-654, 2017.

[6] S-M. Kim and L. Reichel, "Anti-Szegő quadrature rules", *Math. Comp.*, vol. 76, pp. 795-810, 2007.

[7] D. P. Laurie, "Anti-Gaussian quadrature formulas", *Math. Comp.*, vol. 65 (214), pp. 739-747, 1996.

[8] G. V. Milovanović, A. S. Cvetković and M. P. Stanić, "A special Gaussian rule for trigonometric polynomials", *Banach J. Math. Anal.*, vol. 1 (1), pp. 85-90, 2007.

[9] G. V. Milovanović, A. S. Cvetković and M. P. Stanić, "Explicit formulas for five-term recurrence coefficients of orthogonal trigonometric polynomials of semi-integer degree", *Appl. Math. Comput.*, vol. 198, pp. 559-573, 2008.

[10] G. V. Milovanović, A. S. Cvetković and M. P. Stanić, "Trigonometric orthogonal systems and quadrature formulae", *Comput. Math. Appl.*, vol. 56, 11, pp. 2915-2931, 2008.

[11] I. P. Mysovskikh, "Quadrature formulae of the highest trigonometric degree of accuracy", *Ž. Vyčisl. Mat. i Mat. Fiz.*, vol. 25 (8), pp. 1246-1252, 1985.

[12] I. P. Mysovskikh, "Algorithms to construct quadrature formulae of highest trigonometric degree of precision", *Metody Vychisl.*, vol. 16, pp. 5-16, 1991.

[13] N. Z. Petrović, M. P. Stanić and T. V. Tomović Mladenović, "Anti-Gaussian quadrature rule for trigonometric polynomials", *Filomat*, vol. 36(3), pp. 1005-1019, 2022.

[14] T. V. Tomović and M. P. Stanić, "Quadrature rules with an even number of multiple nodes and a maximal trigonometric degree of exactness", *Filomat*, vol. 20(10), pp. 2239-2255, 2015.

[15] A. H. Turetzkii, "On quadrature formulae that are exact for trigonometric polynomials", *East J. Approx.*, vol. 11, pp. 337-359, 2005.

The 10th Conference on Mathematics in Engineering: Theory and Applications
Novi Sad, December 12-14th 2025

UPOTREBA RAČUNARSKE ANIMACIJE KAO METODE OBUKE IZ OBLASTI ALGORITAMA PRETRAGE[1]

Dunja Španović [2], Daria Varga[2], Bojan Banjac[2] i Lidija Krstanović[2]

https://doi.org/10.24867/META.2025.17 Stručni članak

Sažetak. Ovaj rad prikazuje implementaciju i interaktivnu vizualizaciju pretrage mreže pomoću različitih algoritama za pronalaženje putanje od polazne do ciljne tačke. Kreirani interfejs omogućava definisanje dimenzija mreže unosom broja vrsta i kolona, određivanje pozicija prepreka, kao i izbor polazne i ciljne tačke. Nakon inicijalizacije mreže, implementirani algoritmi pronalaze putanju, pri čemu je svaki korak izvršavanja praćen vizuelnim prikazom i ispisom ključnih informacija o toku pretrage. Cilj rada je da se ilustruju razlike između algoritama pretrage uz jednostavan interfejs koji omogućava njihovu analizu na korisnički definisanim mrežama, u obrazovne i istraživačke svrhe.

AMS klasifikacija (2020): 68T20, 68U05

Ključne reči: algoritmi pretrage, korisnički interfejs, vizualizacija, pretraga u širinu, pretraga u dubinu, Dijkstrin algoritam, A*

1. Uvod

Planiranje putanje predstavlja jedan od ključnih zadataka u oblasti robotike, sistema koji se autonomno kreću, veštačke inteligencije, kao i u razvoju video igara. Njihov osnovni cilj je pronalaženje optimalnog puta između početne i ciljne tačke u zadatom okruženju koje može sadržati statične ili dinamične prepreke. U zavisnosti od konteksta primene, kriterijum optimalnosti može biti najkraće rastojanje, najmanji broj posećenih ćelija mreže, izbegavanje prepreka ili kombinacija ovih faktora.

Prema količini dostupnih informacija tokom izvršavanja, algoritmi za pretragu mogu se klasifikovati na neinformisane i informisane. Neinformisani algoritmi, kao što su pretraga u širinu (eng. *Breadth-First Search, BFS*) i pretraga u dubinu (eng. *Depth-First Search, DFS*), pretražuju mrežu sistematično, bez znanja o poziciji cilja. Nasuprot njima, informisane pretrage, kao što je A*,

[1] Ovaj rad predstavlja unapređenu i proširenu verziju funkcionalnosti razvijenih u okviru master rada „Primena modernih algoritama i metoda u sistemima autonomnih vozila“, autorke Dunje Španović pod mentorstvom vanr. prof. dr Lidije Krstanović.

[2] Departman za opšte discipline u tehnici, Fakultet tehničkih nauka, Univerzitet u Novom Sadu, e-mail: duspanovic@uns.ac.rs — dariavarga@uns.ac.rs — bojan.banjac@uns.ac.rs — lidijakrstanovic@uns.ac.rs

koriste heurističke funkcije kako bi usmerili pretragu ka cilju, sa namerom da se smanji broj posećenih ćelija mreže i ubrza proces pronalaženja putanje.

Za potrebe ovog rada, mreža se definiše kao diskretna podela dvodimenzionalnog prostora na konačan broj vrsta i kolona. Svaka ćelija mreže može se posmatrati kao čvor neusmerenog grafa sa granama jedinične težine ka ćelijama levo, desno, iznad i ispod. Putanja između polazne i ciljne tačke predstavlja niz susednih ćelija mreže, odnosno povezanih čvorova koji ne sadrže prepreke. U ovakvim grafovima, najkraća putanja je ona koja sadrži najmanji broj čvorova između polazne i ciljne tačke [1].

U cilju boljeg razumevanja i poređenja pomenutih pristupa, u ovom radu je implementiran interaktivni korisnički interfejs koji omogućava intuitivnu vizualizaciju procesa pretrage i analizu rezultata na korisnički definisanim mrežama. Na ovaj način korisnik može neposredno da prati tok pretrage, uporedi različite pristupe i uoči razlike u brzini, efikasnosti i karakteristikama svakog algoritma.

2. Implementacija

Implementacija funkcionalnosti izvedena je u programskom jeziku *Python*, uz korišćenje biblioteke *NumPy* za rad sa brojevnim strukturama podataka i *Matplotlib* za vizualizaciju i interakciju sa korisnikom [2]. Time je omogućen prikaz svakog koraka pretrage u realnom vremenu, uz prethodno podešavanje parametara mreže na kojoj se pretraga izvršava.

2.1. Korisnički interfejs

Korisnički interfejs omogućava korisniku da u tri koraka definiše sve parametre potrebne za pokretanje algoritama pretrage (vidi sliku 1). U prvom koraku definiše se veličina mreže unosom broja vrsta i kolona, nakon čega se prikazuje prazna mreža zadatih dimenzija. Zatim, naredni korak obuhvata određivanje pozicija prepreka. Selekcijom pomoću miša prohodna ćelija postaje prepreka i obrnuto, pri čemu se svaka promena istovremeno vizualizuje na mreži. U završnoj fazi biraju se polazna i ciljna tačka pretrage, uz ograničenja koja sprečavaju njihovo preklapanje i selektovanje ćelija koje su u prethodnom koraku postale prepreke. Kada su svi parametri definisani, mreža je spremna za pokretanje algoritama pretrage i uporedni prikaz njihovog izvršavanja u zadatim uslovima.

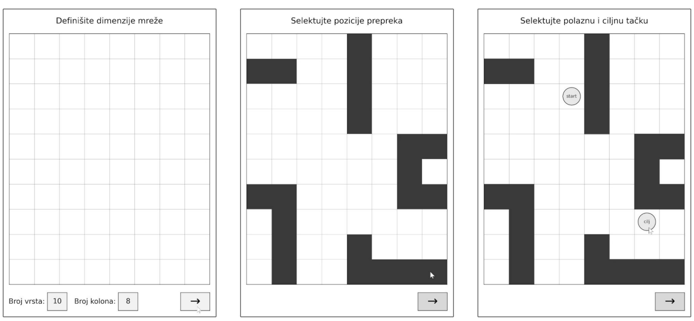

Slika 1: Kreiran korisnički interfejs za inicijalizaciju mreže

2.2. Implementirani algoritmi i heuristike za pretragu

Algoritmi pretrage implementirani su kao zasebne funkcije koje koriste istu reprezentaciju mreže i principe vizualizacije [3]. Prateće metrike, poput ukupnog broja posećenih ćelija, broja otvorenih i zatvorenih ćelija, kao i dužina pronađene putanje, omogućavaju direktno poređenje njihove efikasnosti.

Pretraga u širinu je jedan od osnovnih algoritama za traženje najkraće putanje. Ovaj algoritam istražuje ćelije mreže po nivou udaljenosti od početne pozicije, tako što prvo obrađuje sve ćelije na udaljenosti od jednog koraka, zatim dva, i tako redom [4]. U našoj implementaciji opisani postupak je realizovan pomoću strukture podataka red, koja omogućava obradu ćelija po principu *First In, First Out*. Iterativnim iscrtavanjem mreže, uz bojenje i ispis udaljenosti ćelije od polazne tačke, korisnik može da uoči osnovne osobine ovog algoritma, uključujući širenje pretrage u svim pravcima. Glavna prednost *BFS*-a jeste to što uvek pronalazi najkraći put. Međutim, s obzirom na to da tokom izvršavanja ne koristi informacije o položaju cilja, ovaj pristup može dovesti do velikog broja posećenih ćelija, čime se povećava i vreme procesiranja.

Pretraga u dubinu ima suprotan pristup u odnosu na *BFS*: ona istražuje jedno grananje što je dublje moguće pre povratka i prelaska na sledeće. Implementirani *DFS* se oslanja na strukturu podataka stek kako bi se izbegla upotreba rekurzije i samim tim potencijalno preopterećenje sistema. Pri različitim konfiguracijama mreže, korisnik može zaključiti da *DFS* ne garantuje da je pronađena putanja najkraća i da njen oblik zavisi od redosleda poteza po kojem se obrađuju susedne ćelije (u našem slučaju: gore, dole, levo, desno).

U sistemima gde se određuje putanja u težinskim grafovima sa nenegativnim težinama grana primenjuju se algoritmi koji tokom pretrage prate ukupni trošak pređenog puta $g(n)$, pri čemu n označava ćeliju koja se trenutno obrađuje [5]. Jedan od najpoznatijih među njima jeste Dijkstrin algoritam, koji predstavlja osnovu mnogih savremenih rešenja za planiranje putanje. Za razliku od *BFS*-a koji u grafu sa jednakim težinama pronalazi najkraću putanju od polazne do ciljne tačke samo na osnovu broja čvorova koji čine putanju, Dijkstrin algoritam određuje putanju pomoću prioritetnog reda tako što u svakom koraku bira čvor sa najmanjim poznatim troškom puta. Tokom izvršavanja algoritma prate se dve grupe ćelija: otvorene i zatvorene. Otvorena lista obuhvata sve trenutno dostupne kandidate za dalju ekspanziju pretrage. U njoj se nalaze ćelije koje su otkrivene i za koje je izračunat trenutni trošak puta, na osnovu čega prioritetni red određuje koja ćelija će biti izabrana za narednu obradu. Zatvorenu listu čine ćelije za koje je već potvrđeno da imaju najmanji mogući trošak u određenom trenutku izvršavanja algoritma, pa se zbog toga više ne razmatraju pri daljem širenju pretrage. U vizualizaciji implementiranoj u ovom radu otvorene ćelije prikazane su tamnosivom, dok su zatvorene obeležene svetlijom nijansom sive, čime se omogućava praćenje procesa izbora ćelija tokom pretrage.

Na mrežama gde sve grane imaju istu težinu, Dijkstrin algoritam daje iste rezultate kao *BFS*, ali uz veće vreme procesiranja usled upotrebe prioritetnog reda. Ipak, njegovo uključivanje u analizu omogućava jasnije poređenje sa A* koji predstavlja proširenje Dijkstrinog pristupa uvođenjem heuristike troška puta do cilja [6].

A* kombinuje stvarni trošak puta od polazne tačke do trenutne ćelije *g(n)* sa heuristikom troška preostalog puta do cilja *h(n)*, formirajući vrednost funkcije evaluacije *f(n)* = *g(n)* + *h(n)*, gde n označava trenutni čvor. U našoj implementaciji, heuristika se zasniva na Menhetn udaljenosti koja je pogodna u slučajevima kada se kretanje po mreži vrši u četiri smera, dok se ćelije obrađuju pomoću strukture podataka prioritetni red koji omogućava efikasan izbor ćelija sa najmanjom vrednošću funkcije evaluacije. U svakom koraku se vizualizuju obrađeni čvorovi sa istaknutim otvorenim i zatvorenim ćelijama, kao i ispisom njihove g i h vrednosti (vidi sliku 2). Na ovaj način, korisnik može da prati kako funkcija evaluacije utiče na tok pretrage i da uoči glavnu prednost A* algoritma koja podrazumeva pronalaženje najkraće putanje uz značajno manji broj obrađenih ćelija [7, 8].

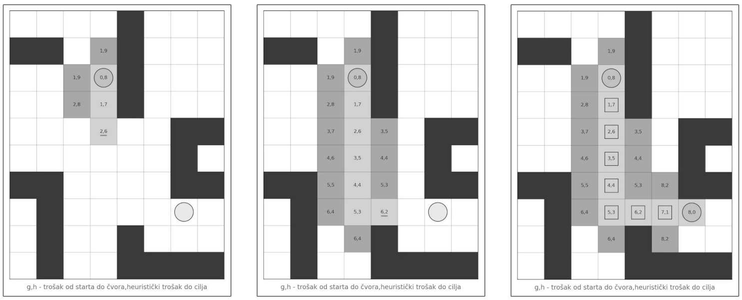

Slika 2: Prikaz nekoliko koraka pretrage pomoću A*

Da bi se olakšalo poređenje, koraci izvršavanja sva četiri algoritma vizualizovani su istovremeno, jedan pored drugog, u okviru istog prozora (vidi sliku 3). Ovakav prikaz, uz ispis ključnih metrika poput ukupnog broja posećenih ćelija, broja otvorenih i zatvorenih ćelija, kao i dužina putanje, omogućava korisniku da lakše sagleda prednosti i ograničenja sva četiri pristupa u identičnim uslovima.

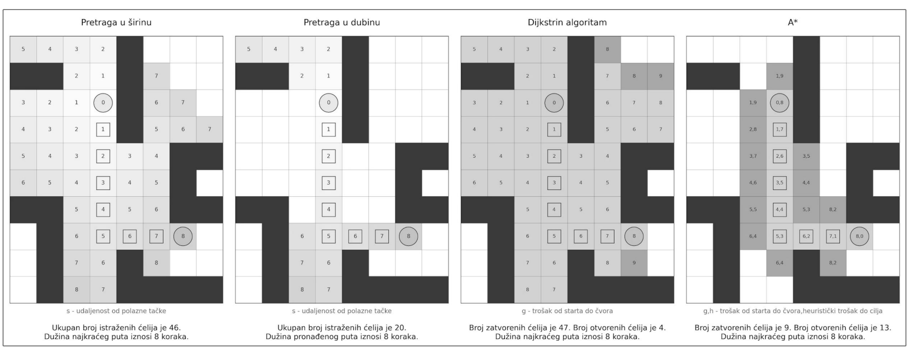

Slika 3: Uporedni prikaz rezultata pretrage pomoću *BFS*-a, *DFS*-a, Dijkstrinog algoritma i A*

3. Zaključak

U radu je realizovan uporedni prikaz pretrage mreže u širinu, u dubinu, Dijkstrinog algoritma i A*. Implementirane funkcionalnosti obuhvataju korisnički interfejs za definisanje dimenzija mreže, prepreka, kao i polazne i ciljne tačke, uz prikaz toka pretrage sa odgovarajućim metrikama. Interaktivna priroda kreiranog rešenja čini ga pogodnim za obrazovne svrhe, jer korisniku pruža mogućnost da inicijalizuje okruženje u kojem se pretraga odvija i da istovremeno prati svaki korak izvršavanja sva četiri algoritma. Moguća unapređenja uključuju nove pristupe za traženje putanje, primenu dodatnih heuristika, omogućavanje dijagonalnih poteza prilikom obilaska mreže i uvođenje dinamičnih prepreka.

Literatura

[1] Ivica Bošnjak, Dragan Mašulović, Vojislav Petrović i Ratko Tošić, *Zbirka zadataka iz teorije grafova*, PMF, Departman za matematiku i informatiku, Novi Sad, 2005.

[2] Matplotlib Development Team, *Event handling and picking*, `https://matplotlib.org/stable/users/explain/figure/event_handling.html`, 2025.

[3] Silvester Dian Handy Permana, Ketut Bayu Yogha Bintoro, Budi Arifitama, and Ade Syahputra, *Comparative Analysis of Pathfinding Algorithms A*, Dijkstra, and BFS on Maze Runner Game*, IJISTECH (International Journal of Information System & Technology), vol. 1, no. 2, pp. 1, 2018. DOI: 10.30645/ijistech.v1i2.7

[4] Thomas H. Cormen, Charles E. Leiserson, Ronald L. Rivest, and Clifford Stein, *Introduction to Algorithms, Fourth Edition*, The MIT Press, 2022.

[5] Steven S. Skiena, *The Algorithm Design Manual, Third Edition*, Springer, 2020.

[6] Sharmad Rajnish Lawande, Graceline Jasmine, Jani Anbarasi, and Lila Iznita Izhar, *A Systematic Review and Analysis of Intelligence-Based Pathfinding Algorithms in the Field of Video Games*, Applied Sciences, vol. 12, no. 11, pp. 5499, 2022. DOI: 10.3390/app12115499

[7] Peter E. Hart, Nils J. Nilsson, and Bertram Raphael, *A Formal Basis for the Heuristic Determination of Minimum Cost Paths*, IEEE Transactions on Systems Science and Cybernetics, vol. 4, no. 2, pp. 100-107, 1968. DOI: 10.1109/TSSC.1968.300136

[8] Stuart Russell and Peter Norvig, *Artificial Intelligence: A Modern Approach, Third Edition*, Pearson, 2010.

The 10th Conference on Mathematics in Engineering: Theory and Applications
Novi Sad, December 12-14th 2025

Kreissova konstanta za Mittag-Lefflerove funkcije

Vladimir Kostić [1] **i Ilja Uzelac Bujišić** [2]

https://doi.org/10.24867/META.2025.18 Pregledni članak

Sažetak

U ovom radu proučavamo prolazno vezu između rešenja sistema frakcionih diferencijalnih jednačina i Kreissove matrične teoreme. Iako se asimptotska stabilnost matrice A određuje položajem njenog spektra, rešenja mogu pokazivati značajno tranzitivno ponašanje, analogno klasičnom fenomenu opisanom Kreissovim teoremom. Mittag - Lefflerove funkcije $E_{\alpha,\beta}(t)$ predstavljaju generalni oblik rešenja sistema frakcionih diferencijalnih jednačina. Ovaj pregledni rad daje kratak pregled navedene teme u slučaju obi;nih diferencijalnih jednačina $\alpha = \beta = 1$ i uvodi hipotezu o gornjoj granici norme $E_{\alpha,1}(At^{\alpha})$ putem frakcionog pseudospektra za slučaj $\alpha < \beta = 1$.

AMS klasifikacija (2020): 15A60, 37N35

Ključne reči: Frakcione diferencijalne jednačine, Kreissova matrična teorema, Mittag - Lefflerove funkcije.

1 Uvod

Ovaj rad se bavi pregledom Kreissove matrične teoreme te njenim proširenjem na novu klasu funkcija - Mittag Lefflerove funkcije. Prva Kreissova matrična teoremu je dokazao Heinz-Otto Kreiss 1962. te tako postavio temelje za ograničavanje norme stepena matrica. Ona je rezultat višedecenijskog proučavanja stabilnosti linearnih operatora i diskretnih semigrupa. Pri posmatranju asimptotski stabilnih linearnih sistema (onih u kojima rešenja teže nuli kako vreme t teži beskonačnosti), primećeno je da njihovo tranzientno ponašanje (recimo za neki konačni interval vremena $t \in [A, B]$) može biti takvo da norma rešenja značajno raste. Kreissova matrična teorema i njena eksplicitna forma, vid. [1], daje ograničenje na ponašanje sistema u tranzientnoj fazi. Pri tome se razlikuju dva glavna slučaja - matrični stepenovi i matrična eksponencijalna funkcija.

Novi oblik Kreissove matrične teoreme koji je glavna tema ovog rada odnosi se primene teoreme na kompleksniji skup funkcija, konkretno Mittag - Lefflerove funkcije [2]. Njihova praktična važnost ogleda se u tome što one predstavljaju rešenje Frakcionog sistema diferencijalnih jednačina [3]. koji

[1]IIT Genova, e-mail: vladimir.slk@gmail.com
[2]Matematički Institut SANU, e-mail: bujisiciljamat@gmail.com

je privukao veliku pažnju tokom poslednjih godina zbog brojnih uspešnih primena kada je u opisivanju dinamike fizičkih procesa koji ispoljavaju ne-lokalne osobine, npr. kretanje objekta u viskoznom medijumu. Ovaj rad uvodi generalizaciju Kreissove konstante za ocenu tranzicijskog rasta linearnih sistema frakcionih diferencijalnih jednačina izraženog putem Mitteg-Lefflerovih funkcija.

2 Frakcioni Diferencijalni Operatori

Definicija 2.1. **Mittag–Lefflerova funkcija** $E_\alpha(z)$, smatra se generalizacijom eksponencijalne funkcije za jedan fiksan realan parametar $\alpha > 0$ definisana konvergentnim redom

$$E_\alpha(z) = \sum_{k=0}^{\infty} \frac{z^k}{\Gamma(\alpha k + 1)}.$$

Iz navedene formule, vidljivo je da važi $E_1(z) = e^z$.

Definicija 2.2. U generalnijem dvoparametarskom obliku za $\alpha, \beta > 0$ definisana je sa:

$$E_{\alpha,\beta}(z) = \sum_{k=0}^{\infty} \frac{z^k}{\Gamma(\alpha k + \beta)}$$

Definicija 2.3. **Riemann - Liouvilleov** frakcioni integralni operator se definiše kao :

$$J^\alpha f(t) = \frac{1}{\Gamma(\alpha)} \int_0^t f(\tau)(t-\tau)^{\alpha-1}\, d\tau, \alpha > 0, \tau > 0$$

Kombinacijom ove formule i celobrojnih izvoda, može se definisati frakcioni izvod reda $\alpha > 0$

Definicija 2.4. **Kaputov (Caputo) frakcioni izvod** funkcije $f(t)$:

$$\frac{d^\alpha f(t)}{dt^\alpha} = D^\alpha f(t) = J^{m-\alpha} D^m f(t) = \frac{1}{\Gamma(m-\alpha)} \int_0^t \frac{f^{(m)}(\tau)}{(t-\tau)^{\alpha-m+1}}\, d\tau,\ m-1 < \alpha \leq m,$$

gde $\Gamma(\cdot)$ označava Gama funkciju.

Ukoliko je α prirodan broj, navedena definicija se svodi na standardan izvod.

Analogno celobrojnim izvodima, i u frakcionom slučaju mogu se definisani dinamički sistemi koristeći frakcione diferencijalne jednačine.

Definicija 2.5. Linearni frakcioni dinamički sistem $\mathbf{x}(t)$ gde t označava vreme, $\mathbf{x}$ je vektor stanja, a $A \in \mathbb{C}^{n\times n}$ je matrica sistema definisan je sa:

$$\frac{d^\alpha \mathbf{x}(t)}{dt^\alpha} = A\mathbf{x}(t), \mathbf{x}(0) = \mathbf{x}_0, x^{(1)}(0) = x_0^1, ..., x^{(n-1)}(0) = x_0^{n-1}$$

U navedenom obliku vektor $\alpha = [\alpha_1, \alpha_2, \ldots, \alpha_n]^T$ označava redove frakcionog izvoda, a diferencijalni operator

$$\frac{d^\alpha}{dt^\alpha} = \left[\frac{d^{\alpha_1}}{dt^{\alpha_1}}, \frac{d^{\alpha_2}}{dt^{\alpha_2}}, \ldots, \frac{d^{\alpha_n}}{dt^{\alpha_n}}\right]^T$$

je definisan Kaputovim frakcionim izvodima $\frac{d^{\alpha_k}}{dt^{\alpha_k}}$ reda $\alpha_k > 0$, za $k = 1, 2, \ldots, n$.

Identično kao i u standardnim diferencijalnim jednačinama, i u ovom slučaju istraživanje stabilnosti ovakvih dinamičkih sistema od izuzetne je važnosti u teoriji kontrole. Glavna pitanja se odnose na potrebne i dovoljne uslove za stabilnost ovakvih sistema [4].

U specifičnom slučaju u kojem su svi redovi frakcionih izvoda jednaki, tj:

$$\alpha_1 = \alpha_2 = ... = \alpha_k = \alpha$$

i inicijalni uslovi :

$$x^{(1)}(0) = x^{(2)}(0) = ... = x^{(n-1)}(0) = 0$$

važi da je rešenje ovog sistema :

$$x(t) = E_\alpha(At^\alpha) = \sum_{k=0}^{\infty} \frac{(At^\alpha)^k}{\Gamma(\alpha k + 1)}$$

gde je $E_\alpha(At)$ Mittag - Leflerova funkcija.

Neka je $A \in \mathbb{C}^{n\times n}$ kvadratna matrica i neka $\|\cdot\|$ označava normu nad matricama indukovanu kvadratnom normom na $\mathbb{C}^n$. Onda su definisane dve relevantne Kreissove konstane.Prva Kreissova konstanta se odnosi na diskretno stepenovanje matrica i definisana je u odnosu na jedinični kompleksni krug.

Definicija 2.6. Diskretna Kreissova konstanta $\mathcal{K}(A)$ definisana je sa:

$$\mathcal{K}_d(A) = \sup_{|z|>1} (\,|z| - 1\,)\,\|(zI - A)^{-1}\|.$$

Dok je Kreissova konstanta vezana za eksponencijalnu funkciju primenjenu na matrici je definisana sa:

$$\mathcal{K}_c(A) = sup_{Re(z)>0} Re(z)\|(zI - A)^{-1}\|$$

U sledećoj teoremi navedena je Kreissova teorema za eksponencijalni slučaj.

Teorema 2.7. *Neka je $A \in \mathbb{C}^{n\times n}$ matrica čiji takva da je njen celi spektar $\sigma(A)$ u levoj kompleksnoj poluravni onda važi:*

$$\mathcal{K}_c(A) \leq \sup_{t\geq 0} \|e^{tA}\| \leq en\mathcal{K}_c(A)$$

gde t označava neprekidno vreme.

Važnost ovih teorema je ta što one daju konkretno gornje ograničenje na normu matrice u tranzijentnom stanju dinamičkog sistema. Dakle, ako je i poznato da dinamički sistem konvergira nuli asimptotski, često nije potpuno jasno kako se sistem ponaša u tranzijentnoj fazi sistema tj za $t \in [A, B]$ za neke konačne A, B. Ova teorema jasno daje ograničenje norme u tim slučajevima jer navedeno ograničenje zavisi samo od $\mathcal{K}$ i od dimenzije matrice n, a ne od vremena t ili stepena k.

3 Generalizacija Kreissove Matrične teoreme

Logično pitanje je može li se navedena teorema primenjivati na široj klasi funkcija, osim samo stepenovanja i eksponencijalne funkcije primenjene na matricu A. Kako bi se do tog pitanja došlo, neophodno je prvo ustanoviti uslove pod kojima je navedeni sistem stabilan. U [3] je naveden uslov za asimptotsku stabilnost ovakvih sistema u zavisnosti od spektra matrice A i uvedeno je uopštenje pseudospektra za linearne frakcione dinamičke sisteme.

Teorema 3.1. *Frakcioni dinamički sistem definisan matricom A i stepenima izvoda $\alpha_1 = \alpha_2 = ... = \alpha_n = \alpha$ je stabilan ako i samo ako je $|arg(\lambda)| > \frac{\alpha\pi}{2}$ za svako $\lambda \in \sigma(A)$ tj ako je :*

$$\Lambda(A) \subseteq \Omega_\alpha := \{z \in \mathbb{C} : \frac{\alpha\pi}{2} < arg(z) < 2\pi - \frac{\alpha\pi}{2}\}$$

Definicija 3.2. Matrica koja ispunjava navedeni uslov stabilnosti se naziva α-*frakciono stabilna* matrica.

Za ovakvu matricu se može definisati α - pseudospektar, slično klasičnoj definiciji pseudospektra.

Definicija 3.3. Za matricu $A \in \mathbb{C}^{n\times n}$ α - pseudospektar je definisan sa :

$$\Lambda_{\alpha,\epsilon}(A) := \{z \in \mathbb{C} : \|[R_A^\alpha(z)]^{-1}\|^{-1} \leq \epsilon\}$$

gde je $R_A^\alpha(z)$ rezolventa stepena α:

$$R_A^\alpha(z) = \|(z^\alpha - A)^{-1}\|.$$

U slučaju eksponencijalne funkcije, t.j. $\alpha = 1$, Kreissova konstanta za eksponencijalnu funkciju može se izraziti preko *spektralne abscise* matrice A, $a_\epsilon(A)$:

$$a_\epsilon(A) := max\{Re(\lambda) \ : \lambda \in \Lambda_\epsilon(A)\}$$

gde $\Lambda_\epsilon(A)$ predstavlja ϵ - *pseudospektar* matrice A:

$$\Lambda_\epsilon(A) = \{z \in \mathbb{C} : \|(z - A)^{-1}\| < \epsilon\}$$

Onda se Kreissova konstanta $\mathcal{K}_c(A)$ može izraziti kao :

$$\mathcal{K}_c(A) = sup_{\epsilon>0}\frac{a_\epsilon(A)}{\epsilon}$$

Ovaj oblik Kreissove konstante direktno povezuje pseudospektar matrice sa njenim tranzitivnim ponašanjem. Dokaz teoreme 2.7. detaljno je prikazan u poglavlju 18 [5] i svodi se na dva glavna elementa - Spijkerovu teoremu i integraciju po konturi koja ograničava spektar matrice. Pri tome kontura mora ograničavati spektar matrice $\Lambda(A)$ za koji se pretpostavlja da je u levoj kompleksnoj poluravni.

Smatramo da se ovaj dokaz može generalizovati na širu klasu Mittag-Leflerovih funkcija. Pri stepenovanju sa α granica skupa koji ograničava pseudospektar prelazi u $\partial\Omega_\alpha$ koja se sastoji od dve linije u desnoj poluravni - jedna predstavlja $arg(z) = \frac{\alpha\pi}{2}$,a druga $-\frac{\alpha\pi}{2}$.

Ukoliko je $x(t)$ rešenje sistema frakcionih diferencijalnih jednačina u slučaju kad je $\alpha_1 = \alpha_2 = ... = \alpha_n = \alpha$, A matrica koja zadaje taj sistem, onda važi nejednakost predstavljena sledećom teoremom.

Hipoteza 3.1. *Ukoliko je A matrica takva da ispunjava uslov Teoreme 3.1. za parametar α, i ako važi $Re(z) < 0$ za sve $z \in \sigma(A)$ onda postoji konstanta $c > 0$ koja zavisi od n i α takoda važi:*

$$\|x(t)\| \leq c\,\mathcal{K}_f^\alpha(A) \tag{3.1}$$

gde je

$$\mathcal{K}_f^\alpha(A) := \sup_{\epsilon>0} \frac{a_\epsilon^\alpha}{\epsilon}$$

za

$$a_\epsilon^\alpha := max\{Re(\lambda^\alpha)\ \ : \lambda \in \Lambda_{\alpha,\epsilon}(A)\}$$

Prvo, primetimo da uslov frakcione stabilnosti garantuje da je $\mathcal{K}_f^\alpha < \infty$, kao i da je rešenje $x(t)$ ograničeno za $t > 0$. Dakle, pitanje je zapravo koliko $c > 0$ može biti mala. U slučaju $\alpha = 1$, znamo da je $c = en$.

Ideja vodilja u pravcu generalizacije dokaza optimalne konstante je sledeća jednakost putem Laplasove transformacije koja važi za sektorijalne operatore [4] dobijena putem Laplasove transformacije:

$$E_\alpha(t^\alpha A) = \frac{1}{2\pi i}\int_\gamma e^{st}s^{\alpha-1}(s^\alpha I - A)^{-1}ds, \tag{3.2}$$

gde je γ Bromwich-ova linija s: $Re(s) = 1/t$ za neko $t > 0$, a u $s^{\alpha-1}$ koristimo glavnu granu u $\mathbb{C}$.

Primetimo da je slučaju $\alpha = 1$ gornja karakterizacije postaje $e(tA) = \frac{1}{2\pi i}\int_\gamma e^{st}(sI-A)^{-1}ds$ klasični razvoj matrične eksponencijalne funkcije $e(tA) = \frac{1}{2\pi i}\int_\gamma e^{st}(sI - A)^{-1}ds$.

Dalje, (3.2) je ekvivalentna sledećem integralu

$$E_\alpha(t^\alpha A) = \frac{1}{2\pi i\alpha}\int_\gamma e^{t\,z^{1/\alpha}}(zI - A)^{-1}dz, \tag{3.3}$$

gde je sada γ z-slika Bromwich-ove konture preslikavanjem $s \mapsto s^{\alpha} = z$, i za $z^{1/\alpha}$ koristimo glavnu granu u $\mathbb{C}$.

Koristeći prethodne karakterizacije zajedno da Spajkerovom teoremom i definicijom frakcione Krajsove konstante, Ootvoren problem je pronaći minimalnu konstantu $c > 0$ koristeći prethodne karakterizacije zajedno da Spajkerovom teoremom i definicijom frakcione Krajsove konstante, tako da (3.1) važi..

Literatura

[1] S. Raouafi, "A generalization of the Kreiss Matrix Theorem," *Linear Algebra and its Applications*, vol. 549, pp. 86–99, 2018.

[2] H. J. Haubold, A. M. Mathai, and R. K. Saxena, "Mittag-Leffler functions and their applications," *Journal of Applied Mathematics*, vol. 2011, no. 1, pp. 298628, 2011.

[3] E. Šanca, V. R. Kostić and Lj. Cvetković, "Fractional pseudospectra and their localizations," *Linear Algebra and its Applications*, vol. 559, pp. 244–269, 2018.

[4] Z. M. Odibat, "Analytic study on linear systems of fractional differential equations," *Computers & Mathematics with Applications*, vol. 59, no. 3, pp. 1171–1183, 2010.

[5] L. N. Trefethen, "Pseudospectra of matrices," *Numerical Analysis*, vol. 91, pp. 234–266, 1991.

The 10th Conference on Mathematics in Engineering: Theory and Applications
Novi Sad, December 12-14th 2025

META-ANALYSIS OF IMMUNOTHERAPY OUTCOMES IN METASTATIC MELANOMA

Katarina Vidojević[1], Jovana Dedeić[2], Srđan Milićević[3], Jelena Ivetić[4], and Marija Delić[5]

https://doi.org/10.24867/META.2025.19 Article type: Review paper

Abstract. Meta-analytic methods are essential for quantitative evidence synthesis, offering a statistical framework for model comparison and heterogeneity assessment. This paper revisits our previous work through a concise methodological review and model-comparison meta-analysis, illustrating adaptive model selection for binary outcomes. Thirteen studies (>6,000 patients) comparing monotherapy and combination regimens in metastatic melanoma immunotherapy were analyzed. Binary outcomes (benefit and risk rates) were pooled using fixed-effects (FEM), random-effects (REM), and generalized linear mixed models (GLMM), depending on heterogeneity. The results highlight how model choice influences pooled estimates and inference reliability, underscoring the importance of flexible statistical modeling in complex datasets.

AMS Mathematics Subject Classification (2020): 62P10, 62F15.

Key words and phrases: meta-analysis; FEM; REM; GLMM; immune checkpoint inhibitors (ICIs); melanoma; benefits; adverse events; risks.

1. Introduction

Meta-analysis is a key statistical framework for quantitative synthesis in medical and technical sciences, particularly valuable in studies of rare conditions with limited statistical power. Beyond summarizing results, it enables formal model comparison and heterogeneity assessment through likelihood-based methods. In modern oncology, where immune checkpoint inhibitors yield complex and variable outcomes, such modeling ensures reliable inference. We present a compact model-comparison meta-analysis that adaptively selects among FEM, REM, and GLMM according to data variability. The analysis includes 13 studies on metastatic melanoma immunotherapy, comprising 22

[1]Department of Fundamental Sciences, Faculty of Technical Sciences, University of Novi Sad, e-mail: vidojevic9@uns.ac.rs
[2]Department of Fundamental Sciences, Faculty of Technical Sciences, University of Novi Sad, e-mail: radenovicj@uns.ac.rs
[3]Department of Fundamental Sciences, Faculty of Technical Sciences, University of Novi Sad, e-mail: srdjan88@uns.ac.rs
[4]Department of Fundamental Sciences, Faculty of Technical Sciences, University of Novi Sad, e-mail: jelenaivetic@uns.ac.rs
[5]Department of Fundamental Sciences, Faculty of Technical Sciences, University of Novi Sad, e-mail: marijadelic@uns.ac.rs

study arms and over 6,000 patients ([4]-[16]) and summarizes our previous work published in [1, 2, 3].

2. Methods

2.1. Statistical models

For binary outcomes we applied three modeling strategies depending on heterogeneity (Cochran's Q, I^2): (i) FEM when $I^2 < 25\%$, (ii) REM for moderate heterogeneity, and (iii) GLMM with logit link for extreme heterogeneity ($I^2 \geq 90\%$). The GLMM was fitted on logit-transformed proportions with a random intercept per study arm; inverse-logit transformations produced pooled proportions and confidence intervals (CIs). Group comparisons used two-proportion Z-tests on pooled estimates when appropriate.

2.2. Quantifying Heterogeneity

Heterogeneity across studies was evaluated using Cochran's Q statistic and the I^2 index. Cochran's Q tests whether observed variability among study outcomes exceeds that expected by chance alone: $Q = \sum_{i=1}^{k} w_i(p_i - \bar{p})^2$, where k denotes the number of study arms, p_i represents the observed event proportion in the i-th arm study, $\bar{p}$ is weighted pooled estimate of the event proportion and $w_i = \frac{1}{\sigma_i^2}$ is the inverse-variance weight, with $\sigma_i^2 = \frac{p_i(1-p_i)}{n_i}$, where n_i is the study sample size.

To interpret heterogeneity in percentage form, the I^2 statistic was calculated as:

$$I^2 = \max\left(0, \frac{Q-(k-1)}{Q}\right) \times 100\%.$$

The I^2 value represents the proportion of total variation in observed outcomes attributable to real differences between studies rather than random sampling error. In accordance with Cochrane guidelines, heterogeneity levels were classified as low ($I^2 < 25\%$), moderate ($25\% \leq I^2 < 90\%$), and substantial ($I^2 \geq 90\%$).

These thresholds determined the choice among three modeling frameworks: FEM, REM, and GLMM.

2.3. Fixed-Effects Model

Under the FEM, it is assumed that all studies estimate a common underlying true effect, and that any observed variation arises purely from within-study error. The pooled proportion estimate under the FEM is given by:

$$\bar{p}_{FEM} = \frac{\sum_{i=1}^{k} w_i p_i}{\sum_{i=1}^{k} w_i},$$

where the weights w_i correspond to the inverse of the within-study variance. The variance and standard error of the pooled estimate are:

$$\mathrm{Var}(\bar{p}_{FEM}) = \frac{1}{\sum_{i=1}^{k} w_i}, \qquad SE_{FEM} = \sqrt{\mathrm{Var}(\bar{p}_{FEM})}.$$

The corresponding 95% confidence interval is expressed as:

$$(\bar{p}_{FEM} - 1.96 \cdot SE_{FEM},\ \bar{p}_{FEM} + 1.96 \cdot SE_{FEM})\,.$$

This model was applied to subgroups exhibiting low between-study heterogeneity ($I^2 < 25\%$), yielding narrow confidence intervals that reflect the homogeneity of treatment effects.

2.4. Random-Effects Model

When moderate heterogeneity was detected ($25\% \leq I^2 < 90\%$), the REM was employed to account for both within- and between-study variability. Between-study variance (τ^2) was estimated as:

$$\tau^2 = \frac{Q - (k-1)}{C}, \quad \text{where} \quad C = \sum_{i=1}^{k} w_i - \frac{\left(\sum_{i=1}^{k} w_i^2\right)}{\sum_{i=1}^{k} w_i}.$$

The adjusted weights under the REM were computed as $w_i^* = \frac{1}{\sigma_i^2 + \tau^2}$. The pooled estimate under the REM is given by:

$$\bar{p}_{REM} = \frac{\sum_{i=1}^{k} w_i^* p_i}{\sum_{i=1}^{k} w_i^*}.$$

This approach provided wider confidence intervals than FEM, capturing uncertainty arising from cross-study differences such as patient demographics, dosing schedules, and study design variability.

2.5. Generalized Linear Mixed Model

For datasets characterized by extreme heterogeneity ($I^2 \geq 90\%$), a GLMM was adopted. The GLMM extends traditional meta-analytic models by incorporating random effects directly into the link function. Event proportions were transformed via the logit function $y_i = \ln\left(\frac{p_i}{1-p_i}\right)$, and modeled as:

$$y_i = \beta_0 + u_i,$$

where β_0 represents the fixed intercept and $u_i \sim \mathcal{N}(0, \tau^2)$ denotes a random intercept capturing between-study variability. The fitted estimates were transformed back to the proportion scale using the inverse-logit function.

The GLMM provided the most flexible framework, yielding stable and interpretable results even under non-normal or highly dispersed data.

3. Results

Across all datasets, treatment outcomes were reported in accordance with the RECIST criteria, classifying therapeutic responses into complete response (CR), partial response (PR), overall response (OR) and stable disease (SD). In addition to survival outcomes, the analysis evaluated the incidence of irAEs, including pneumonitis, colitis, diarrhea, and thyroid-related disorders (hyperthyroidism and hypothyroidism). The dual focus on both treatment efficacy and safety allowed for an integrated risk-benefit assessment of immunotherapy regimens.

The pooled incidence rates of irAEs for monotherapy and combination therapy are summarized in Table 1. The results indicate a markedly higher frequency of adverse events in the combination therapy group, where 93.2% of patients experienced at least one irAE compared to 81.9% in the monotherapy group. For instance, pneumonitis occurred in approximately 5.55% of patients receiving combination therapy versus 1.95% for monotherapy; hypothyroidism was reported in 18.78% versus 10.41%, and hyperthyroidism in 14.09% versus 3.39%.

Table 1: Pooled prevalence estimates of adverse events by therapy group, with heterogeneity indicators.

Adverse event	**Therapy type**	**Study arms**	**Patients**	I^2 **(%)**†	**Point estimate**	**95% CI**
At least one AE*	M	10	3222	99.53^g	0.8194	(0.6562, 0.9152)
	C	6	1801	61.50^r	0.9322	(0.9111, 0.9534)
Pneumonitis*	M	10	2650	31.99^r	0.0195	(0.0126, 0.0265)
	C	6	1801	70.88^r	0.0555	(0.0335, 0.0775)
Hypothyroidism*	M	10	2638	85.43^r	0.1041	(0.0729, 0.1353)
	C	6	1801	47.72^r	0.1878	(0.1597, 0.2160)
Hyperthyroidism*	M	7	2244	92.31^g	0.0339	(0.0173, 0.0654)
	C	5	1707	81.59^r	0.1409	(0.0983, 0.1836)
Colitis*	M	10	2558	80.44^r	0.0300	(0.0161, 0.0439)
	C	6	1801	81.22^r	0.0753	(0.0450, 0.1056)
Diarrhea*	M	9	2567	90.14^g	0.1845	(0.1367, 0.2443)
	C	6	1801	88.67^r	0.3457	(0.2734, 0.4180)
Increased AST*	M	3	1231	0.00^f	0.0670	(0.0531, 0.0810)
	C	5	1487	89.74^r	0.1732	(0.1078, 0.2385)
Increased ALT*	M	3	1231	0.00^f	0.0738	(0.0592, 0.0884)
	C	5	1487	88.64^r	0.1881	(0.1226, 0.2536)

Table 2: Comparison of clinical benefit outcomes between monotherapy and combination therapy, with pooled prevalence and heterogeneity indicators.

Outcome	**Therapy type**	**Study arms**	**Patients**	I^2 **(%)**†	**Point estimate**	**95% CI**
CR*	M	7	2458	91.46^g	0.1251	(0.0858, 0.1791)
	C	5	885	59.29^r	0.1749	(0.1348, 0.2151)
PR*	M	8	2504	79.49^r	0.2029	(0.1663, 0.2394)
	C	5	885	0.00^f	0.3448	(0.3135, 0.3761)
OR*	M	8	2504	94.31^g	0.3156	(0.2391, 0.4037)
	C	5	885	64.94^r	0.5224	(0.4652, 0.5796)
SD*	M	8	2504	91.73^g	0.1676	(0.1257, 0.2199)
	C	5	885	78.09^r	0.1007	(0.0589, 0.1425)

M - monotherapy; C - combination therapy

† Superscript indicates model type used: ^{f} FEM, ^{r} REM, ^{g} GLMM.

* Statistically significant difference between mono and combination groups at $p < 0.001$.

The pooled therapeutic response outcomes, including CR, PR, OR, and SD rates for both therapy groups are presented in Table 2. The combination therapy demonstrated a complete response rate of approximately 17.49%, compared to 12.51% for monotherapy. The partial response rate was 34.48% for the combination group versus 20.29% for monotherapy, resulting in an overall response rate of 52.24% versus 31.56%. Conversely, the rate of stable disease was slightly higher with monotherapy (16.76%), suggesting that tumor regression was less frequent compared to the combination approach. These results highlight that combination immunotherapy yields substantially improved clinical efficacy but at the cost of an increased incidence of adverse events.

4. Conclusion

The results confirm that combination immune checkpoint blockade offers greater benefit than monotherapy but with higher immune-related toxicity, requiring careful monitoring and individualized treatment. Methodologically, integrating FEM, REM, and GLMM highlights the need to account for heterogeneity for accurate effect estimation. Flexible models like GLMM better capture biological variability and support more precise therapeutic decisions.

Acknowledgement

This research was supported by the Science Fund of the Republic of Serbia, GRANT No. 9393, “Optimization and Prediction in Therapy Treatments of Cancer – OPTIC”, and by the Department of Fundamental Sciences, Faculty of Technical Sciences, University of Novi Sad, within the framework of Project “Socio-technological aspects of improving the teaching process in the English language in fundamental disciplines”.

References

[1] J. Ivetić, J. Dedeić, S. Milićević, K. Vidojević, and M. Delić, ”Comparative Meta-Analysis of Survival, Risk, and Treatment Efficacy in Immunotherapy for Metastatic Melanoma Using Random-, Fixed-, and Mixed-Effects Models”, *Journal of Clinical Medicine*, 2025.

[2] M. Delić, S. Milićević, K. Vidojević, J. Dedeić, and J. Ivetić, ”Meta-analysis of risks and benefits in immunotherapy treatment of metastatic melanoma”, in *The Book of Abstracts from RAP 2025 Conference*, Heraklion, Crete, Greece, May 2025.

[3] S. Milićević, J. Dedeić, K. Vidojević, J. Ivetić, and M. Delić, ”Model-based meta-analysis of adverse events in metastatic melanoma immunotherapy: The importance of quantifying heterogeneity”, in *Book of Abstracts of RAD 2025 Conference*, Herceg Novi, Montenegro, June 2025.

[4] J. D. Wolchok, V. Chiarion-Sileni, R. Gonzalez, J.J. Grob, P. Rutkowski, et al., ”Long-Term Outcomes With Nivolumab Plus Ipilimumab or Nivolumab Alone Versus Ipilimumab in Patients With Advanced Melanoma”, *Journal of Clinical Oncology*, 2022.

[5] C. Robert, M.S. Carlino, C. McNeil, A. Ribas, J.J. Grob, et al., ”Seven-Year Follow-Up of the Phase III KEYNOTE-006 Study: Pembrolizumab Versus Ipilimumab in Advanced Melanoma”, *Journal of Clinical Oncology*, 2023.

[6] O. Hamid, I. Puzanov, R. Dummer, J. Schachter, A. Daud, et al., ”Final analysis of a randomised trial comparing pembrolizumab versus investigator-choice chemotherapy for ipilimumab-refractory advanced melanoma”, *European Journal of Cancer*, 2017.

[7] N. Hribernik, M. Boc, J. Ocvirk, J. Knez-Arbeiter, T. Mesti, et al., ”Retrospective analysis of treatment-naive Slovenian patients with metastatic melanoma treated with pembrolizumab—real-world experience.”, *Radiology and Oncology*, 2020.

[8] O. Hamid, C. Robert, A. Daud, F. S. Hodi, W. J. Hwu, et al., ”Five-year survival outcomes for patients with advanced melanoma treated with pembrolizumab in KEYNOTE-001”, *Annals of Oncology*, 2019.

[9] F. S. Hodi, J. Chesney, A. C. Pavlick, C. Robert, K. F. Grossman, et al., ”Combined nivolumab and ipilimumab versus ipilimumab alone in patients with advanced melanoma: 2-year overall survival outcomes in a multicentre, randomised, controlled, phase 2 trial”, *The Lancet Oncology*, 2016.

[10] N. Hribernik, D. T. Huff, A. Studen, K. Zevnik, Ž. Klaneček, et al., ”Quantitative imaging biomarkers of immune-related adverse events in immune-checkpoint blockade-treated metastatic melanoma patients: a pilot study”, *European Journal of Nuclear Medicine and Molecular Imaging*, 2022.

[11] N. Hribernik, K. Strasek, D. T. Huff, A. Studen, K. Zevnik, et al., ”Role of quantitative imaging biomarkers in an early FDG-PET/CT for detection of immune-related adverse events in melanoma patients: a prospective study”, *Radiology and Oncology*, 2024.

[12] J. Larkin, D. Minor, S. D’Angelo, B. Neyns, M. Smylie, et al., ”Overall Survival in Patients With Advanced Melanoma Who Received Nivolumab Versus Investigator’s Choice Chemotherapy in CheckMate 037: A Randomized, Controlled, Open-Label Phase III Trial”, *Journal of Clinical Oncology*, 2017.

[13] C. Lebbe, N. Meyer, L. Mortier, I. Marquez-Rodas, C. Robert, et al., ”Evaluation of Two Dosing Regimens for Nivolumab in Combination With Ipilimumab in Patients With Advanced Melanoma: Results From the Phase IIIb/IV CheckMate 511 Trial”, *Journal of Clinical Oncology*, 2019.

[14] C. Robert, G. V. Long, B. Brady, C. Dutriaux, A. M. Di Giacomo, et al., "Five-Year Outcomes With Nivolumab in Patients With Wild-Type BRAF Advanced Melanoma", *Journal of Clinical Oncology*, 2020.

[15] H. A. Tawbi, P. A. Forsyth, S. F. Hodi, A. P. Algazi, O. Hamid, et al., ”Long-term outcomes of patients with active melanoma brain metastases treated with combination nivolumab plus ipilimumab (CheckMate 204): Final results of an open-label, multicentre, phase 2 study”, *The Lancet Oncology*, 2021.

[16] J. S. Weber, D. Schadendorf, M. Del Vecchio, J. Larkin, V. Atkinson, et al., ”Adjuvant Therapy of Nivolumab Combined With Ipilimumab Versus Nivolumab Alone in Patients With Resected Stage IIIB-D or Stage IV Melanoma (CheckMate 915)”, *Journal of Clinical Oncology*, 2023.

CIP - Каталогизација у публикацији
Библиотеке Матице српске, Нови Сад

51:62(082)

CONFERENCE on Mathematics in Engineering: Theory and Applications (10 ; 2025 ; Novi Sad)
Conference proceedings [Elektronski izvor] / The 10th Conference on Mathematics in Engineering: Theory and Applications, META 2025, December 12-14, 2025, Novi Sad, Serbia. - Novi Sad : Faculty of Technical Sciences, 2025

Način pristupa (URL): https://imft.ftn.uns.ac.rs/meta-mathematics-in-engineering-theory-and applications/. - Opis zasnovan na stanju na dan 18.12.2025. - Radovi na engl. i srp. jeziku. - Bibliografija uz svaki rad.

ISBN 978-86-6022-756-2

а) Математика -- Примена -- Инжењерство -- Зборници

COBISS.SR-ID 182892553